NUMERICAL MODELING OF BRITTLE ROCK FAILURE AROUND UNDERGROUND OPENINGS UNDER STATIC AND DYNAMIC STRESS LOADINGS

by

Nader Golchinfar

Thesis submitted in partial fulfillment of the

requirements for the degree of Master of Applied

Science (M.A.Sc.) in Natural Resources Engineering

School of Graduate Studies

Laurentian University

Sudbury, Ontario, Canada

THESIS DEFENCE COMMITTEE/COMITÉ DE SOUTENANCE DE THÈSE

Laurentian Université/Université Laurentienne
School of Graduate Studies/École des études supérieures

Title of Thesis Titre de la thèse	NUMERICAL MODELING OF BRITTLE ROCK FAILURE AROUND UNDERGROUND OPENINGS UNDER STATIC AND DYNAMIC STRESS LOADINGS
Name of Candidate Nom du candidat	Golchinfar, Nader
Degree Diplôme	Master of Applied Science
Department/Program Département/Programme	Natural Resources Engineering
Date of Defence Date de la soutenance	July 31, 2013

APPROVED/APPROUVÉ

Thesis Examiners/Examinateurs de thèse:

Dr. Ming Cai
(Supervisor/Directeur de thèse)

Dr. Peter Kaiser
(Committee member/Membre du comité)

Dr. Philip Dirige
(Committee member/Membre du comité)

Dr. Davide Elmo
(External Examiner/Examinateur externe)

Approved for the School of Graduate Studies
Approuvé pour l'École des études supérieures
Dr. David Lesbarrères
M. David Lesbarrères
Director, School of Graduate Studies
Directeur, École des études supérieures

ACCESSIBILITY CLAUSE AND PERMISSION TO USE

Abstract

Stability of underground excavations is a prerequisite for the proper functioning of all other systems in a mining environment. From a safety point of view, the lives of people working underground rely on how well the support systems installed underground are performing. The ground control engineer cannot design an effective support system unless the area of the rock mass around the opening, prone to failure, is well identified in advance, even before the excavation of the tunnel.

Under high stress conditions, usually experienced at deep mining levels, stress-induced rock failure is the most common type of instability around the underground openings. This thesis focuses firstly on the use of the finite difference numerical tool FLAC to simulate brittle rock failure under static in-situ stresses. Brittle failure of the rock mass around underground openings is a particular type of stress-induced failure, which can result in notch-shaped breakouts around the boundary of the tunnel. Generation of these breakout zones is a discontinuum process and approximating this process using FLAC, which is a continuum tool, requires careful consideration of the stress conditions and the stress related behavior of rock material. Based on plasticity theory, this thesis makes an effort to estimate the breakout formation using an elastic – brittle - plastic material model.

Due to seismic challenges that deep mining operations are currently experiencing, rockbursting is a major hazard to the stability of underground structures. Therefore in this research, brittle failure of rock in the vicinity of the underground excavations is approximated also under dynamic loading conditions. The numerically modeled results of two different material models

are compared with each other along with a previously developed empirical graph. This assessment, when further validated by field observations, may provide a different perspective for underground support design under burst-prone conditions.

Keywords: Numerical modeling, brittle failure, depth of failure, rock support, FLAC, continuum modeling, constitutive model, tunnel, URL Mine-by tunnel, dynamic loading, ruckburst, seismicity.

Acknowledgments

I would like to express my very great appreciation to Dr. Ming Cai, my knowledgeable supervisor who had faith in me from the starting day. He gave me the opportunity to improve my skills and constantly provided me with invaluable guidance, recommendations, and suggestions. I cannot possibly count every lesson that I learned from him throughout this period. I also would like to thank him for having the patience to review and correct multiple versions of this document.

My special thanks are extended to the friendly staff of MIRARCO and CEMI. Advice given by Mr. Damien Duff, Dr. Denis Thibodeau, Mr. Pavel Vasak, Dr. Benoit Valley, Dr. Bo-Hyun Kim and Mr. Rob Bewick were of great assistance in my research. I would also like to thank my internal committee members Dr. Peter Kaiser and Dr. Philip Dirige as well as my external examiner Dr. Davide Elmo. Special thanks to my dearest friend, Navid Bahrani, for his continued guidance and constant encouragement. I would like to thank Christopher Groccia for having the patience to review some chapters of this document. Qin Liang, Kim Trapani, Jonathan Waddell and many others were more than just colleagues, but good friends, and the best support team I have ever had the honor of working with. Without their help and support, this thesis could not have been possible.

I am also grateful to Mr. Sean Maloney and Dr. Fidelis Suorineni who trusted me and gave me the opportunity to work at the GRC (Geomechanics Research Center) laboratory. Appreciation is extended to Dr. Ramesh Subramanian, the graduate coordinator at the Bharti School of Engineering, Laurentian University for his support and guidance during my graduate studies.

My gratitude to Mr. Allan Punkkinen for his help and guidance during my training period at Vale's Creighton mine. I learned so much more than I could ever imagine about working at a mining environment in a very short period of time, from Allan and many others at Vale.

Love, thanks and gratitude to my beloved family for their understanding throughout the duration of my studies in Canada.

Finally, my thanks to the following companies and organizations for their financial support which made this research possible: MIRARCO, NSERC, Laurentian University, CEMI, LKAB, VALE, and the William Shaver Masters Scholarship in Mining Health and Safety.

Table of contents

List of Figures

List of tables

Chapter 1

Introduction and overview

With the ever increasing demand for minerals throughout the world and a limited amount of resources, there is also an increasing trend in the price of minerals. It is therefore becoming economical to extract mineral deposits in deep ground. Mining in Northern Ontario is being carried out at depths exceeding 2000 m, while mineral deposits are continuously being discovered at even greater depths. Additionally, deep civil tunnels are constructed for transportation and hydro-power generation and deep geological disposal of nuclear waste is being considered by many countries around the world. The in-situ stress of the ground, in which these underground openings are located, increases with depth. Rock failure can occur due to high mining-induced stresses, generating concerns about excavation stability and the safety of mining personnel.

The level of safety required by various industries differs when designing underground structures. For instance, a temporary pillar needs to be designed for a short stand-up time of the intended operational life cycle of the stope. In a deep nuclear waste storage facility where stability is critical throughout its entire lifetime, the importance of support design and construction procedure cannot be ignored. For some mine drifts, a long stand-up time is required because mine personnel and mining equipment passing through the drifts need to be protected from rock fall hazards resulting from stress relaxation and high stress-induced rock fracturing. Therefore, ground control engineers who are responsible for designing rock support systems need to predict the depth and extent of the unstable zone around the underground openings accurately.

Instability of underground excavations in hard rock is either in the form of gravity-driven failure promoted by rock mass relaxation or in the form of stress-induced failure caused by high stress (Hoek et al., 1995). In the former type of instability, the volume of rock that needs to be

supported can be identified by the orientation and intensity of joint sets and proper support system design can be conducted. The latter case is more complicated and predicting the failure zone is only possible when an improvement in understanding the brittle behavior of rocks around underground openings is made.

Factors that influence the behavior of rocks around the underground openings are: (1) the in-situ stress condition; (2) the rock mass strength; (3) the stress related behavior of the rock mass; and (4) the geometry and sequence of the excavation (Kaiser et al., 2000). This research focuses on conditions where an excavation within brittle hard rock is experiencing both high in-situ and high mining-induced stresses. Mining-induced stresses can be either static or dynamic. Under these conditions, new fractured failure zones can be generated parallel to the excavation boundary, referred to as slabbing or spalling. An estimation of these spalling zones is critical for safe and cost-effective rock support design. The primary goal of this research is to approximate the spalling phenomenon, which results from brittle failure in hard rocks around deep underground openings under both static and dynamic loading conditions.

1.1. Statement of the problem

The excavation of underground structures in hard rocks alters the initial stress state of the rock around the opening. This process alone can create damaged and fractured zones around the periphery of the opening, and brittle failure in the form of slabbing and spalling occurs at locations where the stress concentration reaches the rock mass strength (Martin, 1997). Even under static loading, many unknowns such as rock strength and stress-related behavior of the rock mass present obstacles for us to understand the spalling phenomenon. In addition, rockburst

and seismic loading may introduce dynamic stress and cause further failure. The unstable failure zone resulting from slabbing and spalling is often referred to as a breakout or v-shaped notch. For rock support design, it is important to estimate the depth and geometry of the breakout zone. This can potentially contribute to creating a safe and secure working environment while mining at depth.

For most engineered materials such as steel and concrete, analytical equations exist to predict the behavior of structures under load. On the contrary, due to the non-homogeneous material properties of rocks and the complicated loading conditions encountered around underground openings, the prediction of rock behavior has to rely largely on empirical methods and numerical modeling. An empirical relationship between the depth of failure and the stress level was established for brittle rock by analyzing case studies of observed depth of failure from excavations damaged by rockburst (Kaiser et al., 1996) and tunnels from around the world failing in a progressive manner (Martin et al., 1999). This empirical method provides an estimate of the expected unstable zone, and application of this method for dynamic loading condition was investigated as part of the *Canadian Rock Burst Research Program*, using the FLAC numerical tool for the El Teniente case study (Vasak & Kaiser, 1995). There is still a need for studying the depth of failure around excavations under both static and dynamic loading, and from the previous experience numerical modeling seems to be a useful approach to address this need.

When using numerical tools to simulate brittle rock failure near excavation boundaries, the strengths of the rock, both peak and post-peak, must be considered cautiously because they are among the most influential factors that control the depth of failure. Rock strength can usually be described by two strength components, one for cohesion (c or s) and the other for friction (ϕ or

m), where c, ϕ, m and s are parameters of the two most popular strength criteria – Mohr-Coulomb and Hoek-Brown failure criteria. Recent attempts in modeling brittle rock failure concentrated on the concept of additive contribution of cohesive and frictional strength components. The cohesion-weakening and friction-strengthening model developed by Hajiabdolmajid (2001) is based on a delayed and separate mobilization of strength components relative to the amount of plastic deformation. Some other approaches assume that the friction and cohesion strength components are mobilized instantly and simultaneously during rock deformation. Using an approach of instantaneous cohesion-weakening and friction-strengthening model based on Hoek-Brown failure criterion, Diederichs (2007) successfully predicted the geometry of the failed zone around a circular excavation in brittle rock.

The successful approaches (Hajiabdolmajid, 2001; Diederichs, 2007; Edelbro, 2010) in modeling the failure zones around the excavation boundary require extensive model parameter calibration using observed failure zones. Each of these approaches has an underlying assumption behind the rock strength parameters assigned to the model, and for the same rock (Lac du Bonnet granite) investigated by these researchers, a drastically different set of strength parameters might be needed depending on the selected approach. In some cases the prescribed boundary conditions might have an effect on the chosen strength parameters. In addition to decades of study on rock bursting, limited research has been conducted to study brittle rock failure near excavation boundaries under dynamic loading with a focus on the depth of failure estimation for rock support design. A comparison of available modeling methods and an understanding the differences among them may be helpful for the advancement of the science and engineering in underground construction at depth.

1.2. Research objectives

The first objective of this research is to model the stress-induced brittle rock failure with attention to the model behavior and rock strength parameters. Working toward that end, both peak and post-peak strength behaviors of a brittle rock are taken into consideration. One also needs to consider the stress path and model boundary condition to simulate the depth of failure under static load. All these aspects were studied carefully in this research.

The second object of this research is to study the influence of dynamic loading on brittle rock failure. Once the model is calibrated to capture the failure zone under static loading conditions, dynamic loading may be added to the model to study the effect of dynamic loading on brittle failure surrounding the excavation. The outcome of this study may provide insight for rock support design in burst-prone grounds.

1.3. Approach

The approaches taken in this study are described below.

- An important source of information is obtained from the literature; Underground Research Laboratories (URL) around the globe provide well documented information for studying the rock failure processes during excavation. Initially in this research, a careful review of the literature is conducted to obtain information on the URL Mine-by tunnel in Manitoba, Canada. The laboratory observations of brittle rock failure from the literature are also reviewed at the beginning of the work. Furthermore, different approaches for modeling the brittle failure at URL Mine-by tunnel are reviewed and summarized.

- Failure of hard rocks at low confining stress, as observed in rocks near the excavation boundary, occurs in a sudden and brittle manner. When the confining stress increases sufficiently, the brittle hard rock exhibits a strain-softening behavior. Therefore, to simulate the brittle rock failure, in this research it was suggested that an elastic-brittle-perfectly plastic material model be used. The elastic-brittle-perfectly plastic model is realized in FLAC by modifying the existing Mohr-Coulomb material model (Itasca, 2002).
- The effect of the excavation simulation technique is investigated by comparing different available methods. The resulting stress path and the influence of mesh size on the stress monitoring are studied accordingly.
- An important task when simulating the depth of failure around deep tunnels in massive brittle hard rock is to estimate the rock mass strength. There is a persistent trend to underestimate the strength of rock mass at depth based on experiences from shallow civil engineering case histories where the rock mass behavior is dominated by failure processes in low confinement (Valley et al., 2011). In this research, the peak compressive strength of the rock used in simulating the brittle failure around the tunnel boundary is back-analyzed using the Mine-by tunnel case history.
- The remaining load that the rock can sustain, referred to as post-peak strength, is also back-analyzed using the Mine-by tunnel case history; bearing in mind that under low or no confinement conditions as observed around the tunnel walls, the failed rock mass is not expected to carry considerable load. The load bearing capacity of failed rock mass near boundary of tunnels is verified by field observations of carefully documented case studies as

well as laboratory results of triaxial strength measurements of similar brittle rocks (Hsiao et al., 2011; Stavrogin et al., 1982).

- Finally, the effect of dynamic loading on further deepening the failure zone is investigated through a series of parametric studies. For two types of post-peak behavior, i.e., brittle and strain softening, the numerically simulated depth of failure zone is plotted against the available static stress to the uniaxial compressive strength of the rock mass assigned to the models.

1.4. Scope of thesis

The remainder of this thesis is structured in the following manner:

Chapter 2 reviews and discusses brittle rock failure based on findings reported by other researchers. A summary of conventional procedures for laboratory compression tests to determine the rock strength is presented. Some triaxial test data showing the peak and post-peak strength behavior of brittle rocks are summarized and presented here as well. At next stage, this chapter summarizes the works conducted by previous researchers on how to predict brittle rock failure near excavation boundaries by numerical modeling. The discussion is focused on the URL Mine-by tunnel which was well documented and extensively studied before.

Chapter 3 is a summary and presentation of numerical modeling work conducted in the scope of this research to simulate the conventional compressive strength measurements in the laboratory. The simulated loading path of each test is described in detail and justified based on modeling artifacts involved as well as the strength parameters employed within the model.

Chapter 4 presents the results of simulating brittle rock failure near an excavation boundary by using an instantaneous strength mobilization model which is characterized by an instantaneous cohesion loss from peak to post-peak cohesion strength and an instantaneous friction mobilization from initial to post-peak friction angle. The model is called brittle Mohr-Coulomb model and is considered to be an alternative method for approximating brittle rock failure near the excavation boundary.

Chapter 5 presents the results on dynamic modeling of the depth of failure under burst-prone ground condition. The numerical results and their contour lines of progressive dynamic depth of failure under different intensities of dynamic input wave are presented in an attempt to understand the rock deformation behavior under dynamic loading conditions.

Finally, Chapter 6 provides a summary of the research carried out in this thesis, the major findings from the research, and suggestions and recommendations for future research.

Chapter 2

Observation and simulation of brittle rock failure

2.1. Introduction

From a ground control perspective, it is valuable to be able to predict the depth of failure around the underground openings in order to design safe and cost-effective rock support systems. As mentioned in Chapter 1, the depth and extent of rock failure surrounding an excavation is a function of the excavation's geometry, the strength of the rock mass, and the magnitude and orientation of in-situ stresses (Figure 2-1). At low in-situ stress environments, the failure process is governed by the distribution of natural fractures and the structurally controlled gravity-driven failure. As the in-situ stress magnitude increases, new stress-induced fractures parallel to the excavation boundary will be generated, and the extent of the unstable zone will be dictated by the fractures. With further increase of in-situ stress magnitude, the stress-induced fractured zones may expand over the entire boundary of the excavation (Figure 2-1). The stress magnitude at which these stress-induced fractures coalesce and form the unstable zone is one of the key parameters characterizing brittle failure around the underground openings.

In addition to an increase in depth, dynamic loading from an earthquake or rock burst can also increase the stresses around a tunnel, leading to additional stress-induced failure zones. Rock that was previously stable under static in-situ stresses may become unstable under the temporarily increased stresses due to dynamic loading.

Brittle failure in the form of slabbing and spalling around underground openings can occur at a variety of different depths and rock types; it is not exclusive to deep mining levels and brittle rocks. In this chapter, an overview of the field observations of the brittle rock failure around the underground openings is summarized first. Brittle failure solely due to in-situ static stress is

discussed in Section 2.2.1. Section 2.2.2 discusses cases where statically stable openings become unstable once the additional dynamic stress wave reaches the opening.

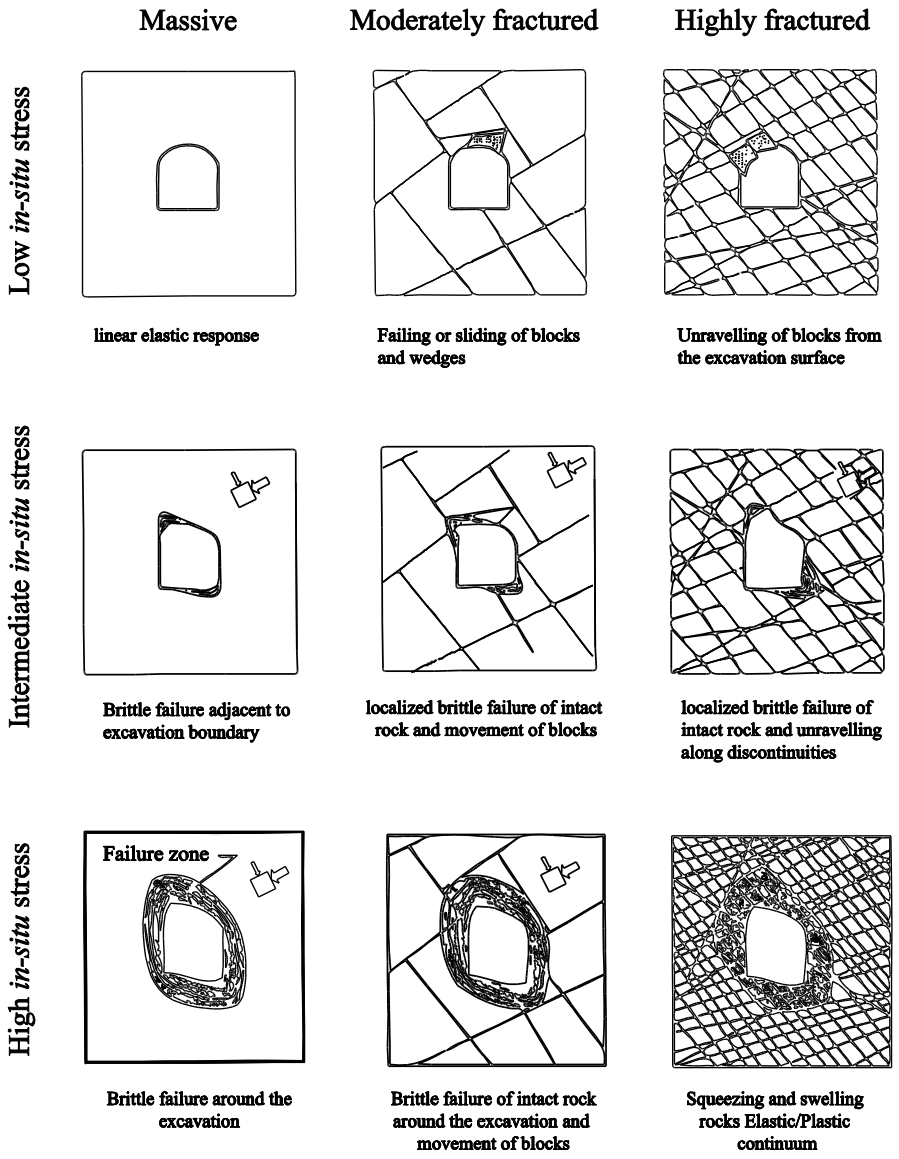

Figure 2-1: Tunnel instability and brittle failure as a function of rock mass rating and the far-field stress (Hoek et al., 1995).

Section 2.3 summarizes the observations of laboratory testing and the commonly used terminologies when describing brittle rock failure. Different loading stages during a laboratory

test for strength measurement are discussed separately. Commonly used failure criteria that are constantly referred to in the literature are also briefly discussed and summarized.

The last section of this chapter summarizes previous research in the simulation of brittle rock failure in the periphery of underground openings. Three modeling approaches proposed by previous researchers for simulating the brittle failure are briefly discussed.

2.2. Field observation of brittle rock failure

Progressive brittle failure in the form of breakout occurs once the stress exceeds the in-situ rock strength at the tunnel wall (Martin, 1995). A distinct characteristic of brittle rock failure around the tunnels is the formation of unstable slabbing zones where the pieces are held together by the friction on the surface of the slabs. This section is a summary of field observations and case histories where high stress to strength ratios causes progressive failure at the periphery of the openings. It is observed that this type of failure can potentially happen at any mining or civil tunneling project where there is a low confining stress acting on the surface of the opening and the tangential stress acting on the boundary is high. Even though most of the observations are within hard brittle rocks such as igneous and metamorphosed rocks (e.g., granites, dolerite, and quartzite), the same brittle behavior can be expected for sedimentary rocks (e.g., sandstone, limestone, and shale).

Both static and dynamic loading conditions may lead to failure of the rock mass. A summary of case studies in which brittle failure occurred due to excessive loading is presented in separate subsections.

2.2.1. Brittle failure under static loading

Two well documented case histories of brittle rock failures under static stress loading are: (1) Atomic Energy of Canada Limited (AECL)'s Mine-by Experiment (Martin et al., 1997), and (2) Äspö Pillar Stability Experiment (APSE) (Andersson, 2007). The calibration of the brittle model under static in-situ stress in Chapter 4 is based on the findings from the AECL's Mine-by Experiment.

- AECL's Mine-by Experiment

The extensively studied Mine-by tunnel at the Underground Research Laboratory (URL) in Manitoba, Canada is a well documented case study of brittle rock failure due to high stresses. The 46 m long, 3.5 m diameter test tunnel was excavated in 0.5 to 1 m round length using perimeter line drilling and mechanical breaking of the central rock stub. The test tunnel was located within the Lac du Bonnet batholith (Figure 2-2a) with few observed natural joints (Martin, 1993). The tunnel was excavated on the 420 m level where the in-situ stress field has been measured as $\sigma_1 = 60\,MPa$, $\sigma_2 = 45\,MPa$, and $\sigma_3 = 11\,MPa$. The test tunnel was oriented approximately in the σ_2 direction with the maximum principal stress acting in a sub-horizontal direction with a 11 - 14° alignment. Some researchers have studied the effect of key parameters on stability of underground openings such as tunnel geometry and geological variability (Everitt, 2001), thermal and humidity effects (Read, 1994), the quality of the rock mass and the effect of confining pressure (Young & Collins, 1999; Read, 1994). Nevertheless, during construction of the URL Mine-by tunnel, all these parameters are kept constant to reduce the number of variables where the failure occurs.

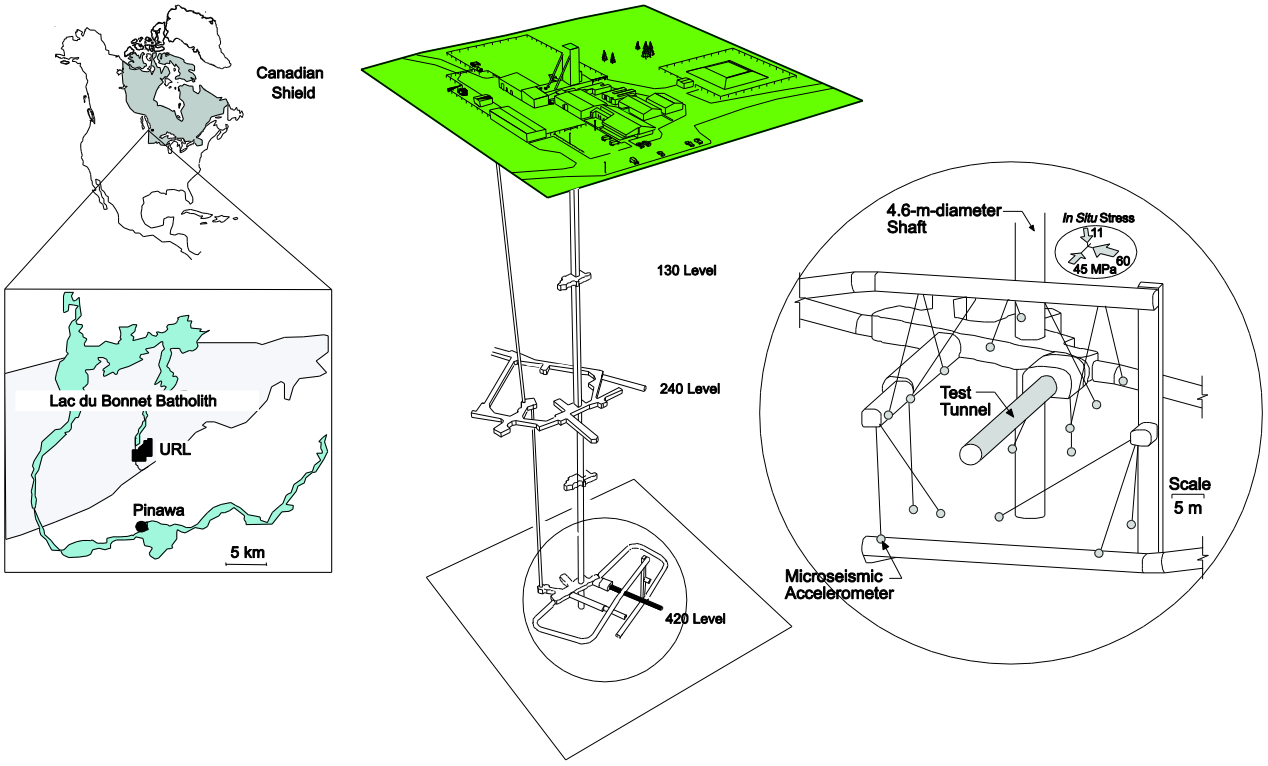

Figure 2-2: (a) The location of the Canadian shield in geographical map of North America and the URL facility in Manitoba, Canada within the Lac du Bonnet granite; (b) perspective view of the 420 m level showing the test tunnel under investigation, observation galleries, and the microseismic sensors (Maxwell & Young, 1998).

A microseismic monitoring array consisting of 16 triaxial sensors was installed to monitor seismicity induced by the excavation (Figure 2-2b). A total of 25,000 microseismic events (local magnitude $M_L < 0$) were recorded between August 1991 and July 1992, during the excavation of the tunnel (Young & Martin, 1993). The induced microseismic events tended to cluster immediately around the tunnel, near the locations where breakouts eventually developed. The location of microseismic events recorded during the 12-hour monitoring period after the

excavation of round 8 is shown in Figure 2-3a. The seismicity was attributed to fracturing associated with the notch formation (Young & Martin, 1993).

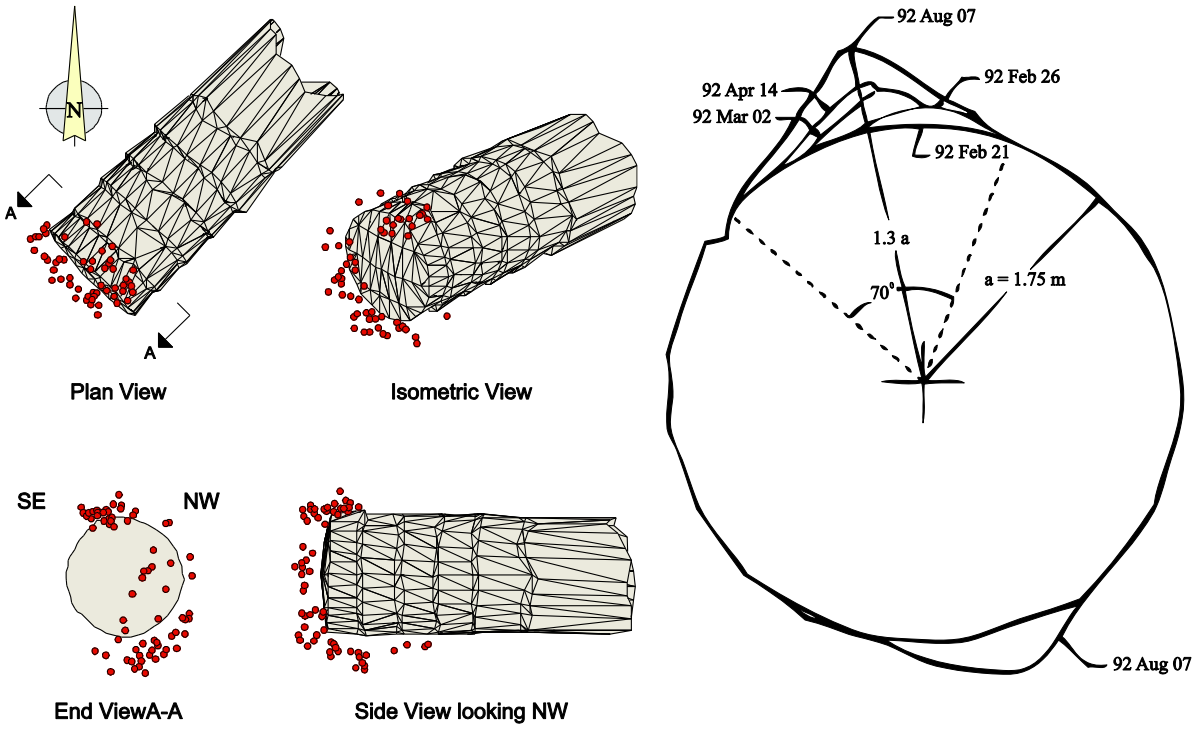

Figure 2-3: (a) Microseismic monitoring results from the Mine-by tunnel showing microseismic events ahead of the tunnel face in regions where breakouts eventually developed as the tunnel advanced (Read, 2004); (b) Progressive development of the breakout notch in the Mine-by Experiment tunnel (March - August 1992) (Martino & Chandler, 2004).

The slabbing on the surface of the tunnel started about 0.5 m back from the tunnel face and progressed into the wall as the tunnel further advanced. Figure 2-3b and Figure 2-5 illustrate this progressive development of the notch at one cross-section of the tunnel. The maximum depth of the notch in the roof of the Mine-by tunnel was 1.3 times the radius of the tunnel from the center of excavation as illustrated in Figure 2-3b. The maximum depth of the notch on the floor of the Mine-by tunnel was significantly smaller than the notch in the roof (Figure 2-3b). Boreholes

drilled into the floor revealed how rapidly the damage decreased away from the slabbing zone (Figure 2-4). In this region, the gravity is not in favor of forming the failure zone. The asymmetry of the failure zones in the roof and floor of the Mine-by tunnel was also partly attributed to the tunnel orientation relative to the principal stress axes (Read et al., 1995). Studies by Read et al. (1995) and Eberhardt (2001) showed that the rocks at the tunnel invert experience a rather different stress path, leading to a maximum compressive stress slightly lower than that in the roof of the tunnel.

At this tunnel, once the notch was formed, it remained stable unless it was disturbed by changing conditions, such as an increase in temperature, a small stress change caused by nearby excavations or significant stress changes caused by a seismic event or blasting.

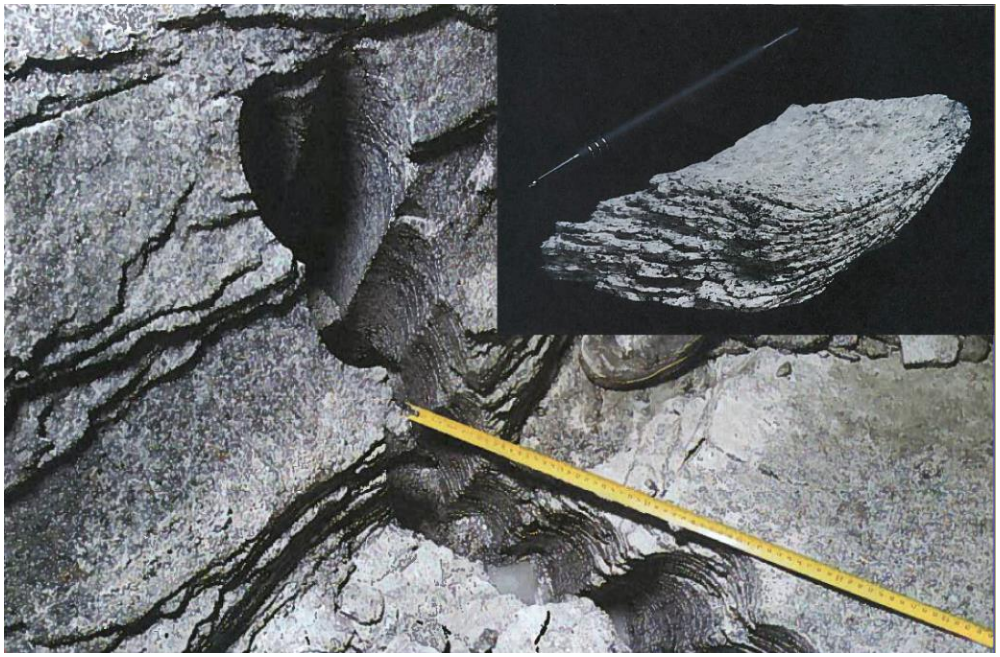

Figure 2-4: Boreholes drilled across the inverse notch tip on the floor revealed the slabbing extended 200 mm into the rock mass and diminished away from the surface (Read & Martin, 1996).

At the roof and the floor of the tunnel, the slabbing initiated where the maximum compressive stress was concentrated at the tunnel boundary and then propagated further into the rock mass. A three-dimensional boundary element analysis conducted by Read (1994) suggested that the maximum compressive stress occurring in the roof of the tunnel was approximately 160 MPa, while the analytical solution for a simplified smooth-boundary circular opening suggests a maximum tangential stress of 169 MPa on the boundary of the tunnel. Figure 2-5 shows the careful mechanical excavation process that led to purely stress-induced fracturing around the tunnel. The mean value of the Uniaxial Compressive Strength (UCS) of intact samples of the Lac du Bonnet granite measured in the laboratory was 212 MPa. In reality the strength of in-situ rockmass is different from that obtained from laboratory tests of intact rock samples. The failure on the tunnel boundary could not have happened unless the in-situ rock mass strength was less than the maximum stress on the boundary of the tunnel (σ_{crm} < 169 MPa).

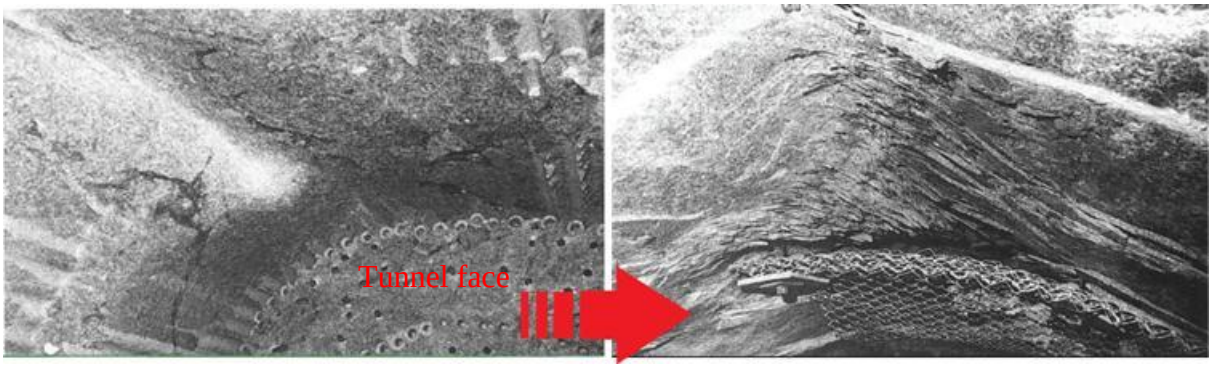

Figure 2-5: The initiation of the failure process delineated by the faint white color, caused by crushing. Note that the failure process zone initiates about 0.5 m back from the tunnel face (Read & Martin, 1996).

The compressive stress region was not the only stress-induced damage zone surrounding this tunnel. Tensile stresses in the sidewalls of the Mine-by tunnel caused invisible grain-scale

cracks. The grain size of the rock in the tensile region and the magnitude of the tensile stresses can affect the degree of cracking. The tangential stress at the Mine-by tunnel wall exceeds the tensile strength of the rock mass ($0.1\sigma_{crm}$), which, according to plastic theory, should result in visible macroscopic cracks. Even though geophysics surveys detected the development of microscopic damage in the sidewall regions (Read & Martin, 1996), no macroscopic tensile failure was visible in the test tunnel. Cai (2008) claims that the predicted damage zone in the tensile sidewall region is affected by the choice of excavation method. He studied the influence of excavation method on the generated loading path using FLAC. The sudden removal of material, as in drill and blast methods, induces more damage to the tensile sidewall region, whereas the gradual tunnel advancement will cause small disturbance to the rock mass in this region. This thesis will not concentrate on rock failure in the tensile zone, but instead will focus on rock failure in the compressive breakout zone.

- The Äspö pillar stability experiment

The Äspö Pillar Stability Experiment (APSE) was conducted between 2002 and 2006 by the Swedish Nuclear Fuel and Waste Management Company (SKB) at 450 m level in Äspö HRL (Hard Rock Laboratory) (Figure 2-6) for testing the Swedish concept of underground storage of used nuclear fuel in the crystalline Scandinavian shield (Andersson, 2007). The main objective of the experiment was to investigate the progressive failure process in a heterogeneous and fractured rock mass when subjected to both excavation-induced and thermal-induced stresses.

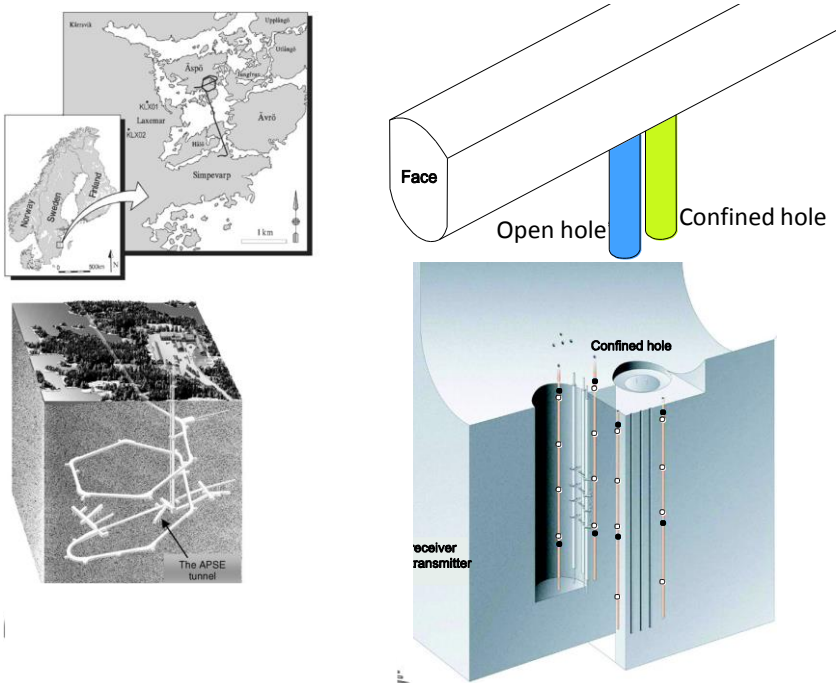

Figure 2-6: Location of the Äspö Pillar Stability Experiment and the coupled shafts (Andersson & Martin, 2009).

A 1 m thick experimental pillar was formed by drilling two 1.8 m diameter vertical boreholes. One was an open hole and other was a confined hole (Figure 2-6). The pillar was carefully monitored throughout the excavation of the boreholes. The pillar was intentionally over stressed, using thermally-induced stresses to induce spalling. It was anticipated that the damage to the pillar would be dominated by the stress-induced fracturing of the intact rock (Figure 2-7). The major difference between the APSE and the Mine-by Experiment is that APSE was located in a fractured rock mass although the intact uniaxial compressive strength of the Äspö Diorite is similar to that of the Lac du Bonnet Granite. The laboratory test results showed that the mean value of UCS of the intact rock, the Young's modulus, and Poisson's ratio are 211 MPa, 76 GPa, and 0.25, respectively (Andersson & Martin, 2009). The laboratory rock strengths for the Äspö pillar and the Mine-by tunnel sites are compared in Table 2-1.

Table 2-1: Comparison of the Uniaxial Compressive Strength (UCS) of the rocks and the in-situ principal stresses at the Äspö pillar and the URL Mine-by tunnel sites (after Martin (2005))

Underground Facility	Laboratory Mean Value (MPa)	In-situ stresses (MPa)
	UCS	$\sigma_1, \sigma_2, \sigma_3$
Äspö pillar stability experiment Äspö Diorite	211	30, 15, 10
Mine-by Experiment Lac du Bonnet granite	212	60, 45, 11

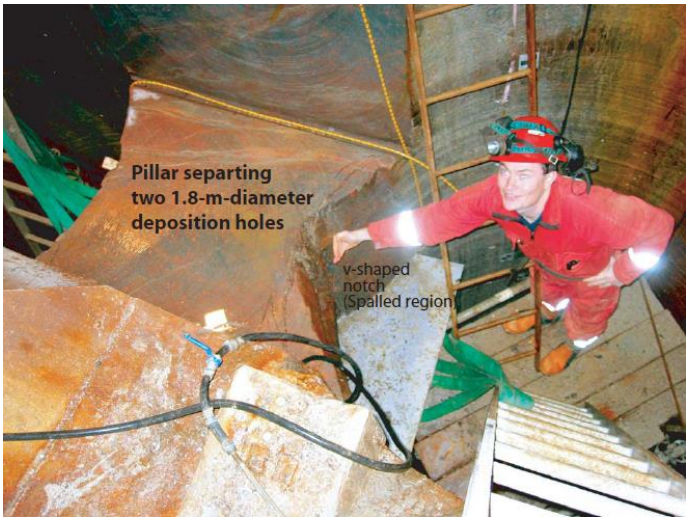

Figure 2-7: The Äspö Pillar Stability Experiment, showing the extent of the notch in the 1m thick pillar (Martin, 2005).

Thermal modeling by Anderson and Martin (2009) showed that thermally-induced stresses in the pillar were adequate to increase the pillar stresses above the stress magnitude expected to initiate failure. The stress magnitude for failure initiation as a spalling limit was back calculated to be equivalent to the crack initiation stress level obtained from laboratory tests. The failure initiation from laboratory tests of intact rock occurred in a stress range of 80 to 135 MPa, which may give a clue for estimating the strength of the in-situ rockmass. An acoustic emission (AE)

study showed that approximately 17,000 events were recorded during thermal loading, and most events were concentrated at the location of the V-shape notch (Figure 2-8).

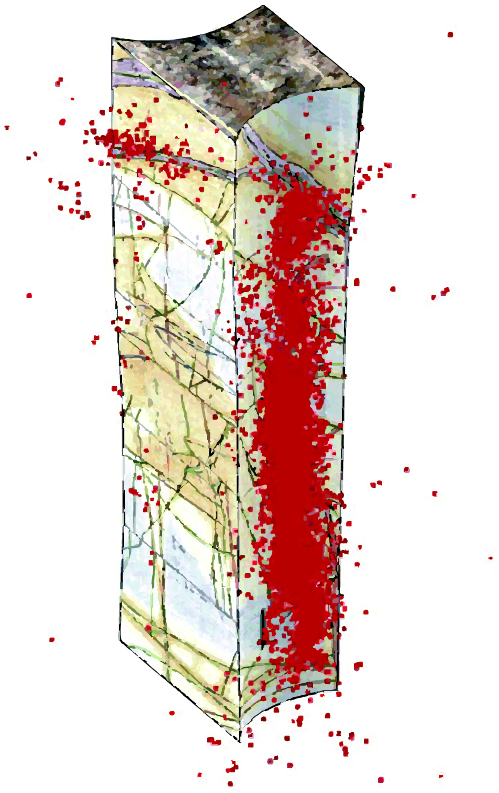

Figure 2-8: The location of AE events in the pillar (Andersson & Martin, 2009).

The excavation of an underground opening changes the in-situ stress around the boundary of the tunnel. In both case studies, slabbing and spalling failure occurred long before the stresses at the boundary of the tunnel reached the strength of the intact rock tested in the laboratory. Based on the maximum possible tangential stress at the boundary of the opening, it is reckoned that the rock mass strength in the field must be smaller than the intact rock strength in order to allow failure to initiate. Therefore, as will be discussed in Section 2.4.1.2, the back calculated strength of the rock mass in the numerical models, should be less than the laboratory intact rock strength.

2.2.2. Brittle failure under dynamic loading

The stress distribution around an opening, solely due to the excavation process, can lead to instability around the tunnel boundary. At greater depths, the stress-induced failure can occur in a violent manner, leading to seismic events and rockbursts.

Many authors define rockbursts as the result of a sudden and violent failure of rock (Stacey & Ortlepp, 1993; Kaiser et al., 1996; Cai et al., 2012). This particular type of rock failure is mostly associated with hard rocks and geological structures such as faults and dykes. When a rock fails during the excavation of a tunnel, it experiences three deformation stages: (1) pre-existing crack growth, (2) stable growth of secondary cracks, and (3) the unstable growth and coalescence of secondary cracks to form macrocracks. If the dissipative energy to grow pre-existing cracks and secondary cracks is smaller than the elastic strain energy stored in the rock mass, the residual strain energy will be released suddenly, in the form of the kinetic energy imparted to rock fragments, resulting in a rockburst. For a rock to fail violently, the loading system stiffness has to be smaller than the post-peak unloading stiffness of the rock.

Ortlepp (1997) presented Table 2-2 as a simplified classification of different types of rockburst and their associated magnitude. The magnitude of smaller events in this table is essentially a rough estimate and the biggest possible events can range up to greater than 4.0 in the Richter magnitude scale. On this basis, Cai et al. (2012) further simplified the types of rockburst into three broader categories – *strainburst, pillar burst,* and *fault-slip burst*. The first category also includes buckling-type rockbursts, and shear rupture rockbursts are grouped within the fault-slip rockburst category. Based on the location of the seismic source, rockbursts are either mining-induced if the damage happens at the seismic source or dynamically-induced if the source is at a

distance from the damaged area. In either case, there will be an increase in dynamic stress in the rock mass due to a seismic event.

Table 2-2: The most common types of rockbursts and their magnitudes (Ortlepp, 1997)

Seismic event	Strainburst		Pillar burst	Fault-slip	
	Strainburst	Buckling	Pillar burst	Shear rupture	Fault-slip
Richter magnitude M_L	-0.2-0	0-1.5	1.0-2.5	2.0-3.5	2.5-5.0
Requisite condition	Failure surface close to a free surface	Free surface >> lamina thickness	Stress > strength in destroyed volume	Shear stress exceeds:	
				Shear strength of rock	Shear strength at asperity

A dynamic stress increase can induce rock mass failure when the instantaneous tangential stress (static stress + dynamic stress) exceeds the peak strength of the rock mass. This failure process will be violent if the rock mass surrounding the fracturing rock create a relatively "soft" loading environment (Cai et al., 2012).

It is mentioned in the *Canadian Rockburst Support Handbook* (Kaiser et al., 1996) that the damage a rockburst can cause to an underground opening can result from one of three mechanisms: (1) *rock bulking* due to fracturing, (2) *rock ejection* due to strainburst and seismic energy transfer, and (3) *rockfalls* induced by seismic shaking (see Figure 2-9). The last mechanism is a structurally controlled type of rockburst where the volume of the loosed rock, defined by the preexisting joint sets and discontinuities in the rock mass, will be triggered to fall. The first two mechanisms, however, are stress-induced and their failure mechanisms are more complicated. Rock bulking and ejection can occur in an unexpected manner with just a small dynamic stress increase if the stress in the immediate skin of the rock mass before the seismic

wave reaches the tunnel boundary is at a critical stage (i.e., the stress is very near the peak strength of the rock mass).

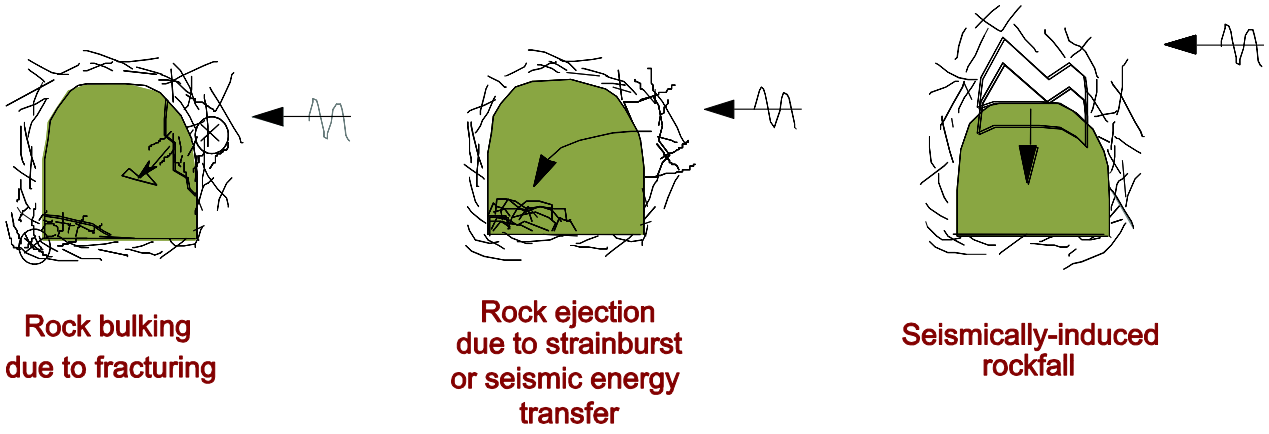

Figure 2-9: Rockburst damage mechanisms (modified from Kaiser et al. (1996)).

An illustrative documentation by Ortlepp (1997) provides multiple pictures from each type of rockburst summarized in Table 2-2. The interested reader is recommended to refer to the original source for details; however, in the scope of this research, only four case histories are summarized. The first one is a historical milestone in the field of rock mechanics, in terms of how it has increased our understanding of the rockburst phenomenon. This event provided field evidence for the first time in North America that slip on an existing fault can be a source mechanism of a large rockburst. The second case history is a visually descriptive one summarizing a mining-induced rockburst event in a deep South African mine and the third one is a brief summary of fatal rockburst accidents at El Teniente Mine in Sewell, Chile. Finally the last case history is a summary of three major mining-related seismic events that all occurred at Kidd mine in Timmins, Ontario.

- Large fault-slip event (Sudbury, Ontario)

On June 20, 1984, a seismic event occurred at the Falconbridge mine in Sudbury, Ontario, Canada. A powerful rockburst with a magnitude of 3.4 on the Richter scale shook the entire mine and caused a collapse of the backfill in a nearby stope where four miners were working. In the next half hour, 116 microseismic events were recorded and shortly after, a series of large seismic events temporarily interrupted efforts to rescue the trapped men at the stope.

A committee of technical experts from Canada, the United States, and South Africa were gathered to examine the underground workings to help determine the cause of the event. As reported by the committee (Stevenson, 1986): "The microseismic monitoring system located the epicenters of the events along a series of faults in the immediate area, and the technical committee concluded that the rockburst occurred when a very large mass of rock moved suddenly along what is known locally as the Ore Pass Fault." The energy from the rock movement along the fault shown in Figure 2-10 was announced as the source mechanism of the seismic event recorded on June 20, 1984.

From the south view of a drift, Figure 2-10a showed fresh spalling along the trace of the easterly dipping fault, at a distance of about 50 m from the damaged stope. However, no detectable slip was observed at this point. The north view of the fault intersection with the drift at a higher level shows distinctive signs of fault movement (Figure 2-10b).

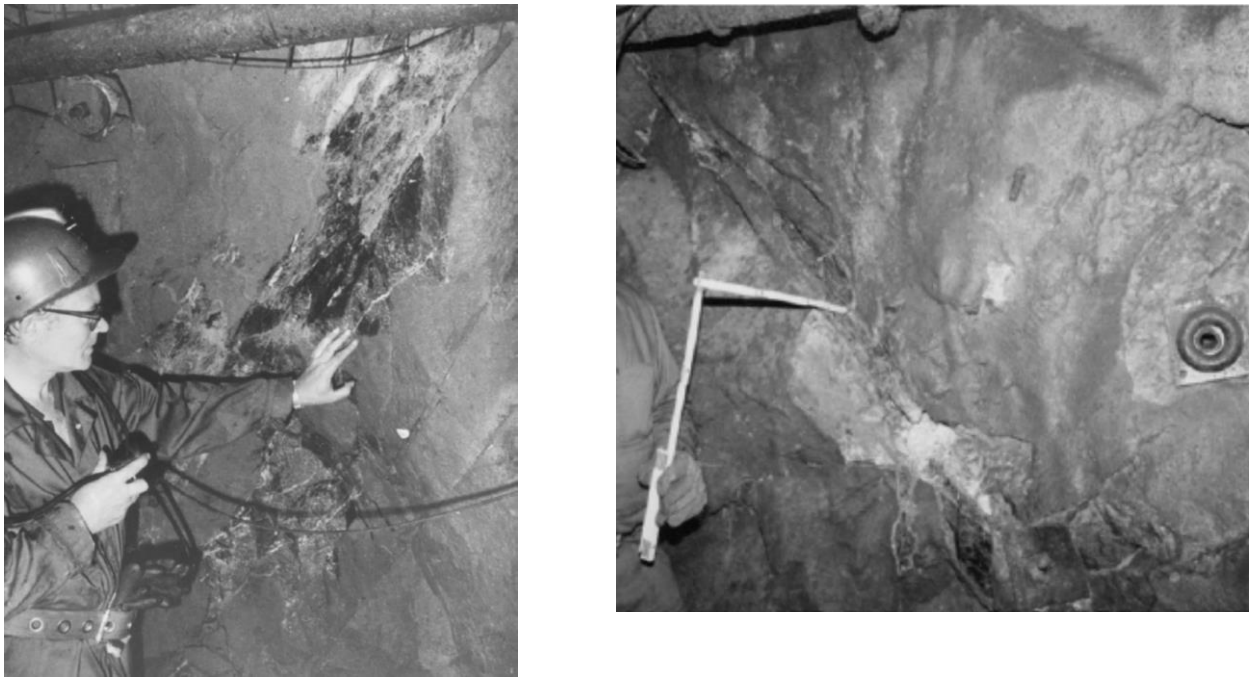

(a) **(b)**

Figure 2-10: (a) South side and (b) north view of easterly dipping fault (Ortlepp, 1997).

This event was considered as one of the most significant examples of fault-slip mining-induced seismicity that had occurred in the Canadian mining history. After the initial technical report was issued, a Provincial Committee of Inquiry was established to make recommendations based on the findings of the report. One of the recommendations was to create a research organization funded by some mining companies, the provincial, and federal governments, as well as to establish a special chair in ground control at an Ontario university. The Geomechanics Research Center (GRC) at Laurentian University in Sudbury and the mining research directorate were the direct result of these recommendations.

- Carletonville Gold Mine (South Africa)

The Carletonville district gold mine in South Africa operates at great depths over a strike length of almost 20 km and for 8 km down-dip at 20 degrees. As a consequence, mining-induced seismicity and severe rockbursts have occurred at deep levels. Ortlepp (1993) described in detail one of the most severe events that occurred in 1977.

This event that was registered as $M_L = 1.8$ on the Richter magnitude scale at the WWSSN station at Pretoria (60 km away from the mine site), severely damaged a drift at a depth of 3500 m. The damage occurred over a 90 m length of the tunnel at a short distance, on the west side of the part that was previously re-opened and re-supported after a previous rockburst. Figure 2-11a shows a wide view of the failure scene after the rockburst, while the existing situations before and after the event are sketched in Figure 2-11b. The severity of the event is evident by displacement of the concrete drain fragment (Figure 2-11c) from its original position in Figure 2-11a to the unstable position indicated in Figure 2-11b after the rockburst.

(a)

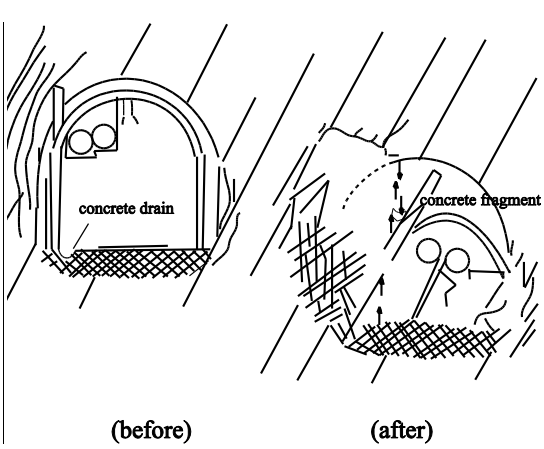

(b)

(c)

Figure 2-11: (a) General view near the easterly end of the damaged portion of 52 haulage; (b) sketch of haulage section before and after the rockburst event; (c) detail of concrete fragment (Ortlepp, 1993).

A few large fractures at the left hand side of the tunnel appeared to be the stress-induced slabbing either during the construction of the tunnel or from previous events. After the event, the notch formed at the upper left corner of the tunnel and the scattered pile of slabbing was on the floor. The final failure shape was in part controlled by the pre-existing rock mass structure. This case history was an illustrative instance of a seismically-triggered strainburst, even though the magnitude of the event is slightly higher than the upper range of this type of rockburst (1.5 Richter) in Table 2-2. The geological condition at the failure site might have created an ideal loading environment which allowed release of large seismic energy due to rock failure.

- El Teniente Mine (Chile)

In high-stress fields, it has been observed that rapid draw can result in the creation of rockbursting conditions. Extraction in El Teniente Sub 6 Sector had to be stopped in March, 1992 after several rockbursts caused fatal accidents, reflecting the low level of knowledge at the time about mining in the primary rock.

Figure 2-12: A good example of dynamic loading induced rock failure with well defined depth of failure at El Teniente (courtesy of Peter Kaiser).

- Kidd Mine (Timmins, Ontario)

On January 6, 2009, three large seismic events occurred at Kidd Mine, between the 6800 and 7100 Levels. The largest event had a local magnitude of 3.8. This large event, which was believed to have been initiated on the North G Fault, was followed 18 minutes later by a 1.7 aftershock approximately located in the footwall of the 86 panel on the North K Fault at 6900 L, and by a 1.1 event on the 6800 Level, again on the North G Fault, in the southern footwall of the 68-SL3 Stope (Counter, 2010).

The observed damage affected almost 1500 m of development, on 7 Levels. The damage ranged from minor shake down of old loose, light to heavy bagging of screen, ejected material and floor heave to 1.5 m deep, to extensive collapse of development, particularly in intersections or where support had not been upgraded to burst rated standards. Most of the severe damage was restricted to within 10 to 20 m of the major shear rupture, and affected 450 lateral meters of drift (Counter, 2010). Several pieces of production equipment were trapped as a result. Beyond this distance, damage decreased to general loosening of the rock mass which was contained by the support, to no observable damage.

Another major burst with a magnitude of 3.1, occurred on June 15, 2009. The trigger for this event was concluded to be the mining of the 77-917 Stope, which was situated in the north abutment of the 7500 Level sill, in roughly the center of the orebody. This event caused further falls of ground in areas which had been damaged in the January 6 event which had not yet been re-supported, particularly on the 6800 Level where up to 2 m of fresh material failed from the unsupported back and south wall of the intersection of the 68-01 Dr. South with the 68-76 cross

section, and on 7100 Level in the 01 Dr. South along the suspected second seismic rupture. The event caused a major fall of ground in the intersection of the 75-01 Drift with the Ramp Access (Figure 2-13). The back failed up to 4 m above the original elevation, and up to 5 m of rock was ejected from the walls of the 75-01 Dr. in the vicinity of the North K Fault. Major damage also occurred in the 75-90 and 75-89 cross sections, where major expulsion of material occurred from the lower walls. Figure 2-13 is a good example of dynamically-triggered fall of grounds. Rock masses damaged by static and dynamic loading may be temporarily stable under support. However, when new dynamic loading due to a near-by rockburst strikes, the previously stable rock mass can be further fractured and if the installed rock support system is not sufficient, failure of the rock mass will occur. This failure mechanism is studied in Chapter 5.

Figure 2-13: 75-01 Drift at Ramp Access Intersection – near completion of primary rehabilitation. "Drift" shaped opening in background is approximately 3 m of cave above original development, the original back of which is even with the top of the muck ramp (Counter, 2010).

2.3. Brittle failure in laboratory compression tests

In the laboratory, rock strengths are obtained using small cylindrical rock samples under loading. There are different loading and testing conditions, and ignoring the influence of joints and structures at the field scale make it difficult for the lab results to represent the field rock mass strength properly. However, if these test conditions and limitations are understood well, the test results may still be useful in engineering design.

Intact rock samples are tested under different confining stresses and the maximum load-bearing capacity under zero confinement is referred to as the uniaxial compressive strength. This strength value can be obtained using conventional test facilities but to capture the post-peak behavior, a stiff test machine has to be used. The post-peak strength of the rock also contributes to the process of failure zone development and can influence the stability of an excavation. It is necessary to understand all the stages of the failure process in a laboratory scale sample before starting to model the failure around underground openings. Details of the failure process can be studied by monitoring stress, strain and acoustic emissions. The complete process of failure in the rock samples consists of three main stages, i.e., pre-peak, peak, and post-peak stages.

2.3.1. Pre-peak stage

Some models assume that rocks behave elastically before the peak strength is reached. This is not entirely true. In fact, the pre-peak deformation stage can be divided into the following stages: (1) crack closure, (2) linear elastic deformation, (3) crack initiation, (4) stable crack growth, (5) crack coalescence and crack damage, and (6) unstable crack growth. Elastic properties of rock

(Young's Modulus and Poisson's ratio) are obtained in Stage 2 regardless of the confinement on the sample. Starting from Stage 3, irreversible plastic deformation due to micro-cracking occurs.

The effect of confining stress on the elastic properties of rocks has been investigated by several researchers. Corkum and Martin (2007) investigated the effect of confinement on the stiffness (Young's modulus) of Opalinus Clay with micro-cracks. Confined test data demonstrated that the stiffness of Opalinus Clay samples increased with increasing confining stress. Other researchers observed similar trends for other rocks (Kulhaway, 1975; Stavropoulou, 1982). Hajiabdolmajid (2001) states that the confinement dependency of Young's modulus is generally stronger for porous rocks and is attributed to the closure of pores during hydrostatic compression. For undamaged Opalinus Clay samples as illustrated in Figure 2-14, the linear elastic behavior (Stage 2) constitutes a portion of pre-peak stress-strain curve. Martin (1993) found the stiffness of Lac du Bonnet granite is very sensitive to the confinement if the sample is significantly damaged. For intact rock samples, the Young's modulus does not change significantly with confinement (60 GPa at the 420 level of the URL).

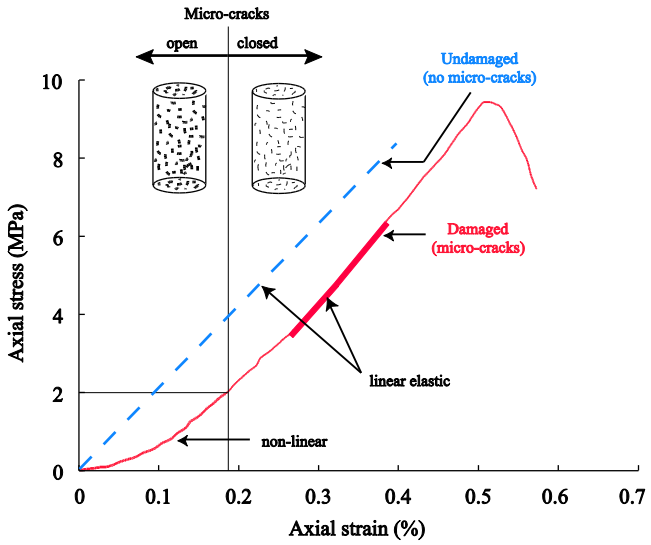

Figure 2-14: Illustration of the effects of open micro-cracks on the stress–strain curve of an unconfined compression test (Corkum & Martin, 2007).

Another important phenomenon that starts in the pre-peak deformation stage of brittle rocks and continues to the post-peak stage is dilation or volume increase. Experimental works carried out to investigate the volume increase behavior revealed that the phenomenon is associated with the initiation and propagation of cracks and is closely related to the process of rock failure. Zhao and Cai (2010) recently investigated the relative change of volume in rock samples and proposed a mobilized dilation angle model which considers the influence of both plastic strain and confinement on dilation. From laboratory test, it is seen that the onset of dilation coincides with the crack initiation threshold, and is marked as the point where the volumetric strain curve departs from linearity (Bieniawski, 1967; Martin, 1993). The crack initiation stress-level is approximately 0.3 to 0.5 times the maximum load that the sample can take (Bieniawski, 1967; Martin, 1993; Cai et al., 2004). After the crack initiation stress is reached, dilation increases gradually along with the generation of new stable cracks but the volume of the rock sample continues to decrease until the stress reaches the crack propagation stress level. At this point, the

crack density is sufficiently high to allow crack interaction and coalescence to happen. This defines the onset of crack damage, which starts at a stress level of approximately 0.7 to 0.8 times the peak strength (Martin, 1993; Martin & Chandler, 1994).

As the applied load to the sample increases, the coalescence of cracks and the subsequent dilation further increases and the stress will eventually reach the peak strength of the rock sample.

2.3.2. Peak

The peak strength is the maximum stress that a rock can sustain under short-term loading conditions. As mentioned above, the peak strength of rock is normally obtained from compression test using cylindrical samples. The standard measure of the rock strength is obtained from tests of 54 mm diameter samples, with a 2 to 2.5 length to diameter ratio, at a slow loading rate such that the failure occurs within 2 to 15 minutes of loading (based on the ASTM – D7012 -10 Standard). Many researchers have investigated the effects of samples size (Hoek and Brown, 1980; Martin, 1997) or scale (Lockner, 1995), saturation (Hakala & Heikkila, 1997), and loading rate (Lajtai, 1971) on the peak strength.

The peak strength of most rocks is strongly affected by confinement. In other words, increasing the confining stress will increase the compressive strength of the rocks. Empirical failure criteria (Franklin, 1971; Bieniawski, 1974; Hoek & Brown, 1980; Sheorey et al., 1989) have been developed to relate the strength of the rock to the confining stress. Two parameters (a cohesive parameter and a frictional strength parameter) are often used in these failure criteria. Hoek and Brown (1980) describe the relationship between the peak strength and the confining stress using

a two-dimensional empirical model which is now widely known as the Hoek-Brown failure criterion. Later, the generalized Hoek-Brown failure criterion was introduced (Hoek & Brown, 1997) for jointed rock masses. The Hoek-Brown failure criterion is expressed by Eq. (1).

$$\sigma_1 = \sigma_3 + \sigma_{ci}\left(m\frac{\sigma_3}{\sigma_{ci}} + s \right)^a \tag{1}$$

where σ_1 and σ_3 are the major and minor effective principal stresses, and σ_{ci} is the uniaxial compression strength of the intact rock, m, s and a are model parameters that can be related to the Geological Strength Index (GSI) (Hoek et al., 1998; Hoek et al., 2002).

On another hand, the Mohr-Coulomb failure criterion is a linear criterion which expresses the shear strength τ of a rock as a linear function of a given normal stress σ_n. This criterion can be expressed by Eq. (2).

$$\tau = c + \sigma_n \tan\phi \tag{2}$$

where c and ϕ are cohesion and friction angle strength parameters, respectively. Alternatively, the Mohr-Coulomb failure criterion defining the peak strength can be defined in terms of the major and minor principal stresses, by Eq. (3).

$$\sigma_1 = \frac{2c\cos\phi}{1-\sin\phi} + \frac{1+\sin\phi}{1-\sin\phi}\sigma_3 \tag{3}$$

Because the cohesive and frictional strength components in the non-linear Hoek-Brown failure criterion are represented by s and m, respectively, it is difficult to link them to any physical parameters in practice. In addition, many engineering programs employs the Mohr-Coulomb

failure criterion as their default failure criterion. Hence, it is necessary to determine equivalent Mohr-Coulomb cohesive and frictional strength parameters for a range of confining stress. This can be performed by fitting an average linear relationship to the curve generated by Eq. (1) for a range of minimum principal stress values defined by $\sigma_t < \sigma_3 < \sigma'_{3max}$ (Hoek et al., 2002), where σ_t is the tensile strength of the rock and σ'_{3max} is the maximum confining stress that is expected to occur. The software package Rocklab, developed by Rocscience (2007), can be used to find equivalent strength parameters between the Mohr-Coulomb and Hoek-Brown failure criteria.

Because the strength parameters *c* and ϕ (or *s* and *m*) are used to define the peak strength, they need to be altered to describe the strength in the post-peak stage.

2.3.3. Post-peak stage

The post-peak behavior of rocks was studied only after the development of stiff servo-controlled test machines in the middle of 1960s. Figure 2-15 summarizes the confined test data of Tailuko marble (Hsiao et al., 2011) and Karelia granite (Stavrogin et al., 1982) at peak and post-peak stages. It can be seen from Figure 2-15 that the laboratory strength data can be used to generate two sets of trend lines that are referred to as strength envelopes. The non-linear strength envelopes fit the laboratory data better, particularly at the post-peak stage. Other triaxial test results also support the non-linearity of strength envelopes (Wawersik & Fairhurst, 1970; Zhao et al., 2010). However, at low confinement pressures (0-5 MPa) the linear strength envelope is a reasonable approximation for the test data.

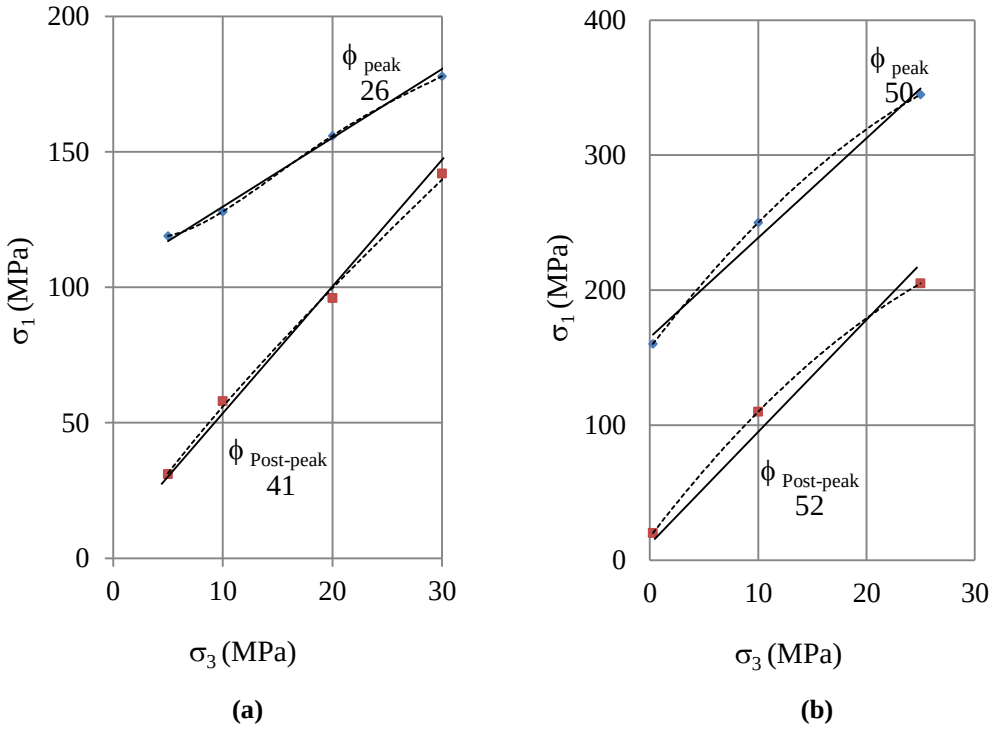

Figure 2-15: Mohr-Coulomb peak and post-peak strength envelopes for: (a) Tailuko marble (Hsiao et al., 2011) and (b) Karelia granite (Stavrogin et al., 1982).

Triaxial test results such as the ones presented in Figure 2-15,indicate that a common feature of the linear post-peak strength envelopes for brittle rocks, at low σ_3, is that the σ_1-axis-intercept of the post-peak strength envelope is small (in the order of 0 to 0.5 MPa). This can be interpreted by a small post-peak cohesion value based on the Mohr-Coulomb criterion (Eq. (3)). In other words, once the rock fails and if the damage process continues, the rock will lose most of its cohesive strength.

On the other hand, the slope of a non-linear strength envelope tends to decrease as the confinement increases. Hence, the linear post-peak strength envelope (defined by c and ϕ) may not be suitable when the confinement is high. Nevertheless, under low confinement conditions

such as those around a tunnel boundary where rock failure occurs, the linear strength envelope is an acceptable simplification.

At low confining stresses, the post-peak strength envelope is generally steeper than the peak strength envelope, governed by a high post-peak friction angle. For example, the peak and post-peak friction angles for the Tailuko marble, under low confinements, are 26° and 41°, respectively. Other test data analyzed in this study show that the post-peak friction angles of hard rocks under low confinements vary primarily between 40° and 55°. This statement may be valid only under low confining stresses when there is limited straining of the fractured rocks; at higher confinement pressures, the asperities of fractured rocks are easy to be worn out and the post-peak friction angle will be smaller than that under low confinement condition.

The mobilized friction angle can also be viewed from a microscopic view point. The concept of joint roughness coefficient (JRC) proposed by Barton and Choubey (1977) and further developed to a mobilized JRC (Bandis et al., 1983) can be used to describe the strength of a joint at different deformation stages. Based on Barton's joint model, even when the displacement is about 10 times that of the displacement that corresponds to the peak strength, the mobilized JRC_{mob} is only half of JRC_{peak}. Figure 2-16 shows that the residual joint strength can only be reached at extreme shear displacements and the post-peak strength before the residual strength is reached is termed as the ultimate strength.

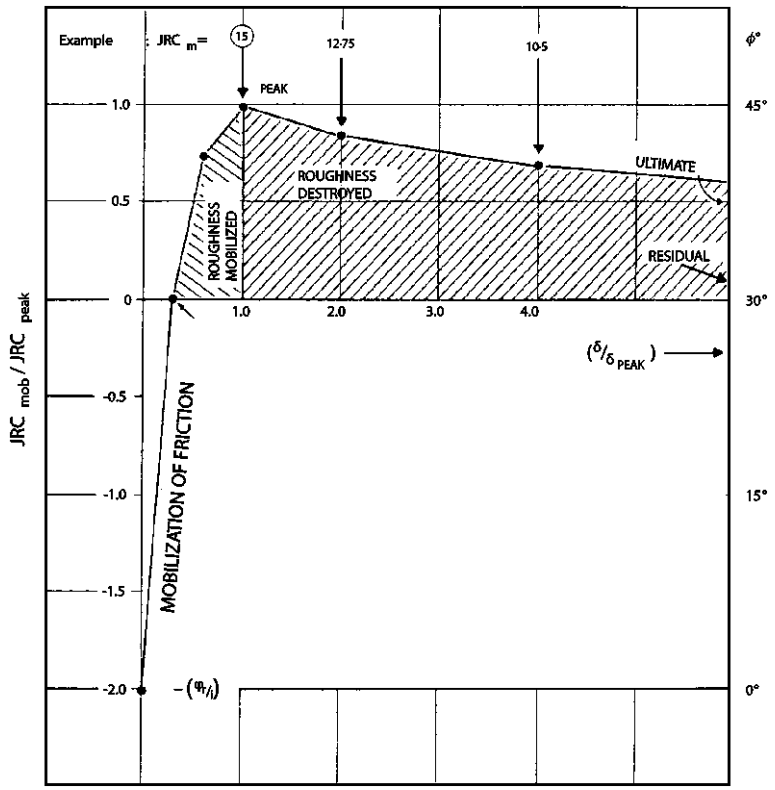

Figure 2-16: Normalized joint roughness–shear displacement relationship (Barton et al., 1985).

The concept defined in Barton's joint model is also applicable to test results of rocks. Most triaxial tests stopped the testing at a strain level which is far from reaching the true residual stress state because of the limitations of the test machines.

By using a servo-controlled and stiff load frame with two strain speeds (0.1 and 0.08 mm/minute), Rini and Mohd (2008) successfully tracked the complete stress – strain curve for intact samples of sandstone. Based on the discussion above, it becomes clear that the term "complete" in the previous statement is relative to the capabilities of testing setup. It should not be understood that the true residual rock strength can be obtained from a complete stress-strain curve presented by these researchers. As Figure 2-17 illustrates, at the post-peak stage, only when the failed sample is strained sufficiently, then the remaining load-bearing capacity can be

referred to as the residual strength of the rock. Most lab tests terminate the test without sufficient straining (strain level ε_0 in Figure 2-17) and the post-peak strength obtained from the data will be called the ultimate post-peak strength. One such an example can be seen in Figure 2-18b.

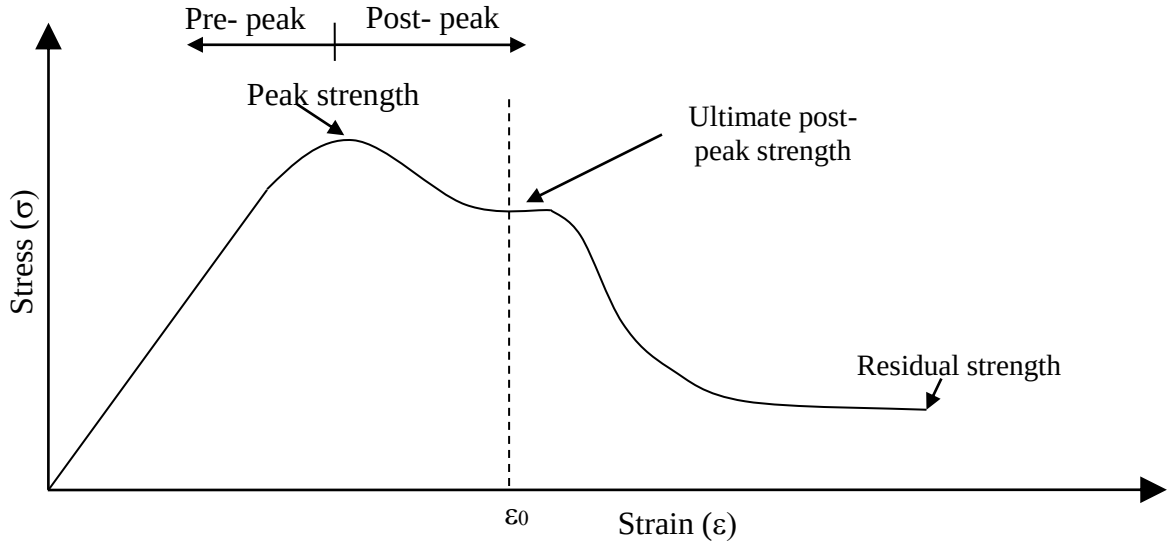

Figure 2-17: Complete stress – strain ($\sigma - \varepsilon$) curve of rocks.

Laboratory confined test results (Prince, 1979; Stavropoulou, 1982; Hsiao et al., 2011) show that the post-peak stage deformation behavior of rocks is confinement dependent. Under zero and low confinement conditions, the transition from peak strength to residual strength for hard rocks occurs in a sudden and perfectly brittle manner, as shown by Curve-A in Figure 2-18a. When the confinement (σ_3) is increased sufficiently, the brittle rocks may exhibit different degrees of brittleness, showing a strain-softening behavior (e.g., Curves-B, C, D, in Figure 2-18a). Seeber (1999) noticed that if the confining pressure was greater than one-fifth of the axial stress at failure, strain-softening was unlikely to occur. The true nature of a softening response is not known for large field-scale rock masses and is an ongoing topic of research at this time. Finally

when the confining pressure is high enough (the brittle-ductile transition limit given by Mogi (1966) is σ_3/σ_1=1/3.4), a ductile post-peak behavior might be observed (Curve–E in Figure 2-18a). Triaxial test data on marble by Wawersik and Fairhurst (1970) showed the confinement dependent post-peak behavior of marble (Figure 2-18b). By using radial strain controlled triaxial tests, Kovari and Tisa (1975) showed that the effect of confining stress on the post-peak behavior is more pronounced in soft rocks (e.g., sandstone and marble) than in hard rocks (e.g., Gotthard-granite). Similar observations by Stavrogin et al., (1982) shows that an increase in confining stress has more influence on the ductile behavior of sandstone than on the brittle behavior of Karoline granite.

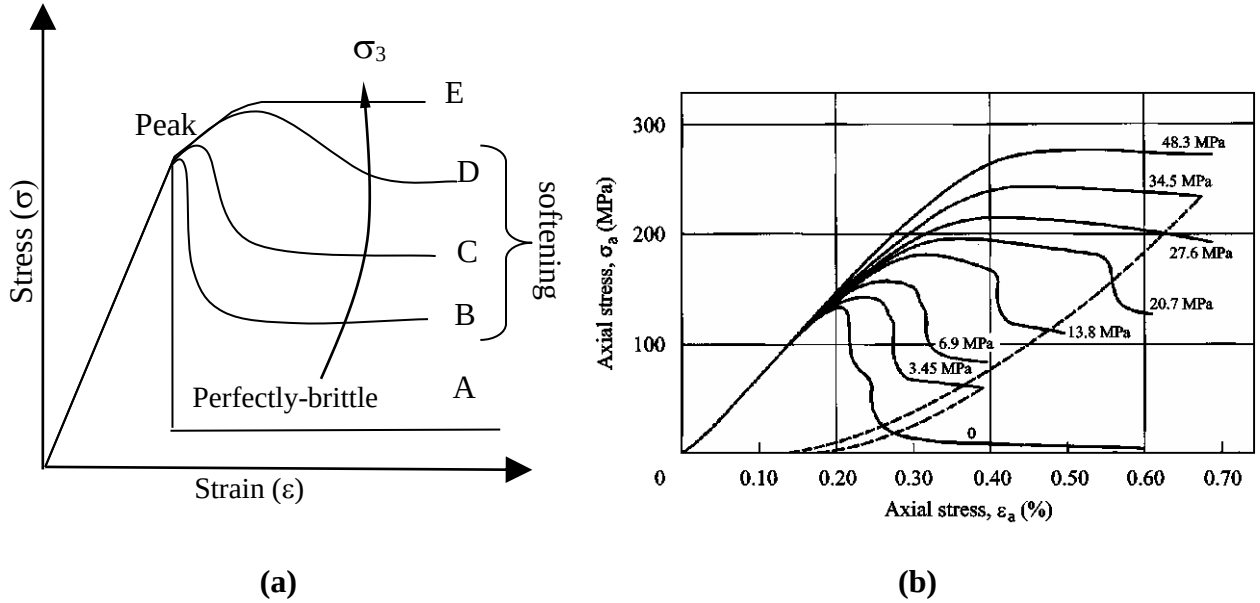

(a) **(b)**

Figure 2-18: (a) Influence of confinement on post-peak behavior of brittle rocks obtained from a strain-controlled test; (b) confinement dependency of post-peak behavior of marble (Wawersik & Fairhurst, 1970).

2.3.4. Using brittle rock strength parameters in numerical tools

So far, only the strengths of the intact rocks obtained from laboratory tests on cylindrical samples have been discussed. The discussion of the strength of the in-situ rock mass, however, is more complicated, and the most practical approach to estimate the in-situ rock mass strength is through back analysis of carefully documented case histories. Numerical modeling, which will be discussed in Chapter 4, is a useful tool for back analysis. Back analysis can be carried out by varying strength parameters so that the depth and shape of failure zones can be captured by the used modeling tool. It should be noted that the strength parameters used in these models are all apparent and they cannot be related to physical parameters of neither the rock mass nor the intact rock. However with some assumptions and simplification, along with a thorough knowledge of stress-related behavior of rock, these back analyzed strength parameters can be used in design if they are used consistently.

Most numerical modeling packages (e.g., FLAC, PHASE^2) define the rock strengths using two strength envelopes, one for peak and the other for "residual" (see Figure 2-19). In the example shown in Figure 2-19, the Mohr-Coulomb failure criterion is used and the peak and "residual" strength are defined by peak and "residual" cohesions and friction angles of 35 MPa, 22° and 1 MPa, 50°, respectively. According to the discussion presented in the previous section, the parameters used for the residual strength are not actually residual because of limited straining which can be excised in the numerical models. In a strict sense, they should be called ultimate or simply post-peak strengths.

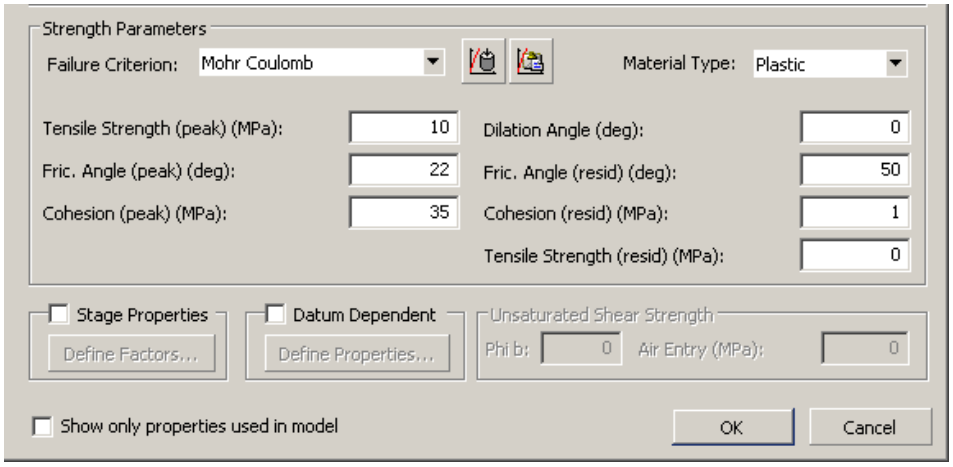

Figure 2-19: Interactive input frame for strength parameters of Mohr-Coulomb failure criterion in PHASE^2.

Based on the strength parameters, two straight lines can be drawn in the space of major and minor principal stresses (see Figure 2-20). The confinement that corresponds to the intersecting point of the two lines is noted as σ_0. At low confinement levels ($\sigma_3 < \sigma_0$), where failure at the boundary of tunnel often initiates, the steeper envelope defines the post-peak strength . The post-peak strength envelope passing through the origin accounts for a complete loss of the cohesive strength at the post-peak stage.

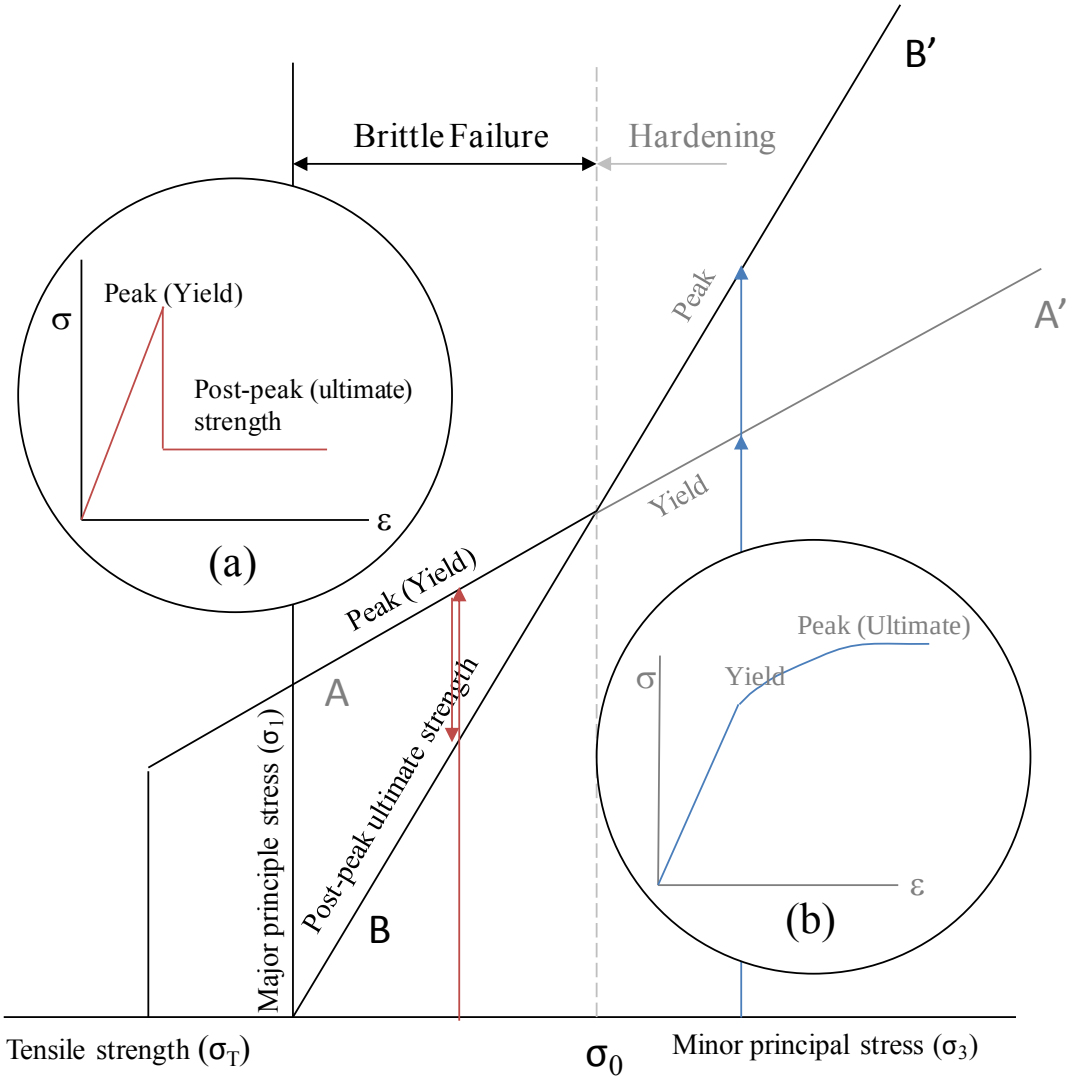

Figure 2-20: Sketch of two possible scenarios for the post-peak behaviors when the strength parameters are defined by two sets of strength parameters (peak and post-peak): (a) elastic-perfectly-brittle behavior; (b) elastic-hardening-ductile behavior.

If a brittle material model such as the one shown in Figure 2-18a is used, (at low confinement levels ($\sigma_3 < \sigma_0$)), once the stress reaches the peak strength envelope A , the model detects yielding and the stress will drop instantaneously to the post-peak ultimate strength envelope B . At higher confinement levels ($\sigma_3 > \sigma_0$), once the stress path reaches the yield (peak) strength envelope A', the model detects yielding and the stress move to the post-peak ultimate strength

envelope B'. Because the post-peak ultimate strength is higher than the yield (peak) strength, the material exhibits a strain hardening behavior. This type of hardening behavior (Figure 2-20) may be seen in materials such as steel but is certainly not a behavior for rocks. A ductile behavior in which the post-peak strength is equal to the peak strength is the closest behavior that can be expected from a rock at very high confinements.

Hence, defining peak and post-peak rock strengths by two sets of brittle strength parameters may violate commonly accepted rules and to capture the brittle rock failure well, a multi-line failure criterion may be required. However, the development of such a multi-line failure criterion requires extensive field and laboratory tests and is not the focus of this study. Fortunately, the focus of this study is on the rock failure near excavation boundary where the confinement is usually small ($\sigma_3 << \sigma_0$). As a precaution to use the brittle rock model, the modeler needs to make sure that the stress path will approach the peak (yield) envelope at the low confining stress zone. This phenomenon and the limitation of the model will be discussed further in 4.

2.4. Estimating brittle failure around underground openings

As mentioned in Chapter 1, it is important to support underground openings to provide a safe environment for workers. Engineers need to estimate the demands that will be placed on the rock support to design a support system that is comprised of rockbolts and surface retaining components. The demands on the rock support system include: (1) load, (2) displacement and (3) energy demands. In all cases, the designers need to know the depth of failure to calculate the weight of the rock that must be supported, to estimate the rock deformation considering rock

mass bulking, and to estimate the energy due to rock ejection that must be absorbed by the rock support system.

2.4.1. Depth of failure under static loading

The depth of failure is defined by either the geological structures (such as joints) that could potentially form unstable wedges or the depth of overstressed rock mass. The first case is frequently seen at shallow depth and the second one is often observed when mining in highly stressed grounds in massive hard rocks.

When an opening is excavated, the in-situ stress field is disturbed and when the stress reaches the strength of the rock mass, the rock will fail. Under static stress loading, the depth of failure in massive brittle rock is primarily governed by the rock strength, stress level, stress ratio (σ_1 / σ_3), and opening geometry. There are two approaches that can be used to estimate the depth of failure, and the methods in each approach are summarized below.

2.4.1.1 Estimating depth of failure using an empirical approach

Kaiser et al. (1996) established a semi-empirical relationship for estimating depth of failure of brittle rocks under static loading; this empirical relation was further refined by Martin et al. (1999) by adding additional data points. The results and data from published case histories in a wide range of rock mass conditions and in-situ stresses are plotted in Figure 2-21. Martin and Christiansson (2009) added the results from the Äspö pillar project to the previous case histories and found that the previously established empirical relation predicted the depth of failure reasonably well.

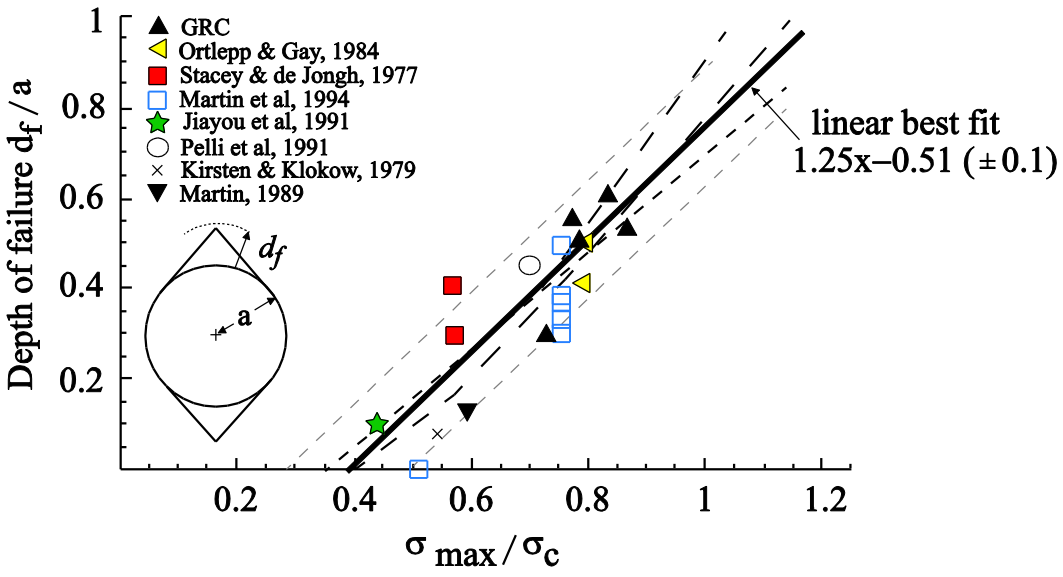

Figure 2-21: Empirical relationship used to estimate the depth of failure (Martin et al., 1999; Kaiser et al., 2000).

In this semi-empirical relationship, the maximum tangential elastic stress (σ_{max}) on the boundary of a circular opening in a continuous, homogeneous, isotropic and linearly elastic rock is expressed using the well-known Kirsch equation $\sigma_{max} = 3\sigma_1 - \sigma_3$, where σ_1 and σ_3 are the maximum and minimum principal stresses, respectively. The maximum compressive strength of the intact rock (σ_c) is obtained from laboratory testing. There are other equivalent equations available based on different strength factors (strength of the rockmass or strength of the intact rock samples, e.g. spalling by Martin and Christiansson (2009)). These equations are all essentially based on data fitting using data from previous case studies. Figure 2-21 illustrates that for a range of stress ratios from 0.4 to 1.0, the maximum depth of failure is well predicted using the linear best fit line.

2.4.1.2 Estimating depth of failure using numerical modeling

As an alternative approach, the depth of failure and the geometry of the failure zone can be simulated by numerical modeling. Several numerical approaches have been used to simulate the behavior of brittle rocks around underground openings. In general, these approaches can be categorized into two broad classes: continuum and discontinuum methods. The results for simulation of the failure zone using discontinuum method (UDEC, 3DEC, etc), where the failed elements are allowed to display large deformation, can be representative of the slabbing process in the field. However these results can be influenced by the predefined properties of discontinuities within the model and the joint geological parameters. The continuum approach, on the other hand, does not allow the failed elements to fully displace and the method relies on using specific failure models to determine the distribution of the stress-induced failure.

The mechanical behavior of intact rocks under compressive loading is complex as summarized in Section 2.3. When modeling the stress-induced rock failure, it is important to assign strength parameters and boundary conditions properly. For the examination of the non-failed part of the rock mass, elastic analysis is a preliminary approach for estimating the maximum stress concentration at the perimeter of a tunnel. However, as an elastic material will not undergo any plastic deformation, this method has serious shortcomings when it comes to the accurate simulation of the breakout zone where plastic deformation takes place (Read, 1994; Martin, 1997). Simple failure models such as the elastic-perfectly-plastic model have been used to account for the effect of plastic straining on the stress distribution. However, this model is not suitable for brittle rocks and it underestimates both the depth and extent of the failed zone in the compression zones, where the notch breakouts eventually form (Hajiabdolmajid et al., 2002).

Martin (1997), Hajiabdolmajid et al. (2002), Diederichs (2007) and others (Martin, 1993; Read, 1994; Edelbro, 2010) proposed several modeling approaches to model the failure of brittle hard rocks, primarily based on field observation at the URL Mine-by tunnel. These approaches were developed by calibrating the yielded elements in the models with the in-situ observations of the depth, extent, and the geometry of the brittle failure zone. In the next sections, the most commonly adopted approaches for simulating brittle rock failure are reviewed.

2.4.1.2.1 Plastic strain-dependent cohesion-weakening frictional-strengthening model

Martin (1997) demonstrated that brittle rock failure is a gradual process of cohesive strength weakening by tensile cracking at the early stages of loading, and mobilization of the frictional strength component when the cohesive strength component is significantly reduced. Therefore, a constitutive law that captures the cohesion loss and frictional strength mobilization should be able to simulate the brittle rock failure process. Hajiabdolmajid et al. (2002) adopted a plastic, strain-dependent, cohesion-weakening frictional-strengthening (CWFS) model in FLAC where the post-peak cohesion and friction angle were assigned to the model as a function of plastic shear strain as shown in the inset in Figure 2-22a. Using the CWFS model and the strength parameters calibrated, Hajiabdolmajid et al. (2002) were able to simulate successfully the V-shaped notches observed at the Mine-by tunnel (Figure 2-22a).

In the original study by Hajiabdolmajid et al. (2002), the effect of the excavation method is ignored by instantaneous nullification of the tunnel core material. Cai (2008) demonstrated that the selected method to represent the excavation method can significantly influence the simulated tensile failure on the side walls. The profile of the failure zone illustrated in Figure 2-22a is reproduced by a linear reduction of the Young's modulus of the core material in ten stages to

simulate the gradual tunnel advancement. Compared with the failure zone distribution by Hajiabdolmajid et al. (2002), the failure zone shown in Figure 2-22a eliminates the tensile failure along the tunnel perimeter but retains the notch shape which matches the field observation well.

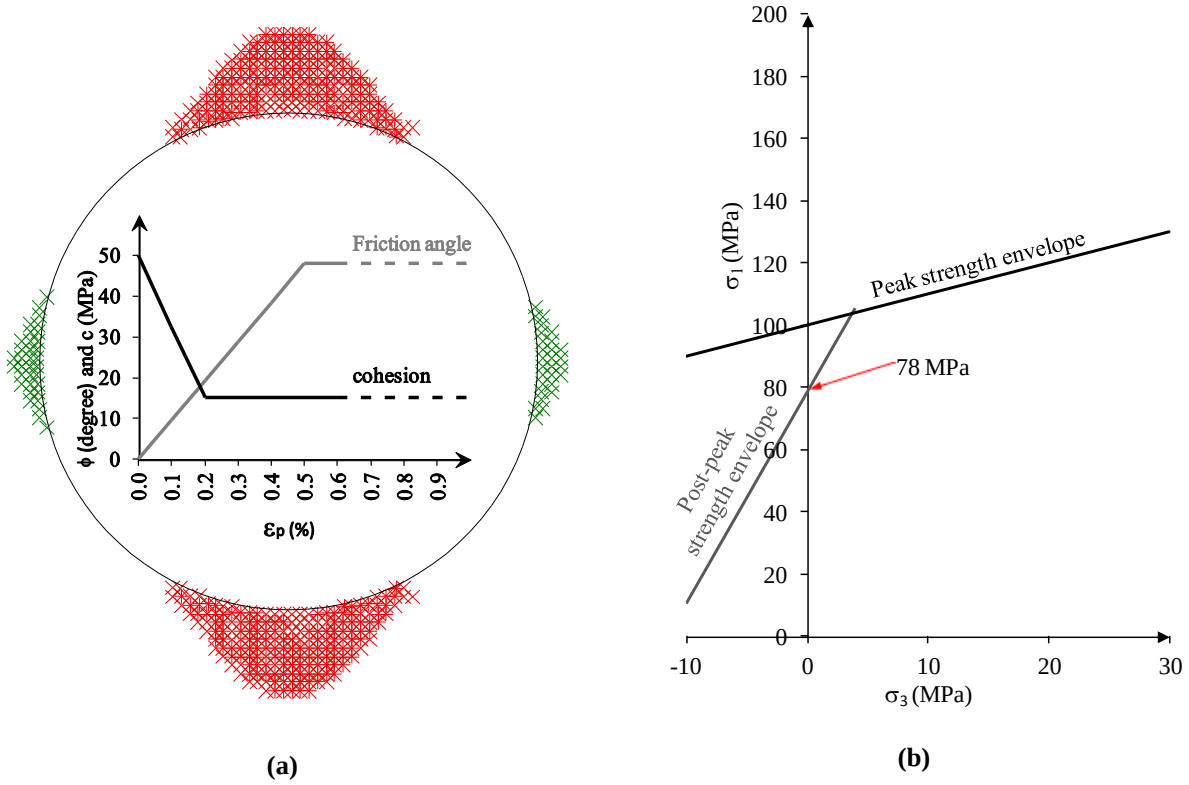

(a) **(b)**

Figure 2-22: (a) Simulation of the V-shaped notches by the CWFS model in FLAC (reproduced from Hajiabdolmajid et al., 2002); red and green color × indicate the elements failed in shear and tension, respectively; (b) Strength envelopes used in the modeling by Hajiabdolmajid et al. (2002).

The CWFS model incorporates a strain-softening behavior at the post-peak stage. The apparent peak and post-peak strength envelopes assigned to the CWFS strain-dependent approach are plotted in Figure 2-22b. The apparent peak uniaxial compressive strength of the rock mass in this model is 100 MPa; this stress level is equivalent to the crack initiation (0.47 UCS) threshold of the intact rock. On the other hand, the apparent post-peak compressive strength of the rock mass

at zero confinement (as is the case for the rocks at the perimeter of the tunnel), based on the model parameters defined in Figure 2-22a, is 78 MPa.

2.4.1.2.2 Spalling failure modeling approach

Diederichs (2007) proposed a set of spalling failure parameters to simulate brittle rock failure and tested the approach using the breakouts observed at the Mine-by tunnel. The simulation was conducted using PHASE^2 utilizing the generalized Hoek-Brown failure criterion defined by two different curved envelopes for the peak and post-peak strengths as shown in Figure 2-23. As illustrated in Figure 2-23, the notch breakout is captured accurately using the spalling failure parameters.

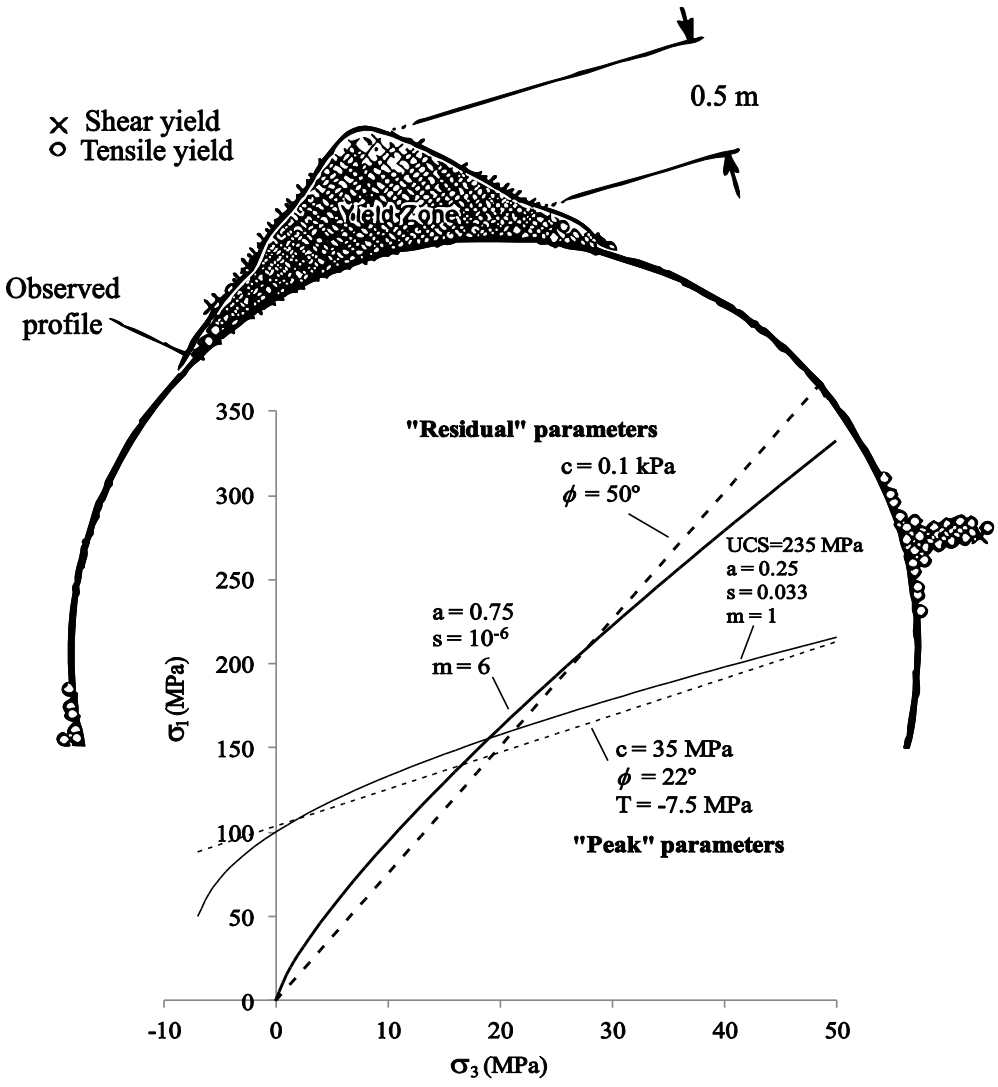

Figure 2-23: Strength envelopes defined by spalling failure parameters and the predicted breakout at the Mine-by tunnel (Diederichs, 2007).

When realized in PHASE^2, as long as the stress path of an element reach the apparent peak strength envelope in the low confinement zone (see Figure 2-20), this model shows the elastic-perfectly brittle-plastic behavior. In the high confinement zone (σ_3 > 18.5 MPa), the model shows a post-peak hardening behavior.

In this approach, the apparent post-peak strength envelope is defined by a low *s* value and a high *m* value (as well as a high *a* value), resulting in an apparent post-peak $\mathrm{UCS} \cong 0$. The apparent peak strength is defined by a set of parameters: intact rock UCS = 235 MPa, *m* = 1, *s* = 0.033, *a* = 0.25 (*m*, *s*, and *a* are Hoek-Brown failure criterion parameters), resulting in an apparent peak strength envelope similar to that defined by the strain-dependent CWFS model (with an apparent peak $\mathrm{UCS} \cong 100$).

It is observed that the models used by Hajiabdolmajid et al. (2002) and Diederichs (2007) have similar apparent peak strength envelopes but their apparent post-peak strength envelopes are different; yet both models capture the failure zone of the Mine-by tunnel satisfactorily. Diederichs' modeling approach is further discussed in Chapter 4.

2.4.1.2.3 Plastic strain independent (instantaneous) cohesion-weakening frictional-strengthening model

Edelbro (2010) utilized an approach in FLAC which was similar to the spalling failure approach proposed by Diederichs (2007) to simulate brittle rock failure. Instead of using Hoek-Brown's strength parameters, Mohr-Coulomb's strength parameters were used in the simulation. Edelbro (2010) claimed that the maximum shear strain obtained from this modeling approach provided a reliable indicator for predicting compression failure-induced fallouts. Some modelers (Martin, 1995; Castro, 1996; Hajiabdolmajid, 2001) use the yielding zone to represent the rock failure (fallout) around excavations. However, Edelbro (2010) found that the region of yielded elements (either in tension or shear) over predicted the depth of failure in this approach. The results of

Edelbro's study showed that the region of yielded elements represents the damaged rock than a fallout region.

2.4.2. Depth of failure under dynamic loading

In modern deep-level mining, seismic events always occur suddenly and they potentially threaten the lives of workers. Case histories summarized in Section 2.2.2 revealed that remote seismic events or large production blasts may add an increment of dynamic stress to the in-situ or mining-induced stresses and provide additional strain energy to the rock fracturing process, leading to more failure around the opening. It is important to design rock support with enough support capacities to control the damage due to dynamic loading. As discussed earlier, only a reasonable estimation of the depth of failure may help with support design.

There are two methods for estimating the depth of failure resulting from additional dynamic loading. The first method uses an empirical relationship based on previously well-documented case studies of the rockburst events with different event intensities and rock mass strength. The second method uses numerical modeling to investigate the effect of additional dynamic stress wave loading to underground openings.

2.4.2.1 Estimating depth of failure under dynamic loading using empirical approach

It is essential to approximate the intensity of ground motion due to a seismic event to estimate the ultimate depth of failure resulting from a seismic event. Based on the expected seismic event magnitude and location, and by incorporating a scaling law (Kaiser et al., 1996), the intensity of ground motion along the drifts, normally expressed as Peak Particle Velocity (*ppv*), can be determined. Because the *ppv* of the p-wave (compressive wave) is much lower than the *ppv* of

the s-wave (shear wave), designers primarily consider the effect of the s-wave. From the seismic design criteria for the LA Metro project (Wang, 1993; SCRTD, 1984), it was numerically determined that a shear wave propagating at 45° (angle of incident) to the tunnel axis would create the most critical impact within the tunnel structure. The most destructive effect of a seismic event on rock failure can finally be predicted by superimposing the static and dynamic stresses (Kaiser et al., 1996).

Using the empirical relationship (Figure 2-21) to estimate the depth of failure under static stress conditions and in combination with a calculated dynamic stress increase, it is possible to assess the impact of stress change on the depth of failure. The dynamic stress change due to an s-wave is calculated by $c_s \rho.ppv_s$, where c_s is the shear wave velocity, ρ is the density of the rock, and ppv_s is the peak particle velocity of the shear wave. The static in-situ stress is altered by $\Delta\sigma_1^d = c_s \rho.ppv_s$ and $\Delta\sigma_3^d = -c_s \rho.ppv_s$. Due to sign reversal, the principal stress difference is twice as large as the peak dynamic stress increment (Kaiser et al., 1996). Accordingly, when the shear wave reaches the opening from a critical 45° angle, the maximum dynamic stress change for a circular-shape tunnel is calculated from Eq. (4).

$$\Delta\sigma_{\max}^d = \pm 4 c_s \rho.ppv_s \tag{4}$$

This maximum dynamic stress is added (or subtracted) to (from) the maximum tangential static stress in Eq. (5) to estimate the depth of failure under dynamic loading by using Eq. (6) (Kaiser et al., 1996)

$$\sigma_{\max} = 3\sigma_1 - \sigma_3 \pm 4 c_s \rho.ppv_s \tag{5}$$

$$\frac{d_f}{a} = 1.25\frac{\sigma_{\max}}{\sigma_c} - 0.51(\pm 0.1) \tag{6}$$

In Eq. (6), d_f is depth of failure, a is the radius of the circular tunnel, $\sigma_{\max}$ is obtained from Eq. (5) and stands for the maximum tangential stress at the boundary of the circular tunnel and finally, σ_c is the maximum compressive strength of the intact rock samples. The dynamic stress can reverse the stress pulse and hence can reduce the maximum stress concentration; and it may also cause tensile stresses, assisting the unraveling process. Based on Eqs. (5) and (6) and a variation of ppv_s values, Figure 2-24 can be plotted to estimate the maximum depth of failure under dynamic loading with different intensities of ground motion.

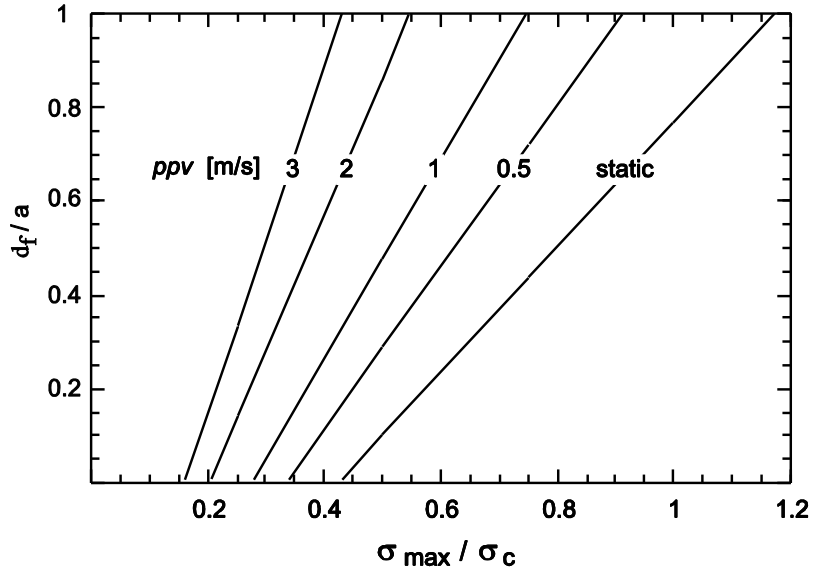

Figure 2-24: Maximum radius of failure under dynamic loading conditions (Kaiser et al., 1996).

This graph was empirical and was verified by numerical modeling using FLAC (Vasak & Kaiser, 1995). The process of static and dynamic stress-induced failure can be investigated with the use of numerical models that can follow the process of progressive brittle failure and allow load

transfer from the failed elements onto other elements until an equilibrium is established. However, it needs to be noted that continuum modeling provides only an approximation of this process; these models do not simulate the transition from continuum to discontinuum of the rocks.

2.4.2.2 Estimating depth of failure under dynamic loading using numerical modeling

Apart from the elastic solutions that are also applicable to the static problems (Examine2D, Examine3D, ExamineTAB and Map3D), ground control engineers require a practical solution for the estimation of the depth of failure under dynamic loading where plastic deformation occurs.

Few efforts had been devoted to modeling rock failure related rock bursting because all available continuum models simulate shear failure and cannot reproduce spalling process satisfactorily. A few reports were summarized in the *Canadian Rockburst Research Handbook* (Graham, 1995), some of which are mentioned here. A three-dimensional nonlinear distinct model with the capability of simulating discontinuities (3DEC (Itasca, 1993)) was used to model the faulting which transected a sill pillar area in Falconbridge's Lockerby mine (Urbancic, 1993). Followed by that, modeling of a sill pillar at Brunswick mine using BEAP (three-dimensional, linear boundary element model) was conducted by Kristof (1995) to estimate stress changes due to blasting. The stress analysis results were later verified by 3DEC modeling. A series of elastic analyses were conducted at both Creighton mine in Sudbury and Campbell mine in Red Lake, Ontario (Kazakidis, 1995; Grabinsky et al., 1995; Wiles & MacDonald, 1988). Most of these studies however concentrated on the mine stope sequencing and its effect on the mining-induced

stress. One study focused on the direct influence of mining-induced rockbursting on dynamic stress-induced rock failure around underground openings in El Teniante mine (Vasak & Kaiser, 1995).

In the study by Vasak and Kaiser (1995), a two-dimensional, plane-strain FLAC model with a plane shear wave input (50 Hz) was used to simulate dynamic loading-induced damage. Appropriate boundary conditions were selected to avoid reflections and leakage of stress waves. A calibrated strain-dependent Mohr-Coulomb failure criterion was used to simulate the rock failure. In this model, a CWFS approach was used and the failed rock mass stress near the wall reached a small post-peak strength value.

With the principal in-situ stresses (σ_1 = 24.8 MPa, σ_3 = 12.6 MPa), static stress analyses were conducted in this study to reproduce the results by (Vasak & Kaiser, 1995). Figure 2-26a presents the contours of σ_1-σ_3 under the elastic condition. It is seen that the highest tangential wall stress is about 75 MPa on the floor corner where notch overbreak eventually formed. On the other hand, the peak strength (cohesion dependent only), as summarized in Table 2-3, is 50 MPa. Hence, failure will occur if plastic modeling is conducted (Figure 2-25a).

Table 2-3: Strength parameters used in study by Vasak and Kaiser (1995)

	Plastic strain (%)	Peak	Post-peak
Cohesion (MPa)	0.2	25	2.5
Friction angle (°)	0.2	0	35
UCS (MPa)		50	9.6

In Vasak and Kaiser's study the shear stress wave, from a semi-artificial magnitude event (50 Hz sinusoidal wave with *ppv* = 1 m/s), results in failure of the rock mass surrounding the opening. By repeatedly applying four cycles of input shear wave, the failure zone further increases to the state shown in Figure 2-25b.

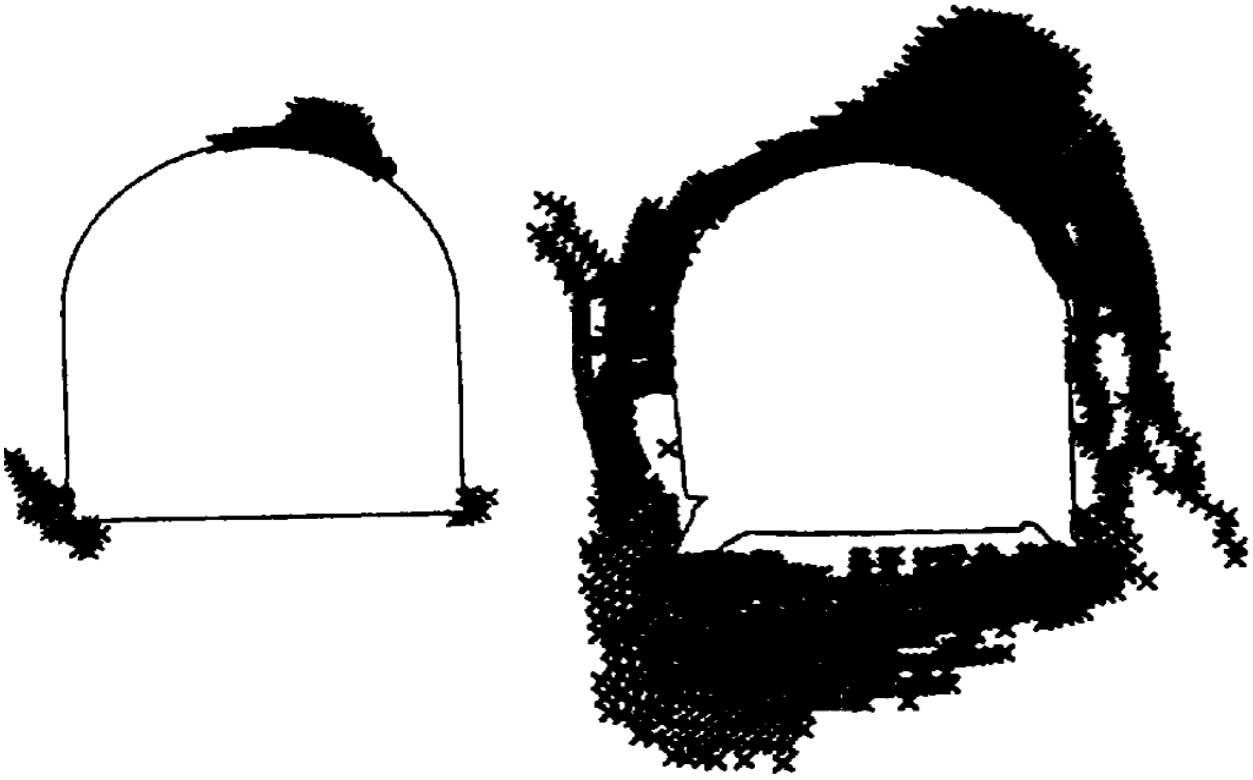

(a) **(b)**

Figure 2-25: Accumulated yielded elements caused by: a) static loading; b) repeated 1 m/s *ppv* sinusoidal wave loading (Vasak & Kaiser, 1995).

The simulated failure zone under static stress loading is reproduced and shown in Figure 2-26b. The depth of failure shown in Figure 2-25a, which was caused by a static loading, is similar to the static depth of failure shown in Figure 2-26b.

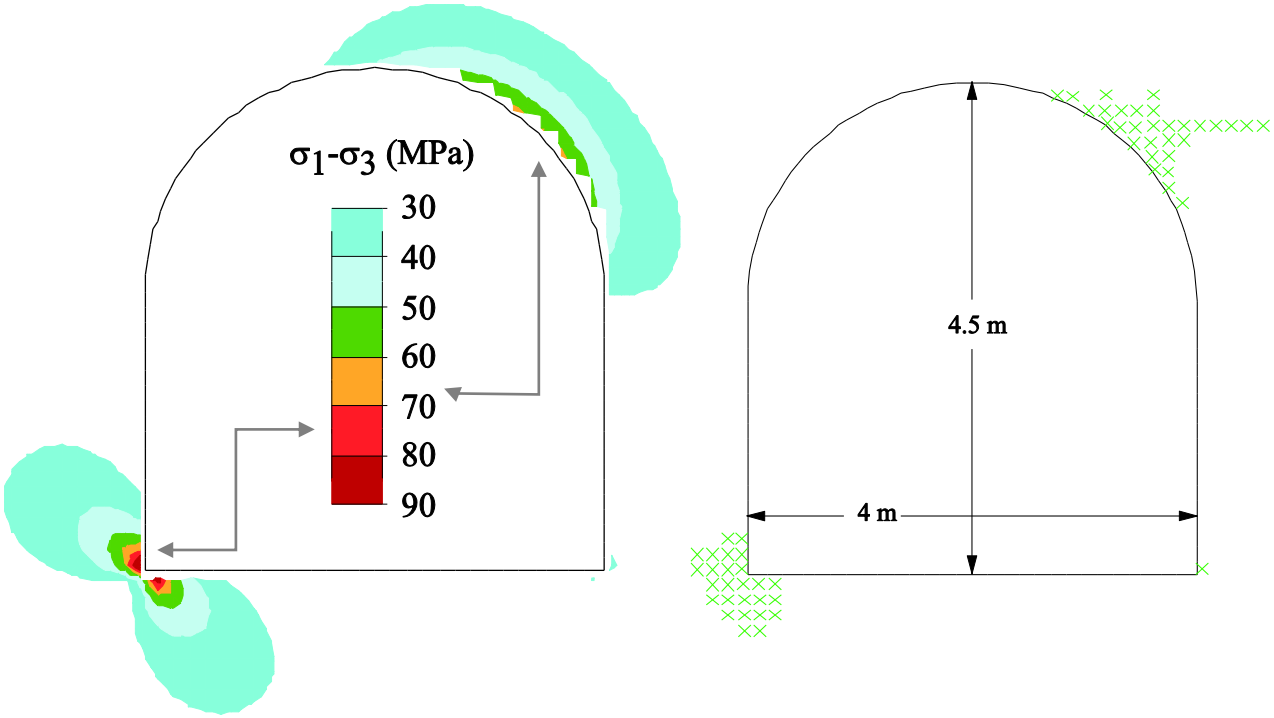

Figure 2-26: (a) Contours of tangential stress from an elastic analysis; (b) failure zone from a plastic analysis reproduced by using data from the El Teniente case study (Vasak & Kaiser, 1995).

The results from the study by Vasak and Kaiser (1995) verified the empirical dynamic depth of failure relationship (Eqs. (5) and (6)) discussed above. Vasak and Kaiser (1995) also conducted a sensitivity analysis of different rock mass strengths (cohesive strengths) ranging from 21 to 37 MPa; only when the rock mass strength is low enough can the shear stress wave causes the amount of failure that matches the empirical relationship.

2.5. Summary

A literature review on some of the previously published documents that covered the topic of brittle rock failure was conducted:

- First, some of the well-documented case studies that experienced brittle rock failure under static and/or dynamic loading were summarized. The importance of conducting this research to estimate the depth of failure zone around the tunnel boundary for rock support design can be seen through such a literature review effort. Most importantly, dynamic loading from a seismic event can change the stress conditions and cause additional failure zone in the perimeter of the tunnel. This calls for additional study on "rockburst support design", which is an ongoing topic of research for decades (Hedley, 1992; Stacey & Ortlepp, 1993; Kaiser et al., 1996).
- Second, the general procedure in laboratory strength measurement tests was discussed to understand the stress-related behavior of intact rock samples. It was clear that data obtained from laboratory tests do not represent the rockmass behavior in the field; however, the knowledge gained from the laboratory tests can be useful in engineering design utilizing numerical tools.
- Finally, some of the most common modeling approaches to model brittle rock failure were summarized. The cohesion-weakening and friction-strengthening (CWFS) model is well-recognized and widely used in simulating rock failure (Vasak & Kaiser, 1995; Hajiabdolmajid et al., 2002; Cheon et al., 2006; Zhao et al., 2010; Oliveira, 2012). In particular, this approach was successfully applied to simulate the brittle rock failure observed at the Mine-by tunnel (Hajiabdolmajid et al., 2002). As an alternative approach, Diederichs (2007) used an elastic-brittle-plastic failure model with the Hoek-Brown strength parameters to simulate brittle rock failure in PHASE^2. All these continuum modeling approaches simulate the shear failure and cannot capture rock spalling which is a discontinuum process. This is acceptable for

engineering design as long as the models and the associated model parameters are used consistently.

There are still opportunities for enhancement of brittle rock failure simulation using the continuum modeling approach, under the static and dynamic loading conditions. Some numerical modeling work is conducted in Chapters 4 and 5 focusing on the influence of strength parameters and the post-peak behavior on the rock failure under static and dynamic loadings, respectively. Other parameters involved when modeling brittle failure around underground excavations, such as mesh size and excavation simulation methods are also studied in these chapters.

Chapter 3

Modeling brittle rock behavior in compression test

3.1. Introduction

In low confinement environments, particularly such as those encountered around the periphery of underground openings, rock failure can happen in a brittle manner. This type of material behavior is mostly attributed to the sudden reduction in the strength of the material at the onset of failure (Martin, 1995; Kaiser et al., 2000).

In determining the strength of a rock, two parameters, one for cohesive strength and the other for frictional strength (c and ϕ), are used in the Mohr-Coulomb failure criterion. This failure criterion defines failure in the stress space, not in the strain space; the reason is mainly that strength can be directly compared with the calculated stress. The Mohr-Coulomb failure criterion is available in most geotechnical software packages such as PHASE^2 and FLAC.

In PHASE^2, with an elastic-brittle-plastic material model, users can define only the peak and "residual" strength parameters, which can present a problem when the slope of the post-peak strength envelope is higher than that of the peak one, as discussed in Chapter 2. In addition, plastic strain-dependent strain softening model is not available in PHASE^2. In FLAC, users can use the plastic strain-dependent Mohr-Coulomb failure model. The cohesive and frictional strength values are assigned to a table based on the amount of plastic strain and the corresponding strength components in the strain-dependent model. This provides great flexibility to users because all the rock behaviors shown in Figure 2-18a can be modeled using the strain-dependent model in FLAC.

In this chapter, some factors for modeling brittle rock behavior using FLAC are investigated. Specifically, the effect of peak and the post-peak strength parameters, plastic strain, and

confining stress are studied in a small scale model representing a laboratory compression test. The purpose of this exercise is to better understand the rock behavior and prepare to make an attempt to simulate the depth of failure around the excavation boundary in the next chapter.

3.2. Defining post-peak material strength parameters

The strain-dependent strength parameters at the post-peak stage are a function of accumulated plastic strain. In the built-in strain-dependent Mohr-Coulomb failure model in FLAC, each strength parameter (cohesion, friction, and dilation angle) can be corresponded to the accumulated plastic strain shown in Table 3-1.

Table 3-1: Tables of strength parameters in the strain-dependent failure model in FLAC

Characteristic Plastic strain (s)	Plastic strain (%)	Cohesion (Pa)	Plastic strain (%)	Friction angle (Pa)
	0	C_{Peak}	0	ϕ_{Peak}
	$\varepsilon_p^{Post\text{-}peak\ 1}$	$C_{post\text{-}peak\ 1}$	$\varepsilon_p^{Post\text{-}peak\ 1}$	$\phi_{post\text{-}peak\ 1}$
	$\varepsilon_p^{Post\text{-}peak\ 2}$	$C_{post\text{-}peak\ 2}$	$\varepsilon_p^{Post\text{-}peak\ 2}$	$\phi_{post\text{-}peak\ 2}$
	...	...	...	...
	$\varepsilon_p^{Post\text{-}peak\ n}$	$C_{post\text{-}peak\ n}$	$\varepsilon_p^{Post\text{-}peak\ n}$	$\phi_{post\text{-}peak\ n}$
	1	$C_{residual}$	1	$\phi_{residual}$

The user can define a linear or non-linear relationship between the accumulated plastic strain and each strength parameter (Table 3-1). In order to avoid unnecessary complications throughout this study, a bi-linear relationship is chosen, which requires only a single value for the characteristic plastic strain for both *c* and ϕ. The peak strength parameters are assigned to the model as long as the material behaves elastically and no irreversible deformation has taken place. When the plastic strain is equal to or greater than the characteristic plastic strain $\varepsilon_p \geq \varepsilon_p^{residual}$, the post-peak values

of strength parameters are assigned to the model ($c_{\text{post-peak}}$, $\phi_{\text{post-peak}}$). If the accumulated plastic strain is smaller than the characteristic plastic strain ($0 < \varepsilon_p < \varepsilon_p^{residual}$), linear interpolation is conducted to calculate the corresponding friction angle and cohesion values between the peak and "residual" values.

The linear interpolation is further discussed here using an example. As illustrated in Figure 3-1, the input table for the cohesion values suggests that at a characteristic plastic strain of 0.5%, the cohesion changes from a peak value of 50 MPa to a "residual" value of 15 MPa. In the calculation, if the plastic strains are 0.2% and 0.3%, the interpolated cohesion value becomes 36 and 29 MPa, respectively. These updated values are then stored for calculating the strength in the next time step. When the plastic strain reaches 0.5%, the cohesion is kept constant at its "residual" or ultimate value.

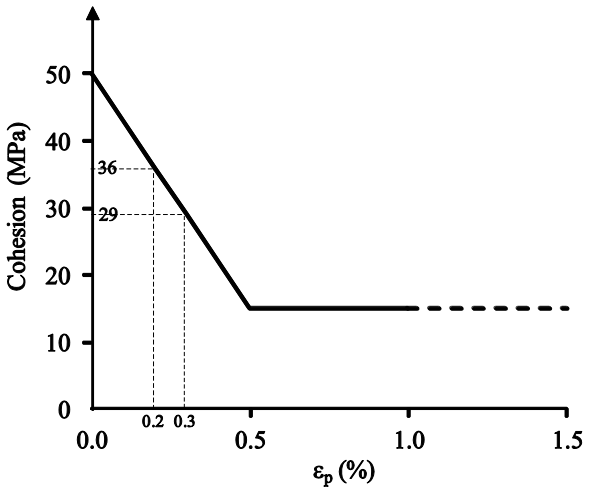

Figure 3-1: Linear interpolation of cohesion strength parameter.

A very small characteristic plastic strain should be used for simulating brittle rock behavior. In the behavior of perfectly brittle-plastic rocks, the characteristic plastic strain is zero. This is not

possible to achieve in FLAC modeling. However, an extremely small characteristic plastic strain can be set to approximate the perfectly brittle rock behavior.

3.3. Simulation of uniaxial compression test

A trial run of a uniaxial compression strength simulation in plane-strain was conducted using FLAC to investigate the elastic-perfectly brittle-plastic behavior. In this section, a simple 10×5 rectangular grids was considered and homogenous material properties were assigned to all the elements. For a simple UCS geometry, the mesh and discretization density were investigated by smaller dimensions and a more dens grid while observing an identical behavior. The goal was to study the influence of strength parameters on the material response. The model dimension, meshing, and boundary condition are illustrated in Figure 3-2. For simplicity, Young's modulus and Poisson's ratio were kept as constants and their values are 60 GPa and 0.25, respectively.

In all numerical experiments of uniaxial compression tests on rock specimens, axial load was applied with a vertical downward displacement which was applied to the top boundary to simulate displacement-controlled loading. The loading speed (velocity) was kept constant at 10^{-10} m/step. This loading rate was selected after a series of rate dependency tests which confirm that the simulation results were not influenced by this factor. The lower boundary was fixed in the Y direction and the lower left grid point was fixed in both directions. In this continuum model, the stress distribution was uniform in all the elements (this has been verified by selecting a few recording points at different locations in the model and tracking an identical stress change as loading was applied). In the following discussion, the middle element of the model (P.1 in Figure 3-2) was used to track the history of stress changes in all simulations.

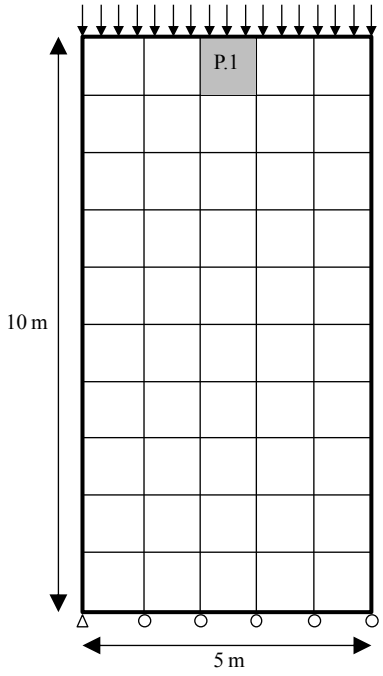

Figure 3-2: The model grid used in the simulation of uniaxial compression tests (P.1 is used to track the stress history).

The stress state of the model can be affected by changing the strength parameters and loading condition. The stress path analysis is a commonly used technique to monitor the stress change as loading conditions change; it plots the changes of σ_1 and σ_3 in all loading steps. Another monitoring method is plotting the stress-strain curve. This relationship is found by recording the amount of strain with the corresponding stress. The stress-strain curve can then be utilized to distinguish a perfectly brittle material response from a strain-softening or a ductile material response.

Figure 3-3a illustrates that the stress path is influenced by the degree of material softening defined by the characteristic plastic strain. Once the stress path reaches the peak envelope, a sudden transition of the stress path to the post-peak envelope occurs for the brittle material with a small characteristic plastic strain of $\varepsilon_p = 10^{-10}\%$. An elastic-perfectly brittle-plastic material

requires a simultaneous reduction in the cohesion and increase in friction angle once the rock fails. As mentioned above, FLAC does not allow the user to set the characteristic plastic strain to zero; therefore, a small value of 10^{-10}% is used here to simulate brittle failure. This small plastic strain value is assigned to both cohesion and friction angle (Table 3-1). No significant change in material brittleness is observed for characteristic plastic strain values smaller than $\varepsilon_p = 10^{-10}$%. Therefore, a rock with a characteristic plastic strain of 10^{-10}% is referred to as brittle rock throughout this study. The stress-strain curves in Figure 3-3c indicate that by assigning different characteristic plastic strains to the material table in FLAC (e.g., 10^{-10}%, 0.05% and 5%), the post-peak material behavior can vary from brittle to strain-softening.

When using the strain-dependent failure model with a high characteristic plastic strain (Figure 3-3b), a large plastic strain is required before the "residual" or ultimate strength is reached. For a characteristic plastic strain equal to 0.5%, the stress level does not reach the "residual" strength of 43 MPa even when the directly measured vertical strain is 2% (see Figure 3-3c)

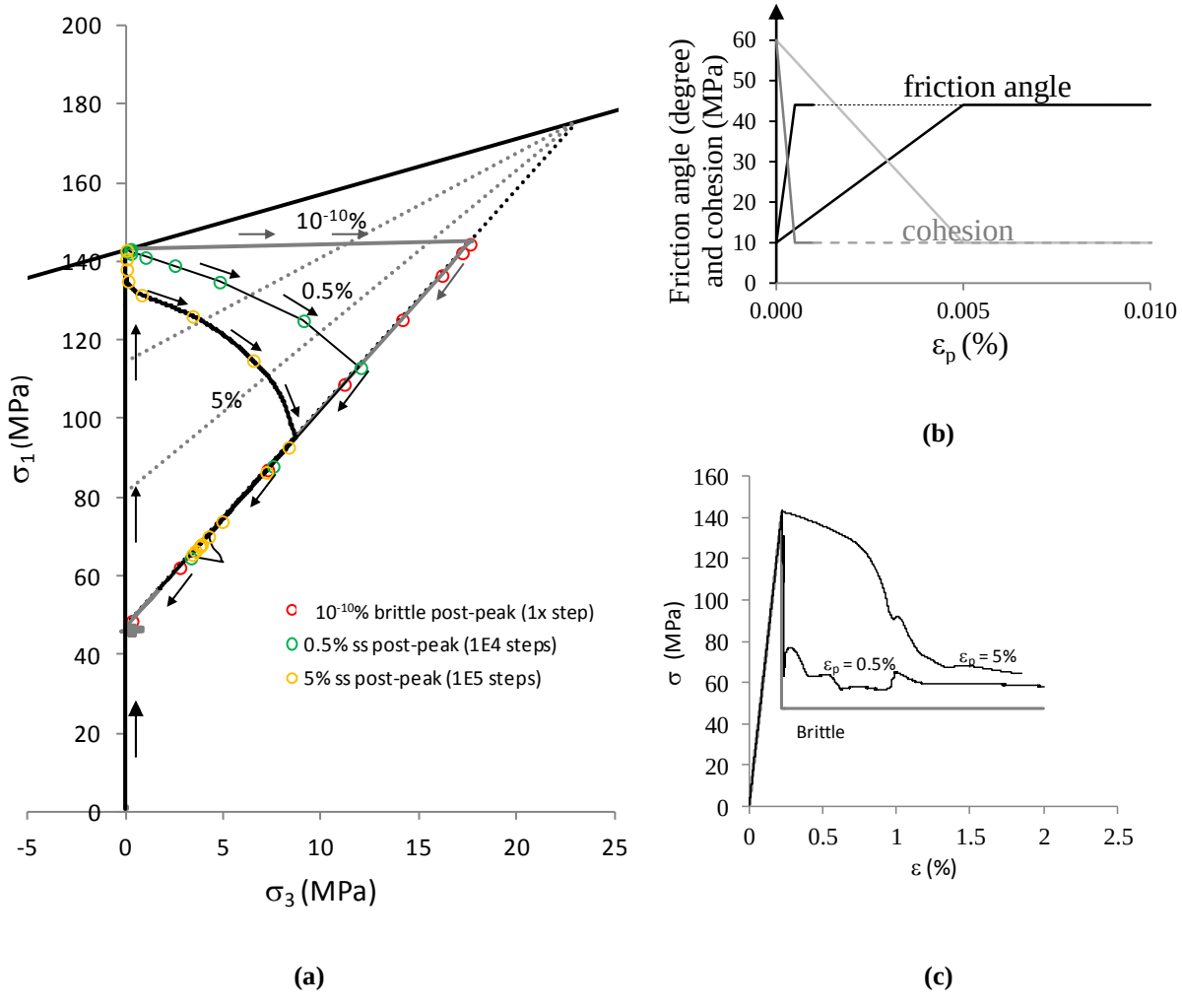

Figure 3-3: (a) Simulated stress paths for the numerical models of a strain softening material under uniaxial compression with three different brittleness levels defined by the characteristic plastic strains (10^{-10}%, 0.5%, 5%); (b) simultaneous mobilization of cohesion and friction angle as a function of plastic strain; (c) stress-strain curves for three different characteristic plastic strains.

As observed in Figure 3-3a, a few stress points are not perfectly aligned on the post-peak strength envelope. In FLAC, a stress point can deviate from the yield surface if there is hardening or softening involved, because the update of the yield function is one time-step behind the current one. In this case, the deviations are usually small because of the small time-steps used in FLAC (Itasca, 2002).

The linear peak strength envelope of a Mohr-Coulomb failure model is defined by combining two strength components, the peak cohesion and the peak friction angle. During a UCS test, Eq. (7) can be used to calculate the maximum compressive strength. The maximum principal stress may not exceed this value under any circumstances. For example, by assigning peak strength parameters for the cohesion and the friction angle to 60 MPa and 10°, respectively, the peak UCS obtained from Eq. (7) is 143 MPa. Therefore, during a UCS test simulation when no confinement is applied to the model, the major principal stress should not exceed 143 MPa regardless of the post-peak strength parameters or characteristic plastic strain assigned to the model (see Figure 3-3a and Figure 3-4a).

$$\sigma_c = \frac{2c\cos\phi}{1-\sin\phi} \tag{7}$$

As observed in Figure 3-3a, once the stress state reaches the peak strength envelope, a sudden and transient increase in the minimum principal stress (σ_3) occurs in a brittle material. For instance, the stress state reaches the peak strength at a minimum principal stress of zero; then at the next time step, the stress state lies on the post-peak strength envelope. When the stress state changes from the peak to the post-peak strength envelopes, the minimum principal stress increases to 17 MPa in the next time-step (for $\varepsilon^{residual}_p = 10^{-10}\%$). This σ_3 increase is a modeling artifact in FLAC and in reality this behavior is not expected from a brittle material under uniaxial compression. In FLAC, finite difference method is used and when an element fails in a brittle manner, a large un-balanced force is generated which must be dissipated. A temporary increase of σ_3 reflects the need to balance the force in the transit from a previous balanced state to the

next balanced state. Once the unbalanced force is sufficiently small, σ_3 becomes zero in all cases (Figure 3-3a).

Four sets of post-peak strength parameters are assigned to the model to verify the immediate artificial increase in the minimum principal stress at the post-peak stage (Figure 3-4b). For all four combinations of the post-peak cohesion and friction angle, an instantaneous artificial increase of the minimum principal stress (σ_3) is observed at the post-peak stress path for the sampling point P.1 in order to maintain the equilibrium (Figure 3-4a). For instance, only one time step is taken for the stress state at the peak strength where σ_3 = 0 MPa to reach the post-peak strength envelope at σ_3 = 18.9 MPa (defined by the post-peak cohesion and friction angle of 0.5 MPa and 50°, respectively). In the following time steps, the stress paths follow the post-peak strength envelope. When sufficient time steps are executed, the σ_1 stress reduces to the post-peak level and the transient artificial σ_3 diminishes completely.

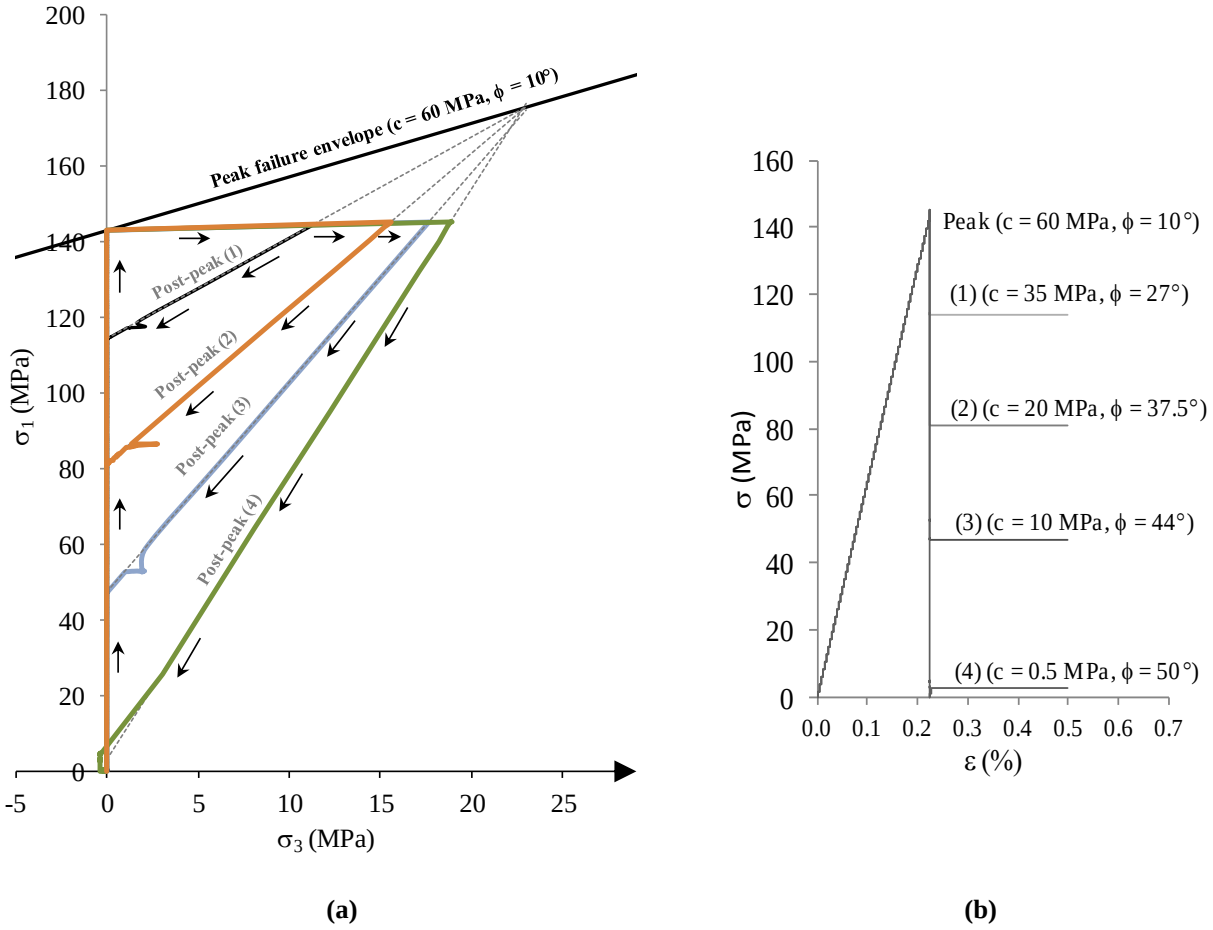

Figure 3-4: (a) Stress paths of a UCS specimen under uniaxial compression loading with four different post-peak strength parameters; (b) stress-strain curves.

This gradual or transient reduction of the maximum and minimum principal stresses after the peak strength is detectable only by using an explicit solution scheme such as FLAC, when a small time step is taken to compute stresses from strains in an element. The resulting plastic strain from one small time step can be smaller than the characteristic plastic strain assigned to the model. As discussed earlier, this small plastic strain will introduce interpolated strength parameters (cohesion and friction angle) to the model for calculating the corresponding post-

peak strength value. Hence, behaviors shown in Figure 3-3a and Figure 3-4a are obtained by employing a non-perfect brittle model.

In an implicit solution scheme such as PHASE^2 (Rockscience, 2008), a stress state is obtained for distinct loading stages and the transient stress change between the stages is not considered. Therefore, the transient stress path changes between loading stages cannot be captured by numerical tools using the implicit solution scheme. This issue was investigated by Cai (2008) focusing on the impact of stress paths on rock failure by implicit and explicit solution scheme.

3.4. Simulation of triaxial compression test

As discussed in the Section 2.3.3, the brittle behavior is observed at low or zero confining stress conditions in the post-peak deformation stage. In this section, further investigation of the influence of confinement on simulating the material behavior is conducted.

The influence of confining stress on rock strength is investigated by simulating a confined compression test. It is not possible to consider true triaxial loading using a 2D numerical tool such as FLAC. In the following discussion, instead of true triaxial loading, a biaxial loading is considered with a zero displacement in the out-of-plane direction.

In the confined compression test simulation, the same mesh used in the uniaxial compressive loading in Section 3.3 is used. The peak strength parameters are the same as the UCS simulation (Figure 3-4b) and the post-peak strength parameters are set as the third set of post-peak strength parameters in the UCS simulation (see Figure 3-4a and b). The characteristic plastic strain is equal to $10^{-10}\%$. An initial hydrostatic stress is applied and in the subsequent displacement

controlled loading is used to increase σ_1 while σ_3 is kept at the specified confining stress. The lower boundary is fixed in the vertical direction.

Two levels of confining stress, 5 MPa and 10 MPa, are considered. The models are axially loaded and the stress paths at P.1 (see Figure 3-2) are plotted in Figure 3-5a. σ_1 builds up in the model as the sample is further loaded from its initial hydrostatic stress state. Once the stress state reaches the peak strength envelope, a transient σ_3 build up can be seen as the stress state moves to the post-peak strength envelope. As illustrated in Figure 3-5a, the higher the confining stress is, the smaller is the minimum principal stress increment.

It has been discussed in the literature review chapter that the post-peak strength is a function of the confining stress. The differential stress–axial strain relationships for three different confining stresses are presented in Figure 3-5b. When there is no confinement, the post-peak differential stress is 47 MPa. When the confining stresses are 5 MPa and 10 MPa, the post-peak differential stresses are 69.8 and 92.6 MPa, respectively.

Not only does the post-peak strength of a rock increase with increasing confinement, the peak strength also increases with confinement depending on the slope of the peak strength envelope which is governed by the peak friction angle. In the results in Figure 3-5b, the change in the peak strength with increasing confinement is less than that of the post-peak strength because the peak and post-peak friction angles are 10° and 44°, respectively.

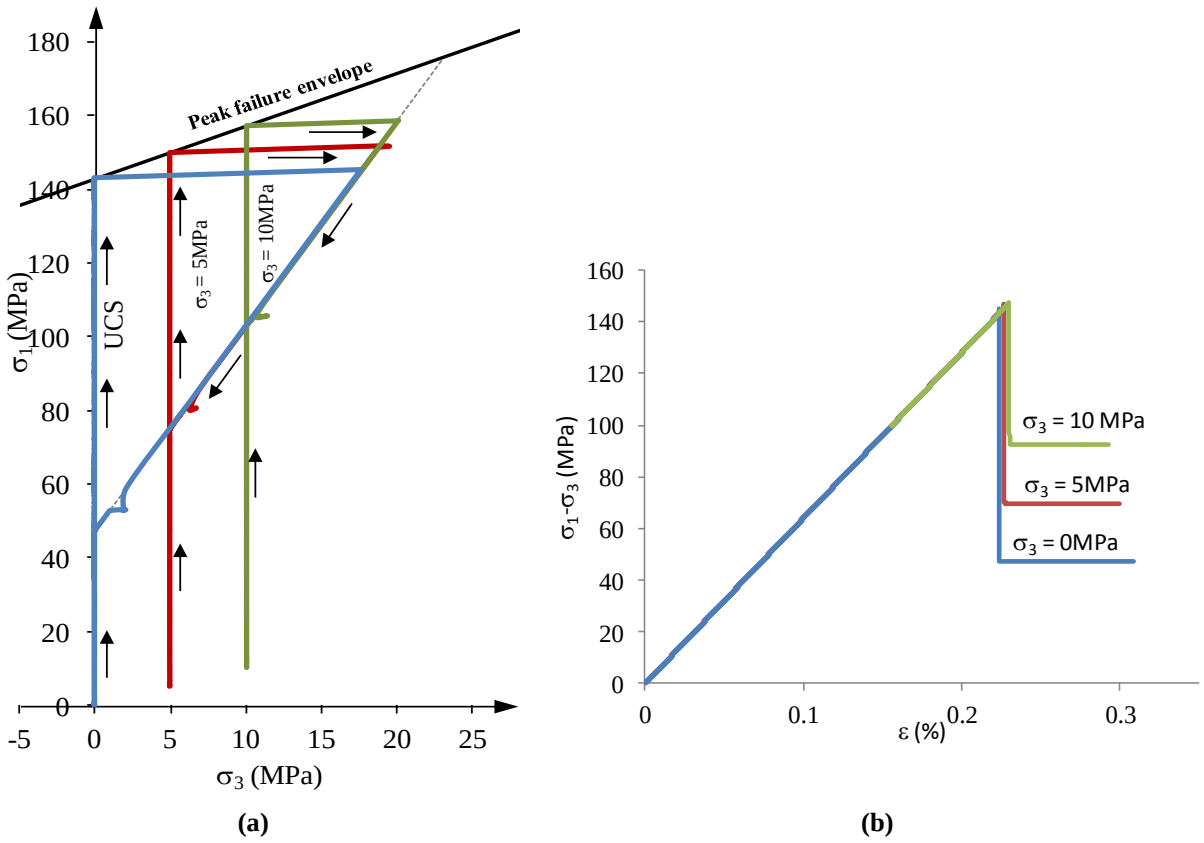

Figure 3-5: (a) Stress paths of a test specimen with three levels of confinements (0, 5, and 10 MPa); (b) the differential stress – axial strain curves corresponding to the three levels of confinement.

3.5. Concluding remarks

In this chapter, it was found that:

- The sudden reduction in the strength of a rock material at the post-peak stage can be simulated using FLAC. Different degrees of softening can be defined in the model using an input table in the strain-dependent failure model in FLAC.
- The simulated stress paths demonstrate a transient increase of confining stress in the process of reaching the post-peak stress state. This transient stress change is simply a modeling artifact and can be captured only by tools employing an explicit solution scheme. This

fictitious stress path change is more abrupt for rocks with brittle material behavior than those with strain-softening behavior.

- Depending on the slope of the peak strength envelope, which is governed by the peak friction angle, the peak strength increases with confinement and this correlation can be implemented within the models. Same relation can be also implemented for the confinement dependency of the post-peak strength and the slope of post-peak envelope.

Chapter 4

Modeling brittle rock failure around underground openings under static loading

4.1. Introduction

In the previous chapter, the perfectly brittle material behavior was simulated using FLAC and the effect of modeling strength parameters and confining stress on the rock deformation behavior was studied using a compression test model. This chapter discusses factors that influence the stress state and brittle failure around underground openings in numerical modeling.

The brittle failure process around an underground opening is often described as spalling or slabbing, and the resulting failed zone is commonly referred to as a "breakout" or "v-shaped notch". As discussed in Sections 2.2 and 2.4, field observation results indicate that brittle failure occurs in the region of maximum tangential stress around the boundary of an opening. This region is of critical importance to the stability of the opening, because in extreme cases such as rockburst, brittle rock failure can lead to complete closure of the opening. Because the behavior of a hard brittle rock is stress dependent, if the stress path at an element located in the region of high stress concentration could be simulated correctly, then the correct rock mass response may be captured.

Prior to modeling the plastic deformation of brittle rock at the periphery of an opening, it is important to consider the effect of the distance from the outside boundary of the model to the perimeter of the opening. The first section (Section 4.2) of this chapter addresses the influence of outside boundary condition on the stress state near the excavation boundary.

In Section 4.3, stress redistribution due to excavation is studied. The effect of the excavation simulation method is often ignored when modeling brittle failure around underground excavations. In this section, two main methods of simulating the excavation process (the core-

softening and the load-split methods) are discussed and the modeling results are compared. This section also includes the modeling to demonstrate the influence of mesh size near the boundary of the tunnel on the stress distribution. Course meshes may lead to under-estimating the stresses at the areas which are important for the initiation of the failure process.

Finally, Section 4.4 examines the influence of peak and post-peak strength parameters, as well as the dilation angle on rock failure around underground openings. A comparison of previous modeling approaches and the current approach is also made.

4.2. Influence of model size on simulation of rock failure

The stress state around the periphery of an opening needs to be determined correctly to analyze stress-induced failure. Accordingly, the governing equations, boundary conditions that include the model boundary condition and field stress condition, and stress and strain relation must be satisfied in the stress analysis.

One important concept in solving an excavation problem is the zone of influence of the excavation. Brady and Brown (2004) define the zone of influence as "a domain of significant disturbance of the pre-mining stress field by an excavation." This concept is widely used for problems that include the state of stress in a medium containing a number of excavations and interaction between excavations of different sizes. When an opening is located outside the zone of influence of other excavations (see Figure 4-1), it can then be designed by ignoring the presence of other openings.

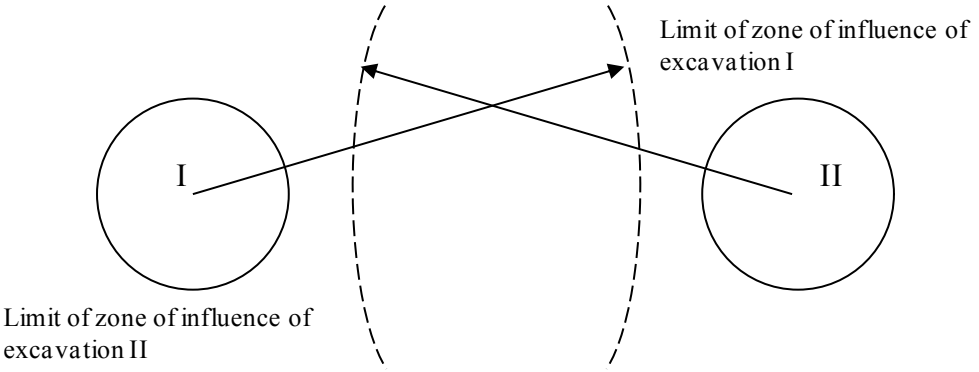

Figure 4-1: Same-size circular openings in a hydrostatic stress field, effectively isolated by virtue of their exclusion from each other's zone of influence (Brady & Brown, 2004).

The concept of zone of influence can be used to specify the correct size of outside boundary in numerical models. In other words, the outside boundary of the model should be large enough so that the influence of the outside boundary on the stress near the opening is sufficiently small. Two main approaches, the analytical approach using the Kirsch equations and the numerical approach, are used to investigate the effect of outside boundary on stress distribution around an excavation.

4.2.1. Analytical analysis of stress around a circular opening

In general, the zone of influence of an opening is a function of both excavation shape and pre-mining stresses. Analytically, this zone can be determined using the Kirsch equations. As illustrated in Figure 4-2, stresses around a circular excavation in an isotropic, linear elastic material can be determined analytically.

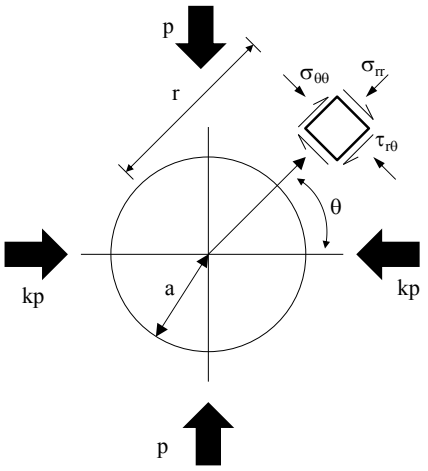

$$\sigma_{rr} = \frac{1}{2}p\left\{(1+k)\left(1-\frac{a^2}{r^2}\right)-(1-k)\left(1-4\frac{a^2}{r^2}+3\frac{a^2}{r^2}\right)\cos 2\theta\right\}$$

$$\sigma_{\theta\theta} = \frac{1}{2}p\left\{(1+k)\left(1+\frac{a^2}{r^2}\right)+(1-k)\left(1+3\frac{a^2}{r^2}\right)\cos 2\theta\right\}$$

$$\tau_{r\theta} = \frac{1}{2}p\left\{(1-k)\left(1+2\frac{a^2}{r^2}-3\frac{a^4}{r^4}\right)\sin 2\theta\right\}$$

Figure 4-2: Stresses and displacements induced around a circular excavation in plane strain (Hudson & Harrison, 2007).

One special case in which the Kirsch equations are simplified is the hydrostatic stress condition where $k = 1$, where k is the ratio of horizontal to vertical field stress components. In this case, the stress distribution around a circular tunnel with a radius equaling to "a" can be calculated using Eq. (8):

$$\begin{aligned}\sigma_{rr} &= p\left(1-\frac{a^2}{r^2}\right)\\ \sigma_{\theta\theta} &= p\left(1+\frac{a^2}{r^2}\right)\\ \tau_{r\theta} &= 0\end{aligned} \tag{8}$$

Using Eq. (8), it is calculated that for $r = 5\times(2a)$, $\sigma_{\theta\theta} = 1.01p$ and $\sigma_{rr} = 0.99p$; the stresses are not significantly different from the field stresses at this distance. This means that another excavation with the same diameter can be designed at a "$10a$" distance from the opening without significantly affecting the stress state around the initial opening. In summary, for a circular opening in an elastic medium in a hydrostatic stress field, the outer boundary must be set at 5

times the opening diameter to minimize the influence of the outside boundary on the stress conditions around the opening.

4.2.2. Numerical analysis of stress around a circular opening

In numerical modeling, it is also important to maintain a uniform far field stress on the outside boundary of the model. The inherent error associated with defining outside boundary in rock failure process simulation using numerical tools is not well documented in previous studies. In the following, the influence of a model outside boundary size on rock failure in a circular tunnel is studied.

In this section, first, an elastic analysis is conducted to study the influence of outside boundary on the stress state around the opening, followed by a plastic analysis that employs the spalling strength parameters with different model sizes. The in-situ stress field, Young's modulus and Poisson's ratio are the same as the values used in URL Mine-by tunnel case study, summarized in Chapter 2.

The outside boundary, which is also circular in shape, is set at different distances from the opening. The differential stress ($\sigma_1 - \sigma_3$) is recorded at ten stress points along a 4.4 m long line at the crown of the tunnel. The recorded stress values are plotted against the normalized distance from the opening (*r/D*) in Figure 4-3a, where *r* is the distance from the tunnel center to the stress point and *D* is the diameter of the tunnel. It is obvious that for stress points located more than one diameter away from the opening, the influence of the outside boundary on the stress magnitudes is small. The closer the stress points are to the surface of the opening, the more influence the outside boundary will have on the differential stress. For the stress point located on

the opening surface (r/D = 0), the tangential stress is only 130 MPa when the outside boundary is located 1.25 diameters away from the opening. As the outside boundary is set further away from the opening (e.g., 5 times of the opening diameter), the maximum tangential stress obtained is 160 MPa. For the given in-situ stress field, the maximum tangential stress is 169 MPa according to Kirsch's solution, which is for the case of a tunnel in an infinite elastic medium.

The results from the numerical analysis are compared with the analytical results from the Kirsch equations in Figure 4-3a. It is seen that for an outside boundary located at a distance of 5 times the opening diameter, the differential stress at the wall boundary where the notch eventually formed is very close to the analytical result.

The contours of the differential stress near the crown boundary are plotted in Figure 4-3b when the outside boundary is set at 1.5, 2.5 and 3.5 times the opening diameter. For simplicity, only two contours are shown; the black and red color lines stand for the boundaries for stresses in the range of 125 and 150 MPa, 150 and 175 MPa, respectively. It is observed that as the outer boundary size increases, the zone of maximum stress concentration expands. For the cases of outer boundary size of 1.5 and 2.5 tunnel diameters, the maximum differential stresses near the crown boundary are smaller than 150 MPa because no red contour lines appear. Only when the outer boundary is equal to 3.5 tunnel diameters, the maximum differential stress can be higher than 150 MPa (indicated by the red-color counter line).

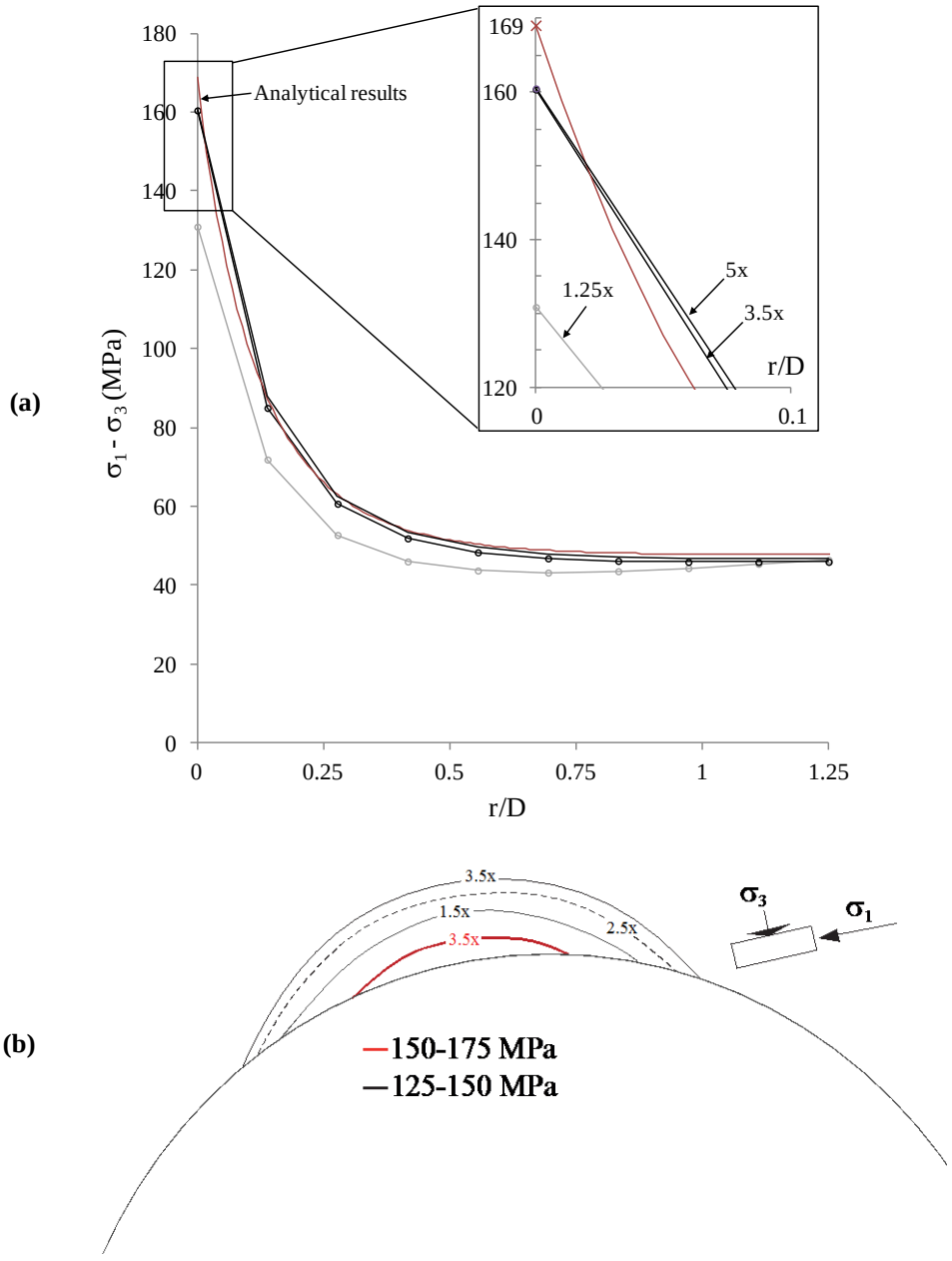

Figure 4-3: (a) Differential stress plotted against the normalized distance from the boundary of the tunnel; (b) The contours of the maximum tangential stress for different outside boundary sizes.

With a well-defined in-situ stress state, it might be thought that simulating the depth and the geometry of brittle failure near a tunnel located in a massive rock would be an easy task. However, as discussed in Section 2.4.1.2, there are many factors that influence the brittle rock

failure and a systematic parametric study is required to determine the proper modeling parameters which include both geometrical and mechanical ones.

The stress required to fail the Lac du Bonnet granite, obtained from laboratory uniaxial compressive strength tests, is 224 MPa under uniaxial loading. Assuming that the field strength is equal to the lab strength, in order to initiate failure around the surface of the opening, the tangential stress must reach the laboratory strength. However, in practice, due to the influence of many other factors on rock strength (e.g. scale effect, blasting damage and loading rate), the field rock strength is lower than the laboratory strength.

In this study, the Mine-by tunnel notch failure is reproduced using the strength parameters suggested by Diederichs (2007), which are presented in Figure 2-23 in Section 2.4.1.2.2. However, using the suggested strength parameters the final notch geometry predicted by Diederichs (2007) could only be reproduced if the outside boundary size is set to 1.25 times the tunnel diameter, as demonstrated in Figure 4-4 and Figure 4-5. It is demonstrated in Figure 4-3a and b that, by expanding the outside boundary of the model, the maximum differential stress increases. If the same strength parameters are used but the outside boundary is set 2, 3.5, and 5 times the tunnel diameter, the predicted failure zone would increase, which does not match well the notch shape observed in the field.

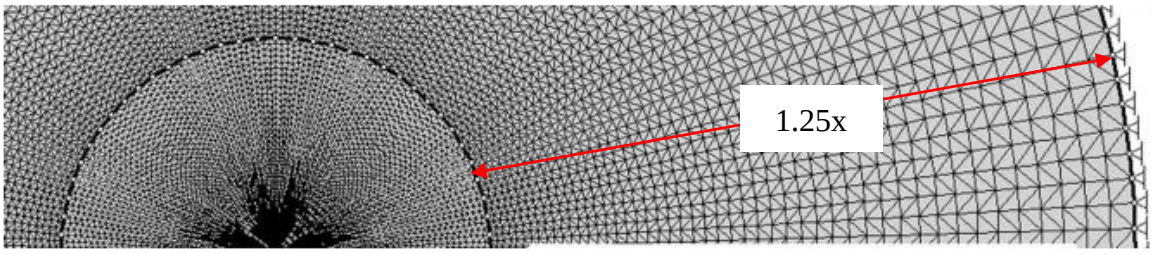

Figure 4-4: The outside boundary used in the spalling parameter approach (Diederichs, 2007).

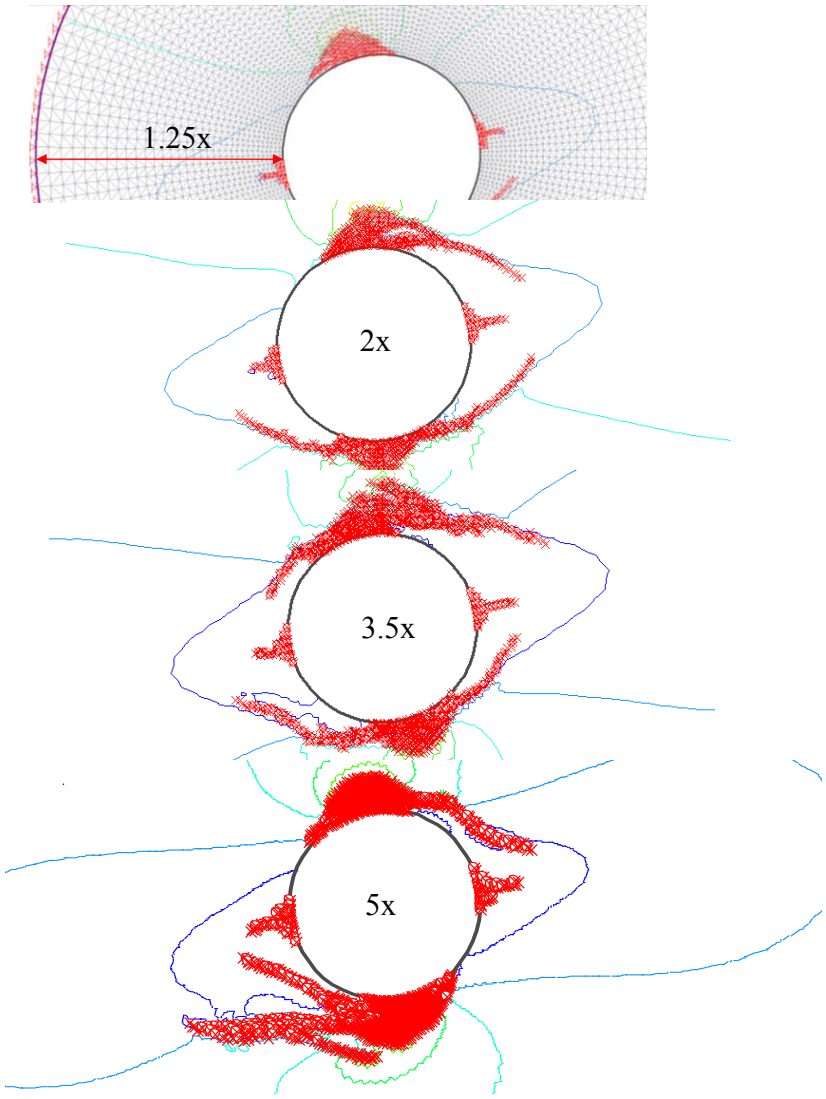

Figure 4-5: The predicted failure zone around the Mine-by tunnel with the outside boundary set at 1.25, 2, 3.5, and 5 times the tunnel diameter away from the opening.

It becomes clear in this study that there are many factors that can influence the strength parameters used in a numerical model. It was noted that the employed strength parameters can be influenced by the model boundary condition and the element mesh size near boundary of the tunnel. The maximum tangential stress at the tunnel wall could be underestimated when the outside boundary of the model is located too close to the opening or the meshes near the boundary of opening are too coarse. In such a case, the peak rock strength needs to be lowered to

allow failure to occur. Such back-calculated peak strength values should be used consistently with the modeling condition employed in the back analysis.

The outside boundary is always set to 5 times the opening diameter in this study to minimize the influence of outside boundary size on the modeling result. In some numerical software packages such as ABAQUS and PHASE^2, an infinite boundary option is available. However, compared with the results of using an infinite boundary the error in stress is small if the outside boundary is set to 5 times the opening diameter.

4.3. Influence of excavation method and mesh density on simulation of rock failure

Another important factor that affects the simulated stress state of the elements around the excavation boundary is the excavation method. Representation of the excavation technique in 2D numerical analysis is important when modeling brittle rock behavior around the underground openings. The goal here is to examine the stress path in a 2D plane-strain analysis using simplified techniques.

In the following sections, two methods for simulating the gradual 3D excavation process in 2D numerical modeling are investigated. The first method, which is called core-softening, simulates the case in which the notch formation initiates ahead of the excavation face (illustrated by dashed lines in Figure 4-6). In this method, the Young's modulus of the elements inside the tunnel area is degraded to zero in a number of stages to simulate the gradual excavation effect.

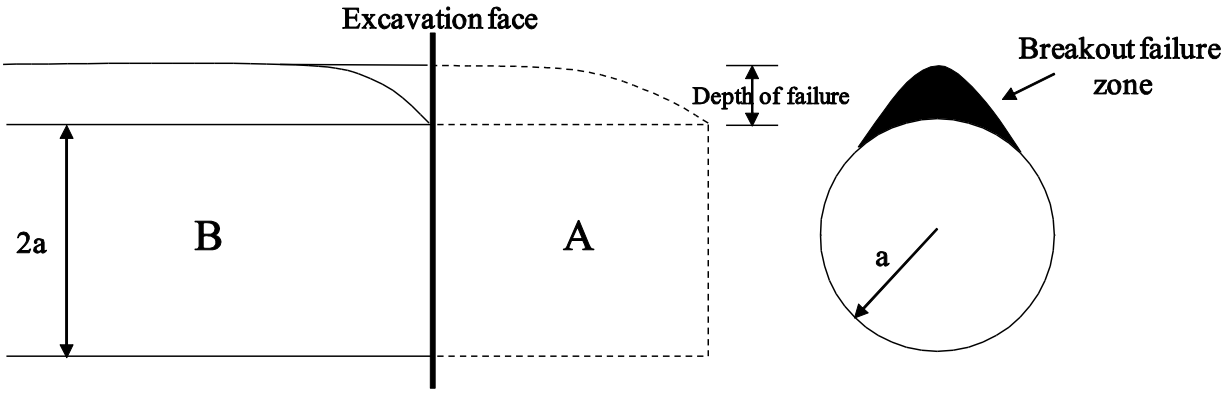

Figure 4-6: Longitudinal and cross section which illustrates the predicted breakout failure zones of a circular tunnel: (A) core-softening method; (B) load-split method.

The second method, which is called "load-split" method, is adopted from PHASE^2. As illustrated by the solid line in Figure 4-6, this method assumes that the notch formation starts behind the tunnel face. The tunnel core material is instantly removed at the first stage, and then the portions of the in-situ stresses are applied as a boundary condition and gradually increased in stages until reaching the in-situ stress state.

4.3.1. Core-softening

Using either tunnel core material softening or the gradual reduction of the equivalent forces within the tunnel, progressive tunnel excavation can be simulated (Cai, 2008). The approach of gradual reduction of the equivalent forces is also called the internal pressure reduction method. In the internal pressure reduction approach, the tunnel excavation process is simulated by gradual removal of the equivalent internal forces applied on the boundary of the opening; a fish function referred to as "relax_tractions.fis" is available in the FLAC library for this purpose. The end result by the internal pressure reduction method is similar to that of the core material softening method. In the present study, however, the core-softening approach is used.

The tunnel core material is considered as an elastic continuum and the Young's modulus and the Poisson's ratio are equal to 60 GPa and 0.25, respectively. The stiffness (Young's modulus) of the tunnel core material is reduced from 60 to 0 GPa linearly in ten stages. At the last stage, the core is defined as a null model in FLAC (or is excavated in PHASE^2). At each stage, 5000 cycling steps are taken for the model to reach equilibrium.

The stress paths at the crown boundary element, obtained from FLAC, are compared with that obtained by PHASE^2 in Figure 4-7a. The variation of the stress path in FLAC reflects the fact that at each stage of core-softening, the stresses at the monitoring point are adjusted with a quick decrease of σ_3 initially followed by a gradual increase of both σ_1 and σ_3. The stress paths given by the PHASE^2 model are straight lines (black color). At the last stage of core-softening, the minimum principal stress (σ_3) at the crown boundary element of the excavated tunnel, which is expected to be zero or having a negligible value, is in fact dependent on mesh size. Two types of elements, triangular and quadrahedral, are used in the PHASE^2 models. In general, the mesh sizes in the PHASE^2 models are smaller than that in the FLAC model, and the final stress state by the PHASE^2 models are closer to the analytical solution than that of the FLAC model. It can be observed that use of a quadrahedral element produce the most realistic stress state at the boundary of opening ($\sigma_3 \cong 0$). In general in FEM or FDM modeling, the finer the mesh is, the better the results are. However, the choice of mesh size must also consider the constraint of computing time.

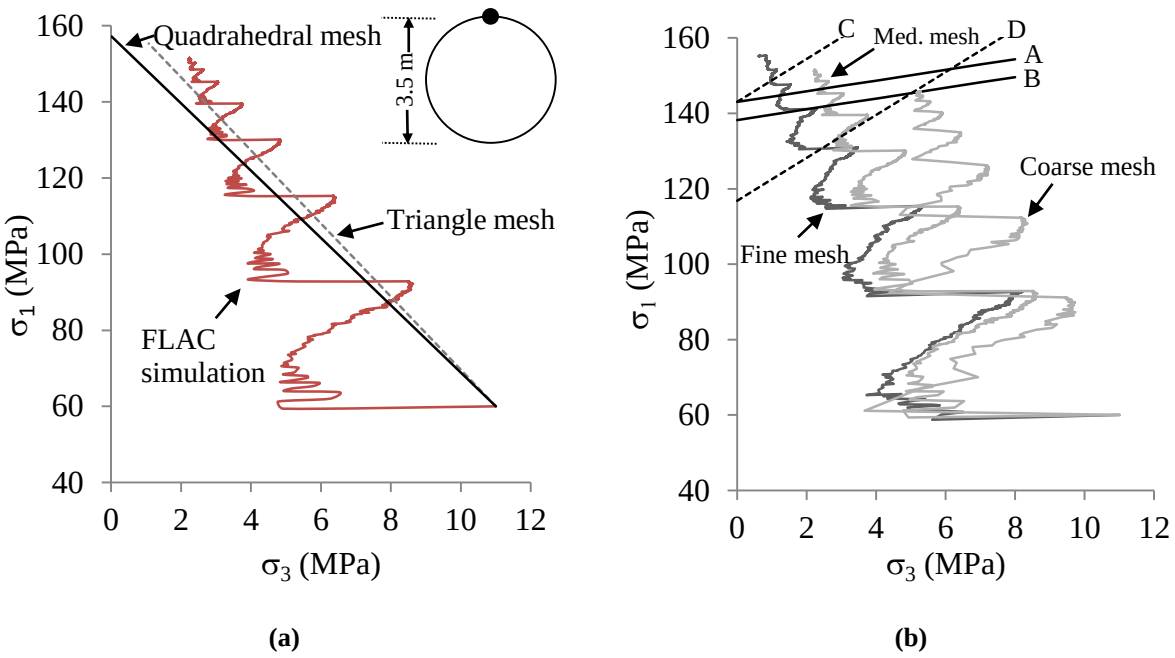

Figure 4-7: (a) Comparison of elastic stress path obtained from PHASE^2 (black) and FLAC (brown); (b) FLAC elastic stress path for three mesh sizes at a point on the tunnel crown boundary. A, B, C and D are different peak strength envelopes.

Stress paths for three mesh sizes are plotted in Figure 4-7b to further illustrate the mesh size influence on the modeling result in FLAC. The ratio of the element size at the tunnel boundary to the diameter of the tunnel, a/b (see Figure 4-8) are 0.01, 0.02, and 0.06 in the fine, medium, and coarse models, respectively. It is seen that the mesh size can have a large influence on the stress state and partially the failure zone near the excavation wall. If failure envelope A (defined by c = 60 MPa, ϕ = 10°) is used to define the peak rock strength, the coarse model will behave elastically because the stress state is below the failure envelope. On the other hand, the fine and the medium mesh models will have elements entering the plastic deformation stage.

Failure envelope B, which is defined by c = 58 MPa and ϕ = 10°, lowers the UCS from 143 to 138 MPa. If this failure envelope is used, then, some elements in the coarse mesh will deform

plastically. Failure envelope C, which has the same UCS of 143 MPa, is defined by a higher friction angle of 44.5°. Only the fine mesh model will have elements entering the plastic deformation stage if the failure envelope C is used. On the other hand, if a set of strength parameters is used to define failure envelope D, all three models will have failed elements. It becomes clear that mesh size can affect the strength parameters in plastic modeling results. If a coarse mesh is used, then low rock strength may have to be employed in order to initiate failure at the tunnel wall and match the zone of yielded elements to the field observations. In other words, the peak strength parameters are associated with the mesh size used in the numerical models.

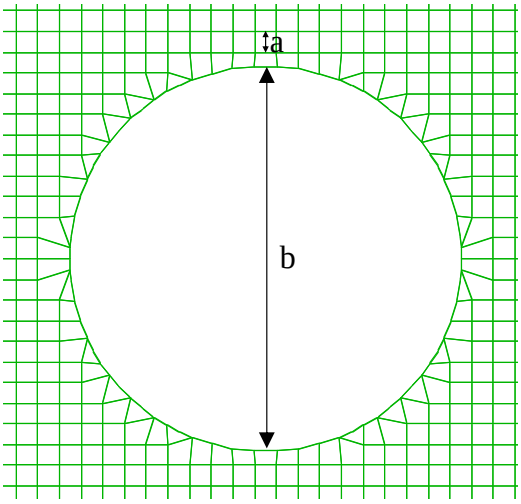

Figure 4-8: The a/b ratio of the mesh size in vicinity of the excavation boundary to the diameter of the opening.

4.3.2. Load-split

As mentioned above, the load-split method applies portions of the in-situ stresses in multiple stages until the in-situ stress state is reached. This technique is readily available in PHASE^2. In FLAC, a fish routine was developed to realize this technique. Initially, a fully excavated circular

opening is generated and load-split loading is applied in 10 stages. At each stage, 10% of the final in-situ stress is applied to the model boundaries and 5,000 steps are taken before the model reaches a balanced state. At the last stage, the stresses applied to the boundary of the model are equal to the in-situ stresses. The fine mesh model (a/b = 0.01) is employed in both the load-split and the core-softening simulations to maintain the consistency of the result.

The stress path at the crown boundary by the load-split method is plotted in Figure 4-9 in red color. For an elastic material, the final stress states at the point from both the load-split and core-softening methods are identical. However, a large difference exists between the two stress paths and this is discussed in the next section.

4.3.3. Comparison of the stress paths from the two excavation simulation methods

Based on the results presented in Sections 4.3.1 and 4.3.2, it becomes clear that the stress state of an element on the tunnel boundary follows different paths depending on the excavation method used. The stress path obtained from the core-softening method starts from the in-situ stress state and then develops until it reaches the final stress state. On the other hand, the stress path obtained from the load-split method starts from a zero stress state and then develops until it reaches the final stress state. In an elastic analysis, if all model parameters and model dimensions are the same in the two simulations, the final stress states of the two excavation methods are identical. However, the stress states between the start and the final states from the two excavation methods are very different. This difference may be of relevance in plastic analysis because failure initiation depends on the intermediate stress states as well.

The correct stress path at a point around the advancing tunnel can be captured only by a 3D stress analysis. The 3D stress path expressed by the σ_1 and σ_3 (maximum and minimum field stresses, respectively), which was obtained from Examin3D by Read and Martin (1996), is plotted in Figure 4-9 along with the stress paths by the core-softening and the load-split methods. At the Mine-by tunnel, the failure zone initiates one diameter away from (between D and E in Figure 4-9) the tunnel face. This suggests that, when modeling progressive brittle rock failure as the tunnel advances, the stress path by the load-split method is very close to that by the 3D stress path. Under such a stress path, the confinement σ_3 is very small at the wall element and the failure process is driven by a steady increase of σ_1.

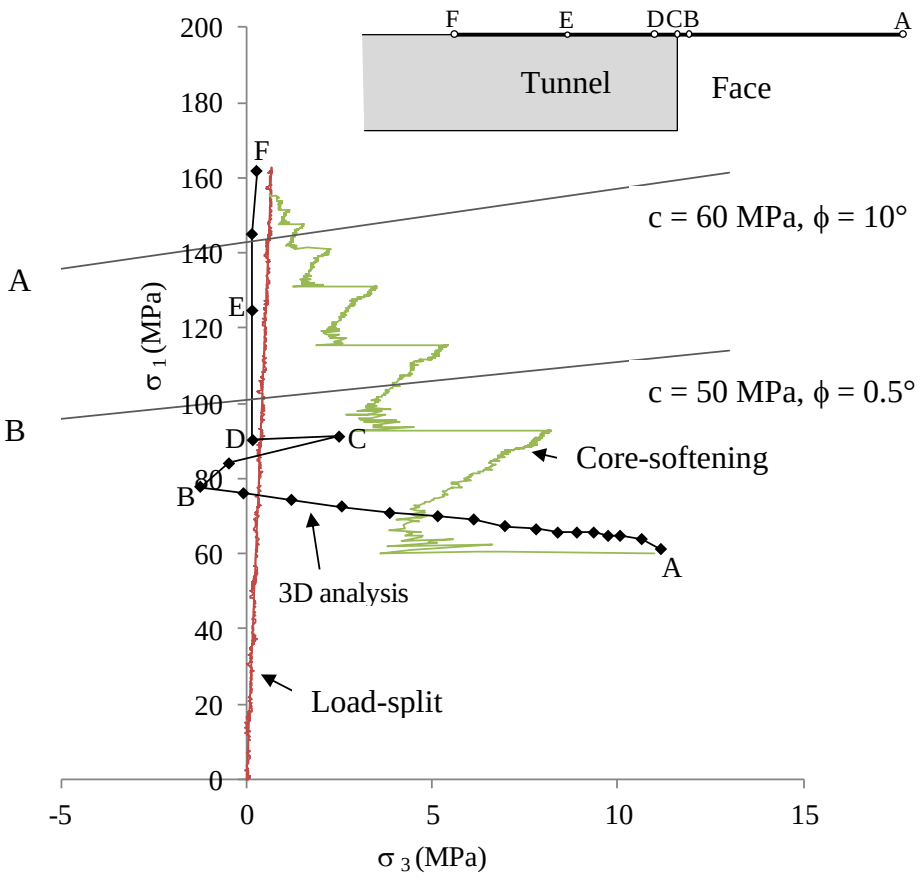

Figure 4-9: The stress paths obtained from the core-softening and load-split methods are compared with the 3D stress path obtained from Examin3D (after Read and Martin (1996)).

It is seen that stress paths from the two excavation methods converge at low confinement. When failure envelope A (defined by c = 60 MPa and ϕ = 10°) is used, the difference in modeling results by the two excavation methods would be small. On the other hand, if failure envelope B (defined by c = 50 MPa and ϕ = 0.5°) is used, the simulation results by the two excavation methods would be large (Figure 4-9).

The above reasoning is based on the elastic stress analysis results. A plastic analysis was conducted to demonstrate the influence of excavation simulation method on the brittle failure

zone. Two apparent peak failure envelopes (A and B as illustrated in Figure 4-9) were assigned to the model. The post-peak failure envelopes are identical in both cases and the assigned strength parameters are shown in Figure 4-10a and b. A constant 40° dilation angle and a tension cut-off of 18 MPa are assigned in all models. The stress paths of the element on the crown boundary element are plotted in Figure 4-10a and b.

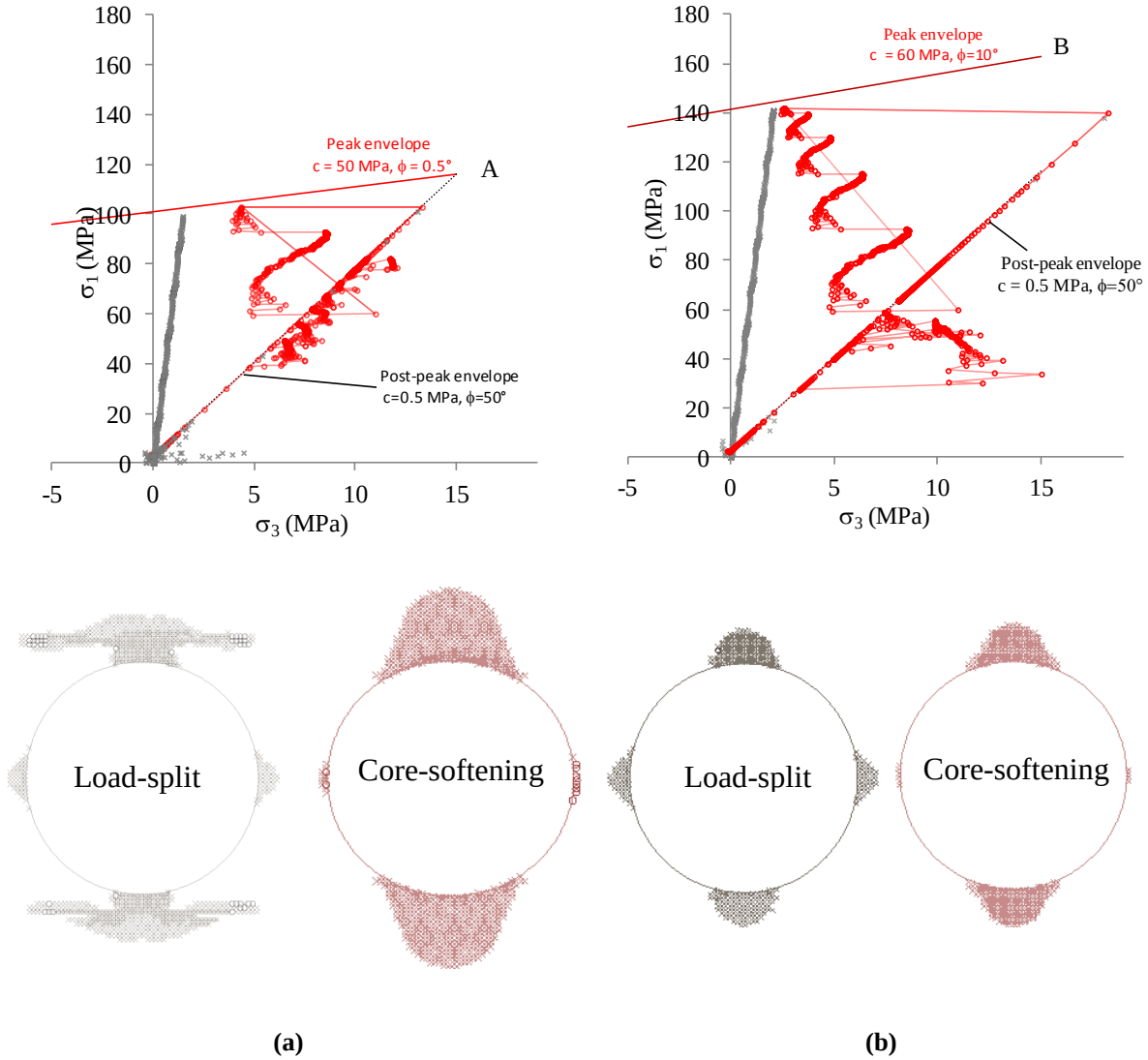

(a) **(b)**

Figure 4-10: The stress paths of the crown boundary element and predicted damage zones by the load-split and core-softening methods, (a) peak failure envelope A; (b) peak failure envelope B.

Figure 4-10a illustrates that there is a large difference in the simulated failure zones obtained from two excavation methods when a lower peak strength envelope is used. The stress paths from the two methods reach the peak envelope at different σ_3 stress states. At the point when the stress path reaches the peak strength envelope, the confining stress in the core-softening method is higher than that in the load-split method. On the other hand, Figure 4-10b suggests that by selecting a higher apparent peak envelope, the state of stress at which the stress path reaches the failure envelope is very close for both the load-split and core-softening methods. As a result, the simulated failure zones around the tunnel are somewhat similar, regardless of the excavation simulation methods used. This is because that failure initiates from the tunnel wall where the confining stress is very small. Any subsequent rock failure is also occurring in the zones where the confining stresses are small. Hence, the two stress paths, generated by two different excavation simulation methods, will produce comparable results (see Figure 4-10b).

4.4. Influence of strength parameter on simulation of rock failure

From the 3D stress path analysis as illustrated in Figure 4-9, it is observed that the tangential stress on the crown boundary increases monotonically when the excavation face passes point D. The stress paths obtained from the two different excavation methods suggests that beyond point D, the 3D stress path can be better represented by the load-split method in a 2D numerical model. Despite of this observation, it is seen that when the peak strength is high enough, both methods predict the failure zone adequately. Therefore, in this section only the modulus reduction (core-softening) method is utilized to simulate the excavation response. A parametric study is conducted to study the influence of strength parameters on the simulated state of stress

and consequently the brittle failure in the perimeter of the opening. The results and trends are only valid if the modulus reduction method is utilized to simulate the excavation response.

4.4.1. Peak cohesion and friction angle

The peak strength is the maximum stress that a rock can sustain at a given stress state. As discussed in Section 2.3, the peak strength of a rock sample is normally obtained from compression tests at different confinements. When the test data are represented by a linear relationship, strength parameters (c and ϕ) of the Mohr-Coulomb failure criterion can be obtained from Eq. (2).

Edelbro (2010) found that the peak friction angle influences the simulated zone of yielded elements, significantly. The influence of apparent peak strength on the stress path and potential rock failure has been investigated in Section 4.3.1 using meshes of different sizes. The peak friction angle for the plastic strain-dependent CWFS model varies between 0° and 22° (e.g. Hajiabdolmajid et al. (2002); Corthesy and Leite (2008)). The choice of this value is based on distribution of the yielded element. For a brittle material, a very small peak friction angle in combination with a constant peak cohesion of 60 MPa will result in a wider and deeper failure zone. In general, an increase in peak friction angle while keeping cohesion constant results in a higher rock strength. In low confinement zones, as is the case for rocks at the boundary of a tunnel, by keeping the post-peak failure envelope with parameters indicated in Table 4-1, it was found that an apparent peak friction angle of 10° simulated the depth of notch breakout well when the brittle Mohr-Coulomb model was used (Figure 4-11a). Increasing the apparent peak friction angle beyond 20° with a cohesion of 60 MPa will result in a UCS value higher than the

maximum deviatoric stress given by $3\sigma_1 - \sigma_3 = 169\,\text{MPa}$ for a circular opening with smooth surface. Therefore, no failure can be initiated on the boundary of the tunnel.

Table 4-1: Strength parameters for the strain-dependent CWFS model and the brittle Mohr-Coulomb model

		Peak	Post-peak	ε^s_p
Friction angle (φ)	Brittle	10	50	0.01%
	Strain-softening	0	48	0.50%
Cohesion (MPa)	Brittle	60	0.5	0.01%
	Strain-softening	50	15	0.20%

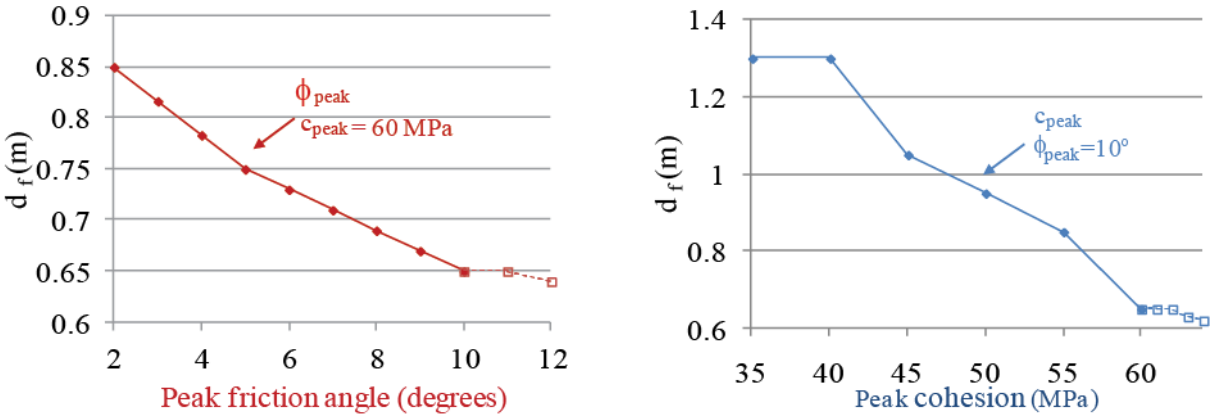

(a) **(b)**

Figure 4-11: Influence of (a) peak friction angle and (b) peak cohesion on depth of failure (d_f).

The apparent peak friction angle is fixed at 10° and the post-peak strength parameters indicated in Table 4-1 are used to study the influence of apparent peak cohesion on depth of failure. It is seen from Figure 4-11b that cohesion has a large influence on the depth of failure. For the elastic-perfectly brittle-plastic model, an apparent peak cohesion of 60 MPa simulates the failure zone that best represents the Mine-by tunnel notch shape in-situ. The apparent peak UCS for the

elastic-brittle model is 143 MPa. These peak strength parameters are obtained through a back analysis by adjusting each parameter and checking the yielded element distribution against the notch shape of the Mine-by tunnel. Hence, these parameters, just like parameters from other modeling excises, are not proven real and should be used in models with similar modeling condition.

From the two plots in Figure 4-11, it becomes clear that with the parameters selected, variation of the cohesion parameter influences the depth of failure more than that of the friction angle. This again is attributed to the fact that failure initiates at the periphery of the tunnel where confinement is low so that a change in cohesion will have more impact on the failure zone than a change in the friction angle (see Figure 4-7b).

4.4.2. Post-peak cohesion and friction angle

As the stress increases, a rock will eventually reach its peak strength and then enter the post-peak region. As demonstrated in Section 2.3, an important feature of the post-peak ultimate strength envelope, obtained from test results of rock samples (which were not strained enough to reach their residual state), is that the post-peak cohesive strength is very low (near zero) and the friction angle reduces with increase of confinement. Because the frictional strength is a function of normal stress (σ_n), this component does not contribute to the overall post-peak strength of the rock at low confining stresses (σ_3). Therefore a very low load-bearing capacity is expected from the failed rock at the post-peak stage if the rock is not well confined.

Figure 4-12 demonstrates the influence of post-peak cohesion and friction angle on the depth of failure by the brittle Mohr-Coulomb model. Post-peak friction or cohesion is varied while keeping the peak failure envelope constant with the parameters defined in Table 4-1.

As the post-peak cohesion or friction angle increases, the depth of failure decreases significantly. This observation is somewhat contradictory to the conclusion by Edelbro (2010), who stated that post-peak cohesion has less impact on the depth of failure than the peak cohesion.

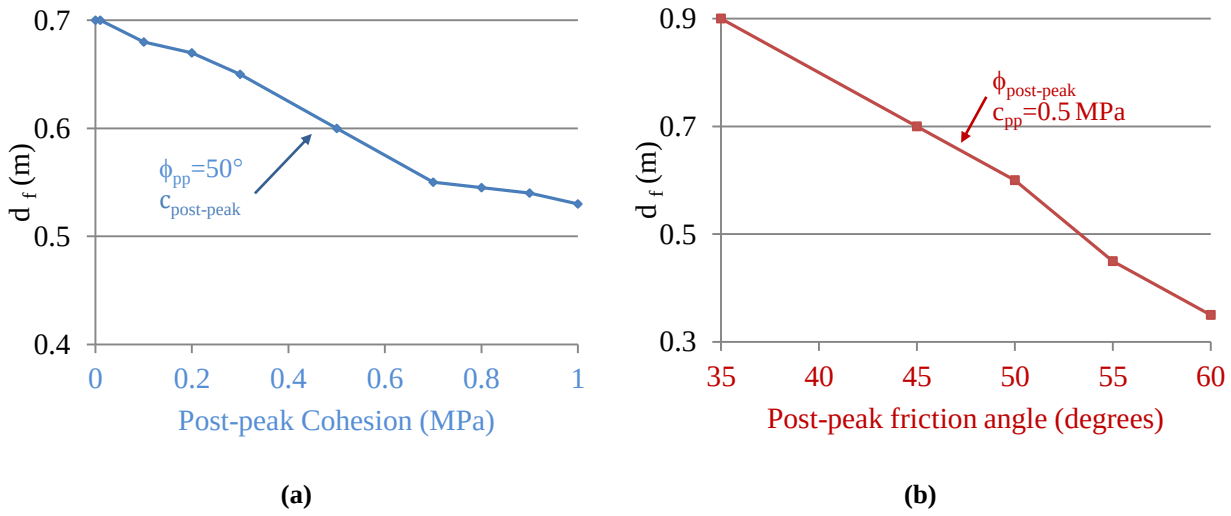

Figure 4-12: Influence of post-peak cohesion (a) and friction angle (b) on depth of failure.

Because no triaxial test data with well-defined post-peak strength on Lac du Bonnet granite are available, results from rocks with similar brittleness were used to determine the post-peak ultimate friction angle in the numerical simulation (Section 2.3). These parameters may only be valid under low confinements, where the saw-tooth asperities of factures are not worn out (Patton, 1966). At higher confinements and when more shear-strain is accumulated, a lower value for the ultimate friction angle is more approximate. Based on this observation, the post-peak cohesion and friction angle (as shown in Table 4-1) that best simulate the Mine-by tunnel

notch breakout are 0.5 MPa and 50°, respectively. The resulting post-peak uniaxial compression strength of the rock is 2.75 MPa.

By selecting high values for apparent post-peak strength parameters (e.g., c_{pp} = 15 MPa, ϕ_{pp} = 50°), while incorporating a perfectly brittle material in FLAC, the progressive formation of the failure zone as the stresses at the boundary of opening redistribute is presented in Figure 4-13. The tunnel core material is softened in ten stages from "a" to "final"; the stress path at the crown boundary element (point A) shows that the element yields in the stage transition from "a" to "b" because the peak strength is reached. At the end of stage "b", the stress state at point A is in fact sitting above the "peak strength envelope". This is only possible because the defined post-peak strength envelope is above the peak strength envelope for σ_3 greater than about 2.3 MPa.

In other words, there is strain-hardening in the high confinement zone by the prescribed peak and post-peak strength envelopes. This issue has been previously discussed in Section 2.3.4 when the slope of the post-peak strength envelope is higher than that of the peak one in the linear Mohr-Coulomb failure model. As excavation continues, the stress path reaches the post-peak strength in stage "d" and then follows the strength envelope from then until the final stress state is reached.

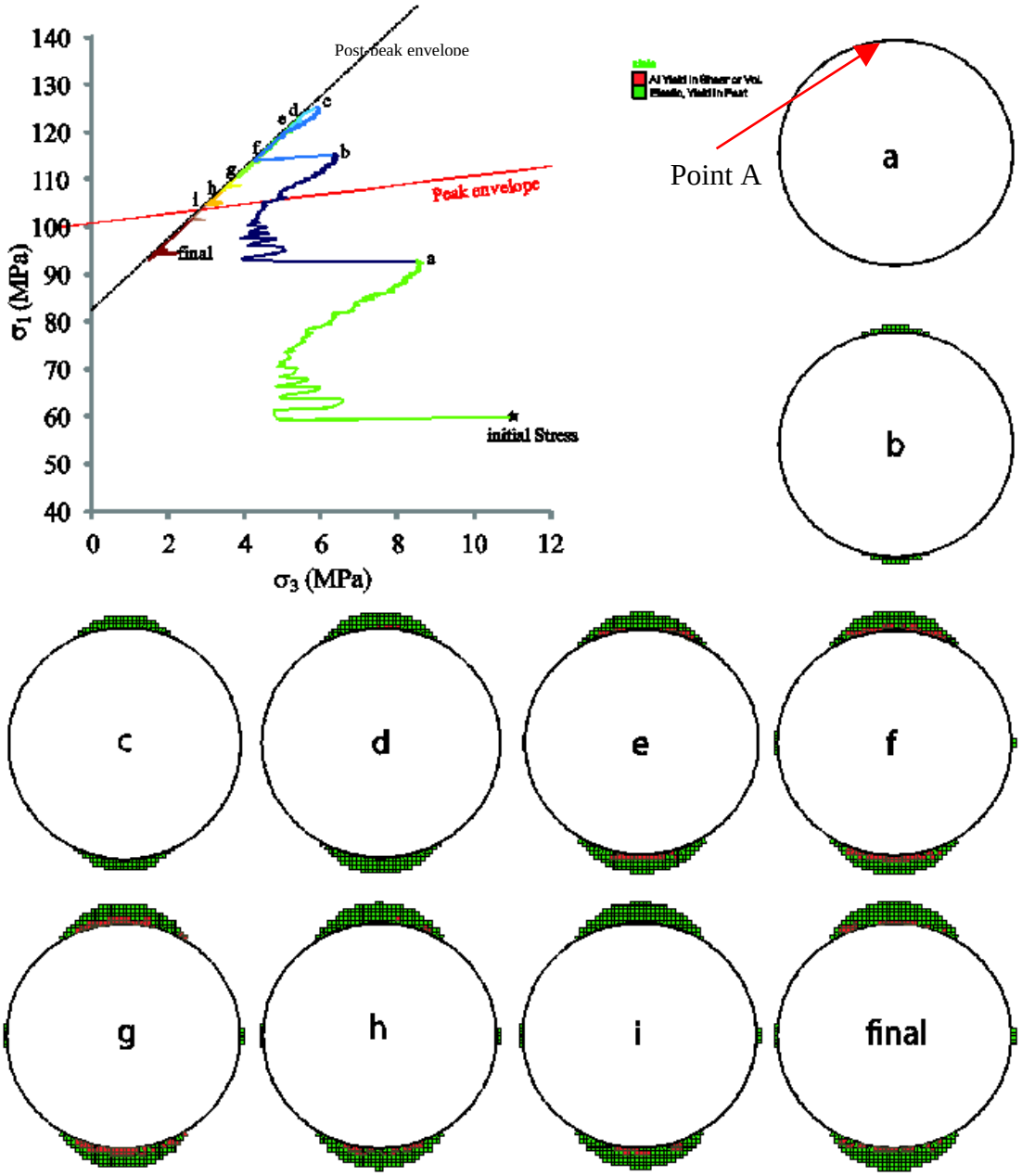

Figure 4-13: Simulation results using the perfectly brittle material behavior and assigning the CWFS model apparent strength parameters, showing the stress path and the failure zone corresponding to each stage.

The problem might be partially resolved by assigning a substantially lower post-peak cohesion while keeping the apparent friction angle unchanged (c_{pp} = 3 MPa, ϕ_{pp} = 50°). In this case, the

intersecting point of the peak and post-peak strength envelopes will be at a higher confinement level. If proper excavation method is used in the modeling, the stress path will mostly move to the low confinement zone, thus ensuring that the post-peak strength is lower than the peak strength. This combination of strength parameters results in a post-peak UCS value of 16.5 MPa. These post-peak parameters are assigned to the brittle model, while keeping the peak strength parameters the same as the previous model. The resulting loading path of the advancing tunnel at the crown boundary element is presented in Figure 4-14b and the final failure zones are presented in Figure 4-14c. The first yielded element occurs at stage “b” during core-softening when the stress point reaches the peak failure envelope. After that, the strength parameters change to their post-peak values and the stress path follows the post-peak strength envelope. The confining stress reduces as the core material softens until the stress point reaches the final state.

At the final stage when the tunnel is fully excavated, maximum stresses in the boundary elements on the roof of the tunnel where the notch is formed are small (0-20MPa) (Figure 4-14). Even though the yielded elements resemble the notches of the Mine-by tunnel well, the remaining stresses in the notch zone are not zero, which is a limitation of the continuum modeling approach employing a failure model with peak and post-peak strength envelopes.

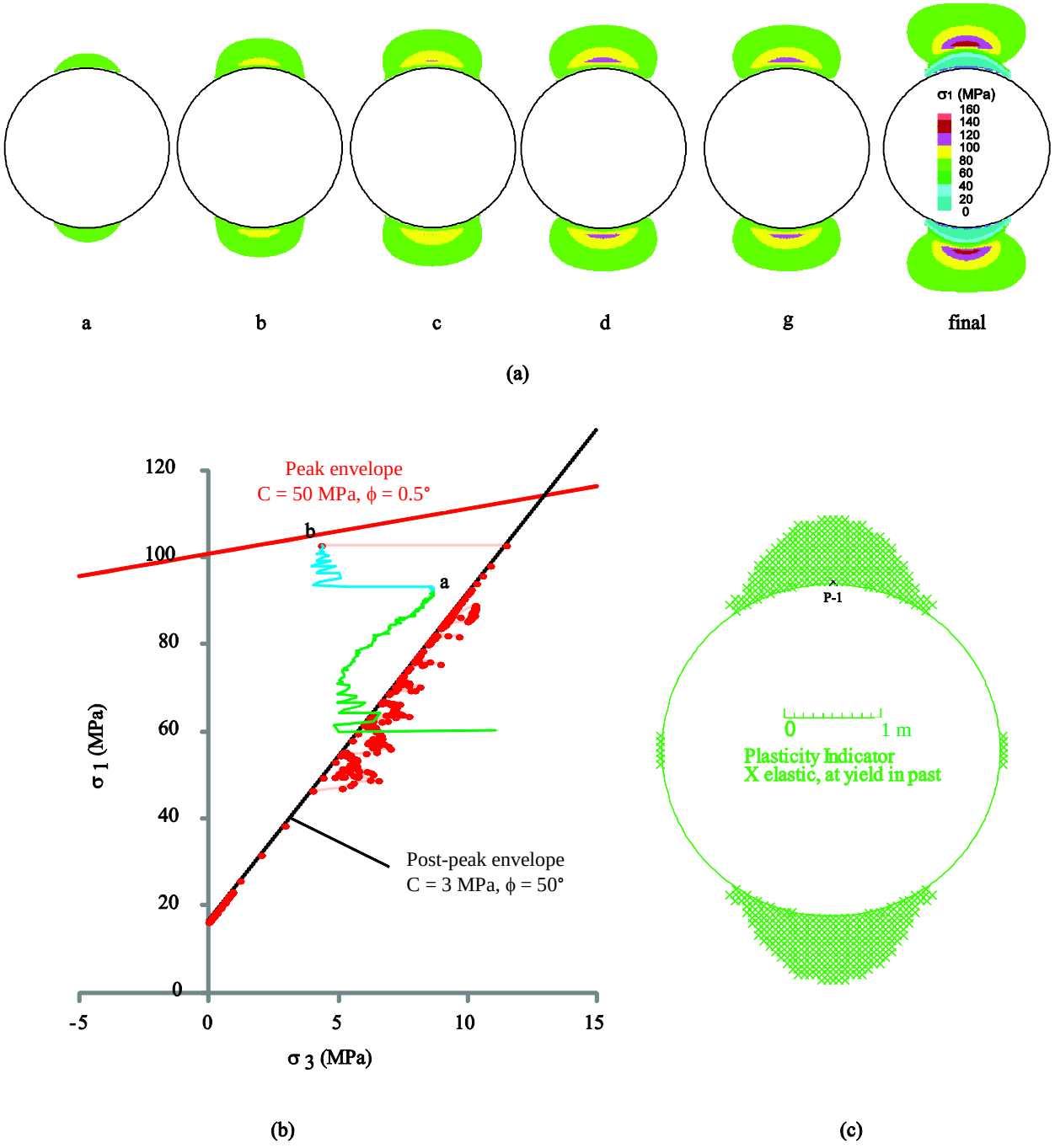

Figure 4-14: Simulation results of assigning a low post-peak strength in the brittle model; (a) the state of maximum principal stress in tunnel perimeter; (b) the stress path of crown boundary element during the core-softening; (c) the simulated failure zone and the location of the stress history point on the crown boundary.

Finally by using the peak and post-peak strength parameters that were previously prescribed in Figure 4-10b, and incorporating either the core modulus reduction or the load-split method for the simulation of the excavation method, the failure zone at the compression zone at the crown can be modeled successfully. Figure 4-15 illustrates the formation of the yielded elements starting from the fifth stage of the core modulus reduction, when the Young's modulus of the tunnel core material is reduced by 40%. By choosing a low post-peak strength at low confinement, defined by c_{pp} = 0.5 MPa, ϕ_{pp} = 60°, the notch failure zone can be captured and stresses in the yielded elements were between 0 and 50 MPa (Figure 4-15-final).

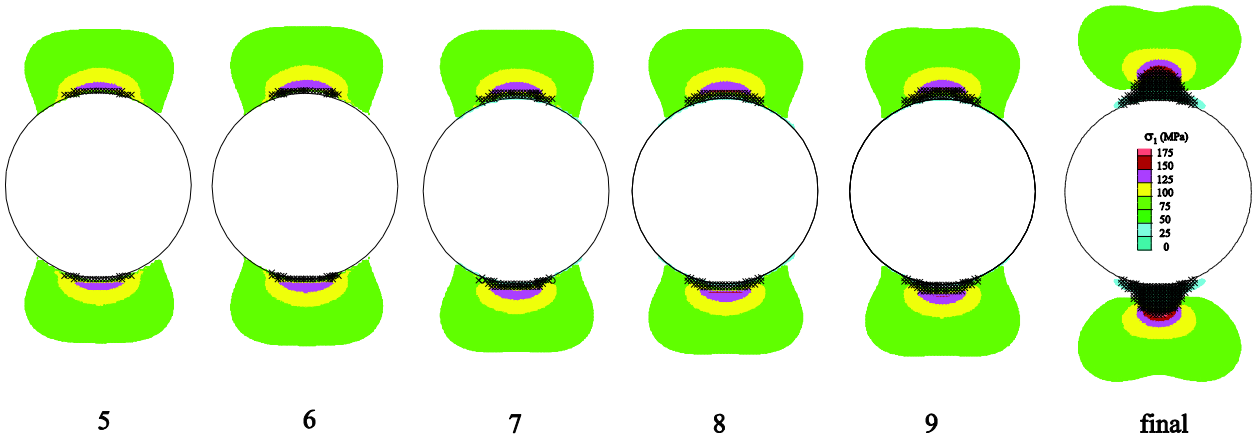

Figure 4-15: Maximum principal stress state and simulation results by assigning a low post-peak strength at low confinement in the brittle model (black crosses define all the yielded elements).

4.4.3. Influence of dilation angle on simulation of rock failure

Dilation angle is a measure of the volume increase in a material during shearing. In continuum mechanics modeling, the dilation angle for rocks is small and it should be less than the friction angle according to the plasticity theory (Vermeer & De Borst, 1984; Zhao & Cai, 2010). A higher dilation angle leads to higher deformation. Using the brittle Mohr-Coulomb parameters with zero dilation will not result in V-shaped failure around the opening (Figure 4-16). The effect

of rock dilation needs to be considered to approximate the notch breakout correctly. The results presented in Figure 4-16 are obtained using the brittle Mohr-Coulomb parameters shown in Table 4-1 with varying dilation angles and a tensile strength of 18 MPa. It can be noted that when the dilation angles are small, failure zones tend to propagate horizontally. When the dilation angle is greater than 20° (lower than 50°), V-shaped breakouts can be captured reasonably.

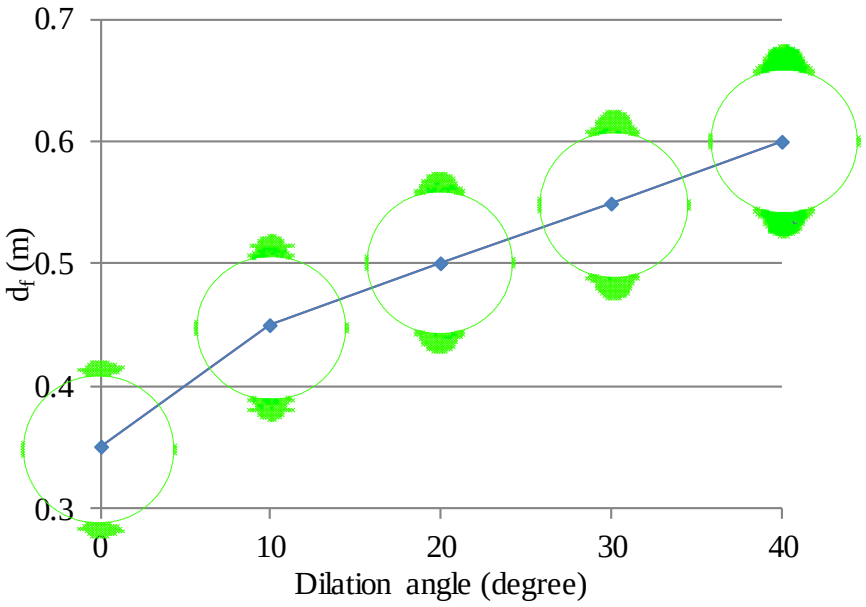

Figure 4-16: Influence of dilation angle on brittle rock failure.

4.5. Concluding remarks

The brittle Mohr-Coulomb model is used in an attempt to simulate the depth of failure around the Mine-by tunnel. For the given rock mass properties and boundary conditions, different excavation simulation methods lead to different stress paths, which can influence the failure

zones around the excavation boundaries. In numerical modeling, the behaviors of a rock mass can only be reasonably simulated when the stress path is captured correctly.

3D stress analysis is needed to capture correct stress redistribution near the advancing face of the tunnel. Stress states at a location far away from the tunnel face can be simulated by 2D plane strain analysis. 3D numerical stress analysis can be time-consuming and requires a large processing speed and memory. Two techniques, i.e., core material softening and load-split, are used to simulate gradual rock failure in 2D due to stress change. The influence of excavation methods on rock failure is studied considering the strength envelope. It is noted that if the rock strength is high, failure can only occur when the tangential stress is sufficiently high and the confinement is low. In this case, the excavation method has little influence on the failure zone. On the other hand, if the rock strength is low, the difference in the two excavation methods is large.

It became clear in this study that there are many factors that can influence the strength parameters used in a numerical model. It was suggested that the employed strength parameters can be influenced by the model boundary condition as well as the mesh size of elements near boundary of the tunnel. The maximum tangential stress at the tunnel wall could be underestimated when the outside boundary of the model is located too close to the opening or the mesh near the boundary of opening is too coarse.

Rock failure is always initiated near an excavation boundary where the confinement is small or zero. By utilizing the peak strength parameters suggested by the brittle Mohr-Coulomb model, the Mine-by tunnel notch failure can be captured regardless of the method utilized to simulate the excavation process.

It can be misleading to examine the yielded element zones for failure zones around an excavation without mentioning the post-peak stress state in the failure zone. An important element in the brittle Mohr-Coulomb model is its post-peak strength envelope. The apparent post-peak strength is defined by a very small post-peak cohesion and a friction angle which reflect the frictional strength of fractured rocks under low confinements. In this situation, the remaining post-peak stresses in the failure zone are low.

When back analyzing the observed rock failure in the field, it is required to make a combination of choosing one set of parameters to define the peak strength envelope and another set of parameters to define the post-peak strength envelope. When a low post-peak strength envelope is selected, it will require a high peak strength envelope in the model. Hence, it is important to consider not only the peak strength but also the post-peak strength when conducting the back analysis to capture the failure zone. At the end, when back analyzing, all modeling parameters as described in this chapter should be considered consistently as a system.

Chapter 5

Numerical modeling of brittle rock failure around underground openings under dynamic stress loading

5.1. Introduction

Under high static stresses, fracture and damage of rock mass around an opening can result from high mining-induced stresses, leading to brittle rock failure around the excavation boundary. In burst-prone grounds, mining-induced seismicity can cause additional dynamic loading which may further increase the stress around the tunnel, leading to more failure, loosening, sudden release of elastic strain energy stored in the failing rocks and the surrounding rock masses, and potentially violent ejection of the failed rock masses (Kaiser et al., 1996).

Once the anticipated seismic damage risk is recognized, it is important to control the potential damage caused by the seismic event. First, the demands that will be imposed on the support systems need to be estimated. Then, rock support with sufficient capacity must be designed and installed to control the potential failure zone, to provide a safe environment for the underground workers, and to avoid disruption to mine production. One method to estimate the support capacity under dynamic loading is the energy approach, which is based on the estimation of the maximum ejection velocity (Stacey & Ortlepp, 1993). Another method relies on a reasonable estimate of the ultimate depth and extent of the failed rocks under both static and dynamic loadings. It is important to anticipate the brittle rock failure zone around the excavation under both static and dynamic loadings to achieve this goal.

5.2. Purpose of the study

As indicated previously in Chapter 2, the depth of failure under static loading can be estimated empirically and/or numerically. The empirical approach utilizes an equation summarized by surveying actual field tunnel failure of some underground projects around the world (Martin et

al., 1999) (see Figure 2-21). The numerical approach emphasizes predicting the depth of failure using either a suitable numerical tool and/or a suitable failure model. For example, the cohesion-weakening frictional-strengthening (CWFS) model (Hajiabdolmajid et al., 2002), the spalling failure model (Diederichs, 2007), and as demonstrated in Chapter 4, the brittle Mohr-Coulomb model, can be used to approximate brittle rock failure near the excavation boundary.

Similarly, the depth of failure under dynamic loading can be estimated using either the empirical approach or the numerical approach. One empirical method considers adding a dynamic stress increment to the total excavation-induced tangential stress at the tunnel boundary to estimate the depth of failure due to dynamic loading, using the same empirical equation for static loading (Figure 2-24). The influence of seismic and dynamic loading on stress changes around the opening and consequently on the depth of failure had previously been investigated (Wang, 1993; Vasak & Kaiser, 1995; Lanzano et al., 2009). Some of their results played the role of developing the empirical relationship for estimating depth of failure under dynamic loading.

It has been observed that further research is needed to model rock failure under dynamic loading. This observation is largely driven by the fact that new understanding about brittle rock failure has been gained in recent years. In the work by Vasak and Kaiser (1995), a strain-softening model was used in FLAC to simulate the rock mass failure, allowing 0.2% plastic strain for a full friction mobilization and cohesion loss. As previously mentioned, the behavior of a rock mass under low confining conditions, such as those near the tunnel boundary, is brittle, which means that there is a sudden reduction of rock mass strength from peak to “residual” once failure occurs. In Chapter 4, a brittle material model was used to approximate the failure zone near the boundary of the Mine-by tunnel under static loading. Brittle rock failure is likely to occur under

dynamic loading; hence it is the motivation to conduct a study to investigate the dynamic rock failure near excavation boundaries using a brittle material model.

5.3. Description of the modeling procedure

In this study, a modeling approach using brittle rock strength parameters will be used to simulate the depth of failure around a circular tunnel under dynamic loading. The model geometry and boundary condition of a tunnel similar to the Mine-by tunnel to demonstrate the effect of dynamic loading on rock failure is used in this thesis. This was based on the observation that the strength parameters should first be calibrated against field monitoring data such as notch breakout before commencing the dynamic modeling. The Mine-by tunnel provided the data required to achieve the objective of model parameter calibration. Because the Mine-by tunnel experienced no rockburst or seismic event, it was not possible to verify the simulated depth of failure around the tunnel under dynamic loading. The underlying assumption here is that because we used a calibrated brittle model for the dynamic stress analysis, it was expected that we would have a better chance capturing the depth of failure accurately if a similar dynamic loading were to occur.

Accordingly, several intensities of dynamic stress wave are applied to the model and the corresponding rock failure patterns are studied. For comparison, we also conduct numerical modeling using a strain-softening model.

5.3.1. Dynamic loading and boundary conditions

As previously summarized in Section 2.2.2, fault slips cause the largest seismic events encountered in a mining environment. In the present study, the simulation will consider seismic

waves generated by a large seismic event travelling in the rock mass, reaching the tunnel, and causing dynamic stress increase in the rock mass around the tunnel. Coupled with the excavation-induced stress, the total stress may cause the rock mass to fail. Usually, the stress waves generated by large magnitude seismic events have a dominant low frequency, ranging between 10 and 50 Hz (Hedley, 1992; Aswegen & Butler, 1993). Because p-waves are the fastest seismic waves, they will usually be the first ones to appear on a seismograph. The next set of seismic waves to appear on the seismogram is the s-waves, which have high ground motion amplitudes and are therefore the main source that causes large stress change in the rock. For simplicity, only the s-waves will be considered in this study.

The effect of stress wave loading on rock failure around the tunnel is simulated by applying a dynamic shear stress boundary at the lower boundary of the numerical model shown in Figure 5-1. The diameter of the circular tunnel is 3.5 m and the model size is 40 m × 40 m. Free-field boundaries are applied along the vertical and top boundaries of the model to absorb energy and allow propagation of stress wave through the model without boundary reflections. Because the dynamic input is a stress boundary, quiet (absorbing) boundaries are assigned in the direction of wave propagation to the top and lower boundaries to avoid the reflection of outgoing wave back to the model and the movement of the entire model downwards due to gravity acceleration.

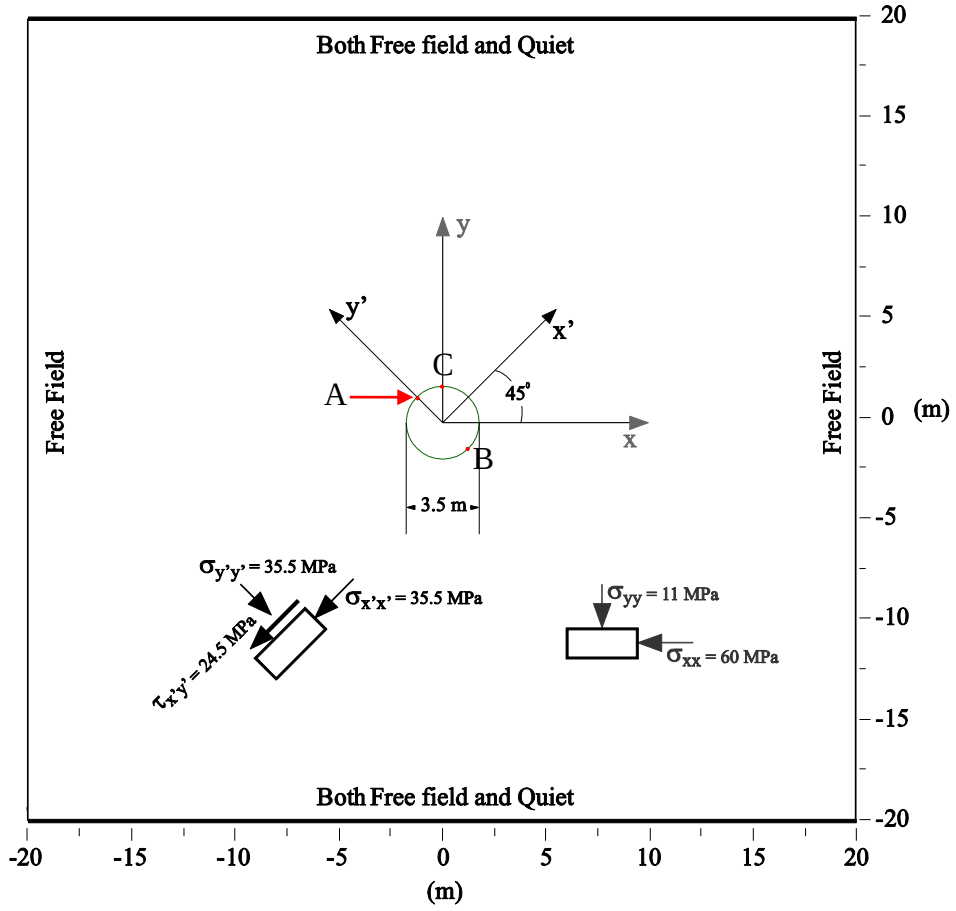

Figure 5-1: Model geometry and boundary conditions for the dynamic failure analysis.

The dynamic input is applied as a shear stress wave at the bottom boundary, and the peak shear stress τ_s is obtained from Eq. (9):

$$\tau_s = 2(\rho C_s)\, ppv \tag{9}$$

where ρ is the mass density (kg/m^3) and *ppv* is the peak particle velocity which can be determined using a design scaling law (Kaiser et al., 1996):

$$ppv = C^* \frac{{M_0}^{a^*}}{R}, \tag{10}$$

where M_0 is the seismic moment in GN·m (seismic moment can be related to the event magnitude), R is the distance between the tunnel location and the seismic source in m, and a^* and C^* are empirical constants. Finally, C_s is the s-wave propagation velocity of the medium which can be obtained from Eq. (11):

$$C_s = \sqrt{G/\rho} \tag{11}$$

where G is the shear modulus of the rock mass.

In the present study, the shear stress is multiplied by a sinusoidal time history function, pulsing at 10 Hz frequency, to create a synthetic stress wave similar to the wave form illustrated in Figure 5-2 (*ppv* = 0.65 m/s, G = 24 GPa, ρ = 2500 kg/m^3). Using the synthetic stress wave, it is easy to validate the stress wave transmission through the model. The stress wave needs to be applied at a 45° angle relative to the maximum in-situ principal stress direction to ensure that the shear stress wave has a maximum influence on rock failure (SCRTD, 1984). In the model shown in Figure 5-1 the synthetic stress wave is applied to the bottom boundary, in the horizontal direction. Instead of applying the wave at a misaligned angle to maximize the effect of the stress wave on dynamic stress increase near the tunnel wall, the in-situ stress field defined by σ_{xx} and σ_{yy}, as illustrated in Figure 5-1, is rotated by 45°. In this way, a combination of static and dynamic stresses will induce maximum tangential stresses at locations A and B indicated in the figure.

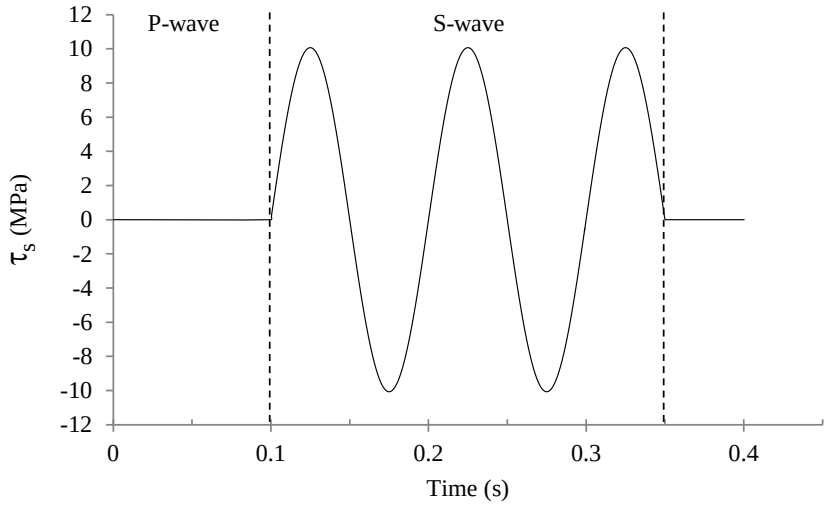

Figure 5-2: The synthetic stress wave form used in this study.

An elastic stress analysis is conducted first for an in-situ stress field of σ_1 = 60, σ_2 = 45, and σ_3 = 11 MPa. σ_2 is parallel to the tunnel axis, and σ_1 and σ_3 are oriented in the x and y directions, respectively. Under this in-situ stress condition, the maximum tangential stress occurs at point C (see Figure 5-1). When the in-situ stress components are rotated 45° from the horizontal, the maximum tangential stress occurs at points A and B. The Young's modulus and Poisson's ratio of the rock are 60 GPa and 0.25, respectively. As a result of the shear stress wave loading (Figure 5-2), the variation of the maximum tangential stresses over time at points A (in-situ stress rotated) and C (in-situ stress not rotated) are plotted in Figure 5-3. Before the stress wave arrives, the maximum principal stresses at points A and C are 165.5 MPa and 158.9 MPa, respectively. The difference in stress magnitude is partially attributed to the outside boundary effect and partially due to the shear wave loading effect. When the in-situ stress is rotated 45° from the horizontal, the diagonal distance of point A to the outside boundary is larger than the horizontal distance of point C to the outside boundary. Hence, there is a stress difference of

165.45 – 158.90 = 6.55 MPa before the shear stress wave arrives. When the shear stress wave arrives, more stress change occurs at point A than at point C because a shear stress wave applied at the bottom causes the largest stress increase in the directions of ±45°. Coupled with the static stress, it is seen that for the case with the in-situ stress rotated 45° from the horizontal, more stress disturbance will be induced to the rocks near the tunnel boundary at point A (and B).

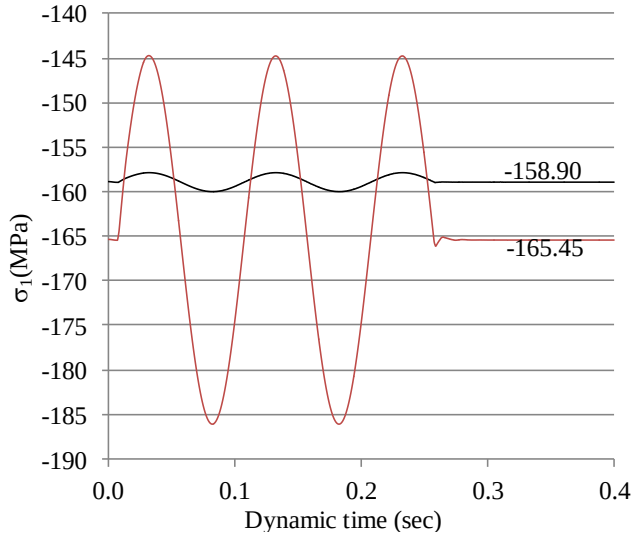

Figure 5-3: Comparison of the stress change caused by the same seismic wave at point C (black line, without in-situ stress rotated 45°) and point A (red line, with in-situ stress rotated 45°).

5.3.2. Wave transmission through the model

As explained above, the dynamic loading is a sinusoidal shear stress wave applied at the base of the model in the x-direction. The magnitude of the stress wave is a function of *ppv* (see Eq. (10) and the wave frequency is 10 Hz. For the given rock, the shear wave velocity calculated from Eq. (11) is 3098 m/s. The largest zone dimension (Δl) of the numerical model is 0.1 m. The relation between the longest wave length (λ) and the maximum frequency is:

$$f = \frac{C_s}{\lambda} = \frac{C_s}{10\Delta l} \tag{12}$$

Using Eq. (12), it was found that the maximum frequency which can be modeled accurately is over 3000 Hz. Therefore the current zone (mesh) size is small enough to allow wave at the input frequency (10 Hz) to propagate accurately in the model. In addition, to increase the accuracy of the dynamic analysis, the mesh needs to be as uniform as possible throughout the model. The mesh used for the dynamic modeling in this study is shown in Figure 5-4.

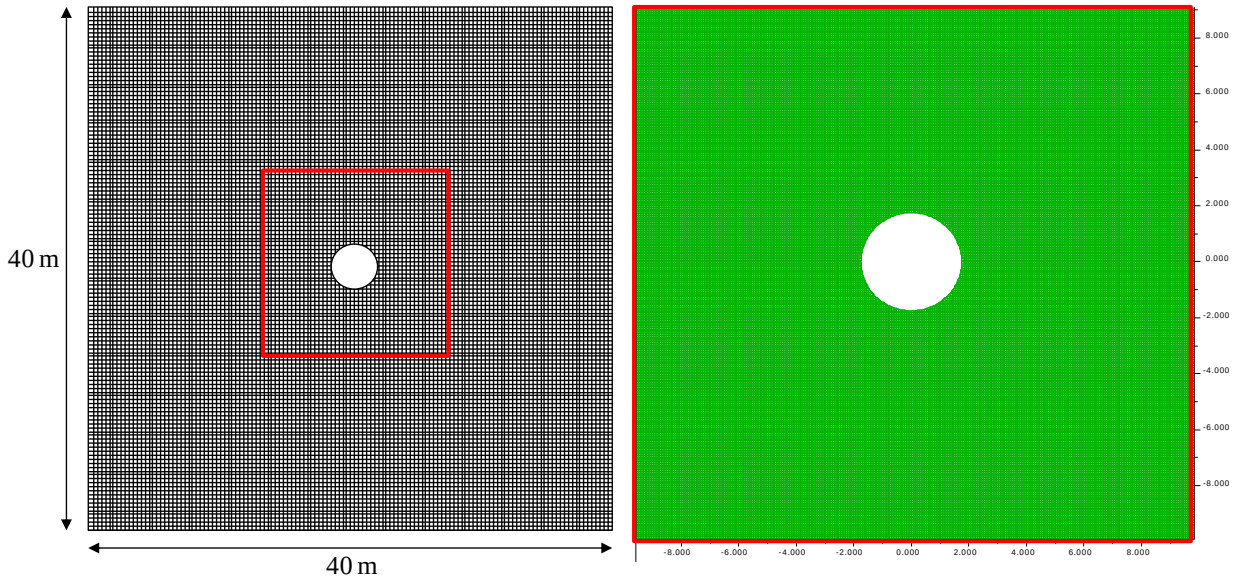

Figure 5-4: The uniform fine mesh utilized in the dynamic modeling approach; the right figure is a zoom-in figure of the left to emphasize on the density of the used mesh.

5.3.3. Mechanical damping

One factor that influences dynamic stress wave propagation within the model is mechanical damping. Natural dynamic systems contain some degree of damping which absorbs part of the vibration energy within the system; otherwise, the system would oscillate indefinitely when

subjected to vibration. Damping is due, in part, to energy loss as a result of internal friction in the intact material and slippage along interfaces (Itasca, 2002). Hence, it is necessary to consider the effect of damping when modeling stress wave propagation in the model.

There are several types of dynamic damping available in FLAC, such as *Rayleigh* damping, artificial viscosity damping, and local damping. Local damping is used in FLAC even for static stress analysis. An elastic model was run with no damping explicitly specified, with local damping specified, and with a small amount of *Rayleigh* damping specified (5%, at 10 Hz frequency) to evaluate the influence of damping on the modeling result. The stress at point A (Figure 5-1) is tracked, using a model grid with uniform 10 cm mesh size (input shear wave is as illustrated in Figure 5-2 without the p-wave section). From the results plotted in Figure 5-1, it is seen that the results when specifying no damping are the same as that of specifying local damping because local damping is in fact the default damping in FLAC. A small difference between the results with the *Rayleigh* damping and local damping exists. For simplicity, the default damping is used in the dynamic modeling.

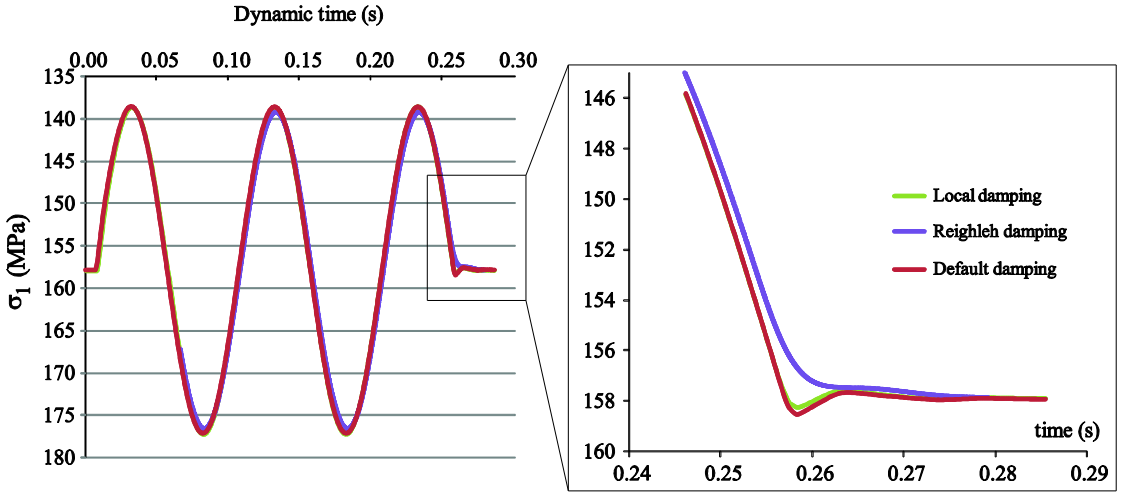

Figure 5-5: Influence of damping in an elastic analysis, comparing different types damping.

5.4. Dynamic response

Two scenarios of rock failure are considered in the study. In the first scenario, rock failure in the form of notch breakout occurred under static stress loading. The incoming dynamic stress wave further expands the failure zone. In the second scenario, the rock strength is higher than the maximum stress under static loading on the tunnel boundary. Hence, no failure will occur when the tunnel is excavated. When the dynamic stress wave is applied to the model, a dynamic stress increase will be generated in the rock around the tunnel. If the combined stress (static plus dynamic stresses) is high enough, failure will occur around the tunnel.

It is understood that the material properties under dynamic loading are different from those under static loading. Rock strength is generally higher under dynamic loading than that under static loading (Olsson, 1991; Cai et al., 2007). For simplicity, we assume that the same peak and post-peak rock strength envelopes calibrated under static loading are applicable to dynamic loading.

5.4.1. Deepening of depth of failure by dynamic loading

In the present study, we first simulated the extension of the notch failure of the tunnel under dynamic stress loading. The purpose was to use a calibrated model to understand how the rock would respond under dynamic loading, which can be generated by fault-slip induced by rockbursts or natural earthquakes. The insight gained from such a failure process analysis could assist us to design better rock support systems for underground construction.

The modeling procedure was as follows. First, the model was run under static loading until reaching equilibrium state. A static equilibrium can be obtained only if sufficient cycling steps are taken. In general, about 50,000 cycling steps are required before the unbalanced force

reaches an insignificant value. This is especially important in an analysis in which rock failure occurs. The failure zone around the tunnel was plotted and compared with the field observation data. The model parameters were adjusted to match the modeling results to the field observation.

Next, the dynamic analysis was initiated and the model was run until the stress wave input was finished, then the model was run until the stress wave passed the top boundary. Failure due to dynamic loading was then analyzed. For comparison, we conducted numerical modeling using both the brittle and the strain-softening models. The tensile strength and dilation angle were 30 MPa and 30 degrees, respectively. The reason for assigning such a high tensile strength value was to focus the failure analysis in the compression zone.

Under static loading with an in-situ stress field of σ_1 = 60 MPa and σ_3 = 11 MPa, where σ_1 was rotated 45° from horizontal, the failure zones around the tunnel when the tunnel is excavated are plotted with green filling in Figure 5-6a and b for the strain-softening and the brittle material models, respectively. The peak and post-peak strength envelopes of the two models are shown as inserts in the figures. In the strain-softening model, the characteristic plastic strains for cohesion and friction angle are 0.2% and 0.5%, respectively. In the brittle rock model, as discussed in Chapter 2, a extremely small value for the characteristic plastic strain is used in FLAC to realize instant friction mobilization and cohesion loss post-peak.

The 10 Hz frequency sinusoidal shear waves with two stress intensities (*ppv* = 0.65 and 1.3 m/s) were applied to the model which had been in equilibrium statically. In this case, notch failure had already occurred under static loading. Hence, the dynamic stress wave loading would increase the failure zone. The failure zone increases are shown in Figure 5-6 by blue and red colors for

the wave intensities of *ppv* = 0.65 m/s and 1.3 m/s, respectively. The stronger shear wave indicated with the red zone extends further over the blue zone in Figure 5-6a, where a strain-softening material is used. In Figure 5-6b, where the brittle material model with parameters specified in Table 4-1 is used, the red zone extends differently compared with that in the strain-softening material.

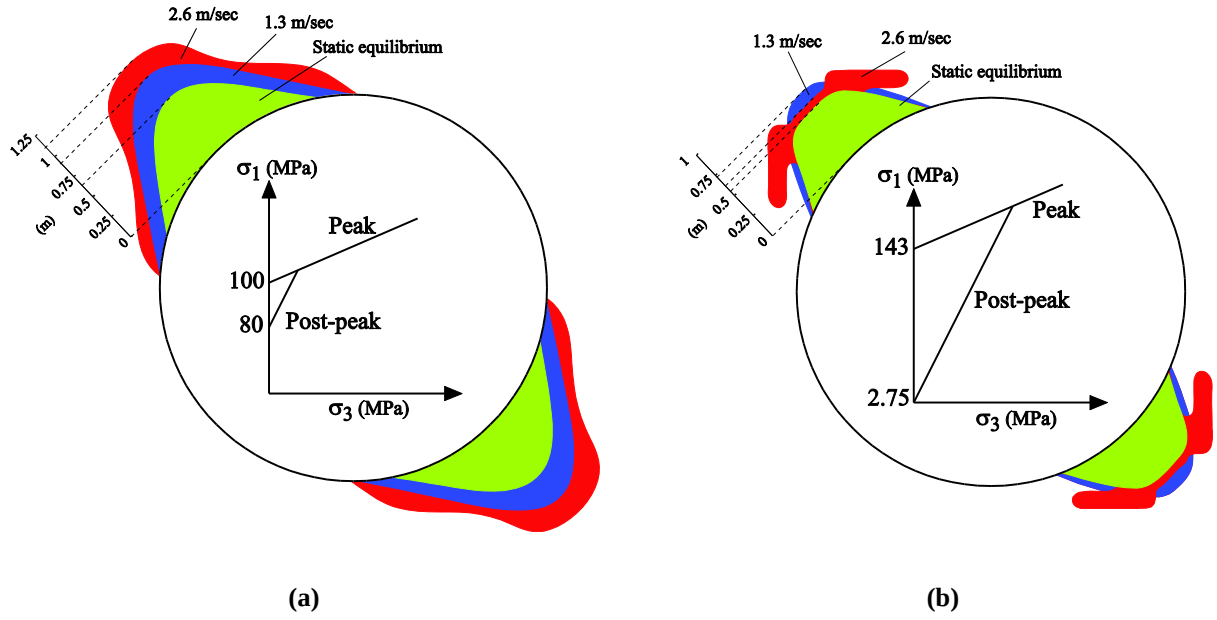

(a) **(b)**

Figure 5-6: Influence of dynamic loading on the depth of failure: (a) strain-softening model; (b) brittle model (Note that the peak and post-peak strengths are different in the two models).

As shown in Figure 5-6a and b, the same dynamic wave would induce different degrees of additional failure to the rock depending on the strength models used. In the strain-softening model, the failure zone depth and extent were larger than that in the brittle model, when only considering the elements that enter plastic deformation. It is not appropriate to determine the failure zone based on the yielded element plot alone from a numerical exercise without

mentioning the strength model used. Depending on the peak and particularly the post-peak strength parameters used, the remaining stresses in the failure zone can be very different.

Figure 5-7a and b, shows the differential stress distributions after the tunnel was excavated for both the strain-softening and the brittle models. Using the strength parameters in the strain-softening model, the failure zone indicated by yielded elements matches the Mine-by tunnel notch shape obtained from field observation. The differential stresses inside the notch were in the range of 60 to 100 MPa in the strain-softening model results (see Figure 5-7a). On the other hand, the differential stress distribution given by the brittle model was mostly in the range of 0 to 20 MPa (see Figure 5-7b). Low stresses in the zone where notch eventually formed represents slightly better the zone of failure in the context of continuum modeling, but is still far from reality where a discontiuum damage process occurred resulting in slabbing and spalling of failed rocks. In a continuum model, it is not possible to completely release all the stresses in the failure zone. In the brittle model, high stresses at the tip of the notch may prevent further propagation of the failure zone under loading. This is largely due to the choice of a higher post-peak friction angle (than the peak friction angle) and the resulting hardening stress path of some elements in this zone may experience (see Figure 2-20).

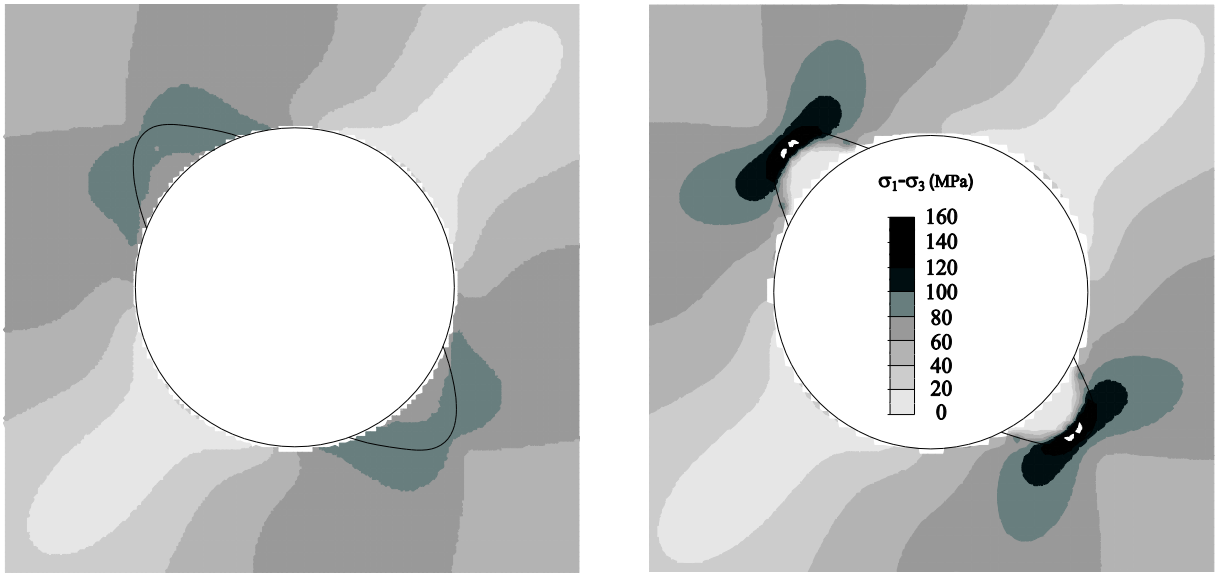

(a) **(b)**

Figure 5-7: $\sigma_1 - \sigma_3$ **stress distribution in the rock when the notches (identified in figures) are formed under static stress loading: (a) strain-softening model; (b) brittle model.**

The dynamic loading of a seismic wave further increases the stress in the rock. Depending on the material model and the strength parameters, the failure zone may propagate differently. In the strain-softening model, the stresses in the notch failure zone (under static loading) were high. Therefore, elements just outside the notch boundary could carry high stresses and this made it easier for these elements to fail under additional dynamic loading, leading to failure zone expansion as shown in Figure 5-6a. In the brittle model, on the other hand, the stress concentration zone was located at the tip of the notch failure zone (see Figure 5-7b) and additional stress increase induced by the seismic wave caused additional failure in the highly stressed areas. When *ppv* is equal to 0.65 m/s, the shape of the additional failure zone due to dynamic loading is similar to that in the strain-softening model, but the depth of failure is smaller. For *ppv* = 1.3 m/s, wing-shaped failure zones were created by the dynamic loading in

the brittle model, which was different from that in the strain-softening model (red and blue areas in Figure 5-6a and b).

5.4.2. Creation of rock failure due to subsequent dynamic loading

In many underground openings and mines, tunnels were stable after excavation because the rock strength was higher than the maximum excavation or mining-induced stress. However, when a fault-slip event occurred, the seismic wave could cause rock failure in tunnels located away from the seismic source. In the following discussion, rock failure is studied in a tunnel located in a weaker rock with a different in-situ stress field from the previous example. The peak and post-peak strength parameters of both the brittle and strain-softening models are presented in Table 5-1. The model parameters were chosen in such a way that upon the tunnel excavation, there would be no rock failure. Rock failure was only induced by subsequent dynamic loading. In the example shown above, the ratio of the principal in-situ stresses (K_o ratio) was 5, which was extremely high. For this simulation, σ_1 = 30 MPa and σ_3 = 15 MPa (K_o = 2) are used. Again, the maximum principal stress was rotated 45° from the horizontal to maximize the stress increase due to dynamic stress loading. The shear stress wave was applied to the bottom boundary of the model (Figure 5-1).

Table 5-1: Strength parameters for the brittle and strain-softening models

		Brittle	Strain-softening
Peak	c (MPa), ε_p (%)	26, 10^{-10}	26, 0.2
	ϕ (°),ε_p (%)	10, 10^{-10}	10, 0.3
Residual	c (MPa), ε_p (%)	0.5, 10^{-10}	0.5, 0.4
	ϕ (°),ε_p (%)	50, 10^{-10}	50, 0.5

Figure 5-8 presents the differential stress distributions and the failure zone distribution in the rock for the brittle and the strain-softening models. As expected, no rock failure occurs under static loading using either modeling approach, which means that after tunnel excavation, the maximum tangential stress at the tunnel wall was less than the wall strength of 62 MPa. Under dynamic loading, new rock failure zones were formed in the direction in which the combined tangential stress was the maximum. The depth of failure was higher for the case with the higher dynamic stress increase (Figure 5-8).

Figure 5-8 shows that when the peak and post-peak strengths of the brittle and strain-softening models are the same (see Table 5-1), respectively, the depth of failure zone by the brittle model is similar to that of the strain-softening model while the extent is larger.

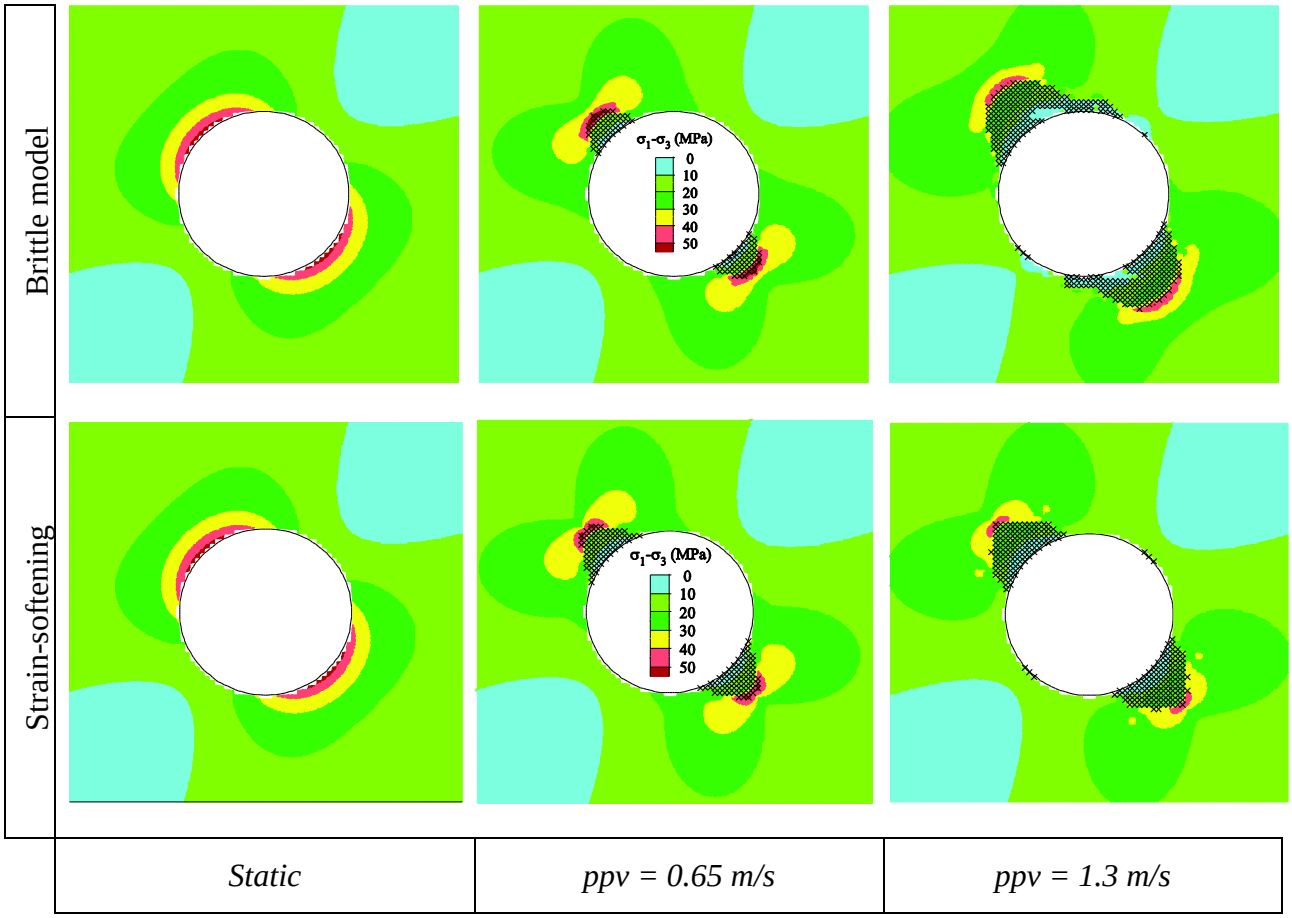

Figure 5-8: Depth of failure under static and dynamic loading for brittle and strain-softening models.

Kaiser et al. (1996) presented Figure 2-24 which plots the normalized depth of failure (d_f/a) as a function of normalized tangential wall stress to the uniaxial compressive strength of the original rock (σ_{max}/σ_c) and *ppv*. In Figure 5-9, the counter lines of normalized depth of failure are plotted against the normalized tangential stress (σ_{max}) to the strength of the rockmass (σ_{cRM}). The empirical static contour line given by Kaiser et al. (1996) is also shown in Figure 5-9.

Based on the numerical modeling results, we plot a few contour lines relating depth of failure to the stress to strength ratio and *ppv* in Figure 5-9 for the strain-softening (blue lines and blue markers) and the brittle models (red lines and red markers). Under static loading (*ppv* = 0), the

depth of failure predicted by both models is in reasonable agreement with that of the empirical relation given by Kaiser et al. (1996). Although there are some differences between the results of the strain-softening and the brittle models, the differences are nevertheless small when the stress to strength ratio is low ($\sigma_{max}/\sigma_{cRM}$ = 1). When the stress-to-strength ratio is high, the numerical modeling tends to predict a smaller depth of failure, regardless of the post-peak behavior of the rock.

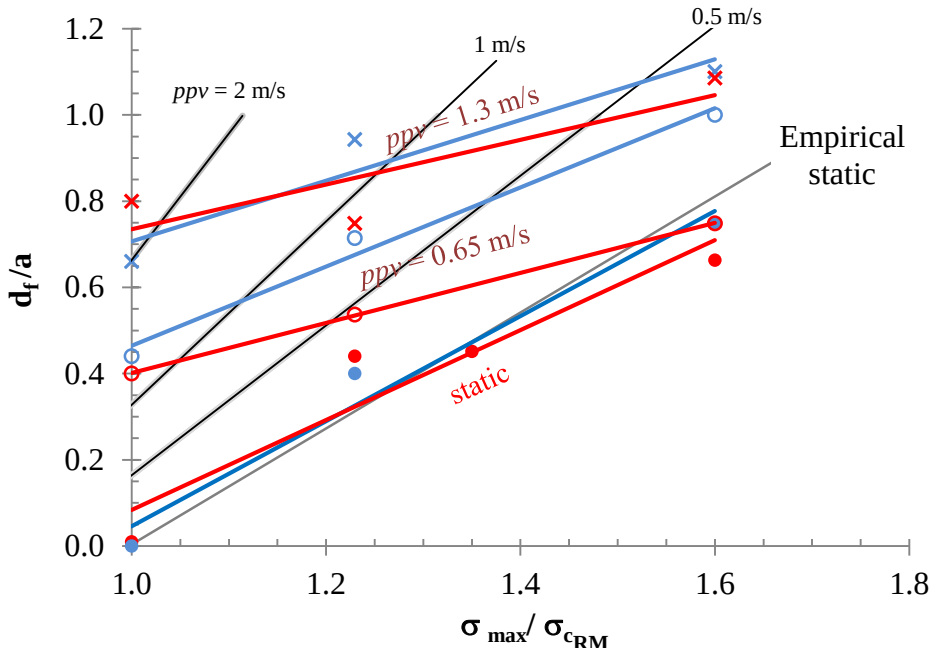

Figure 5-9: Comparison of the simulated depth of failure by a brittle model (red lines and markers) and a strain-softening model (blue lines and markers).

Under dynamic loading, the slopes for the depth of failure contours by the current numerical modeling are smaller than these given by Kaiser et al. (1996), but their intercepts to the d_f/a axis are higher than these by the previous results. This means that for a given *ppv*, the numerical model predicts smaller and larger depth of failure zones when the stress to strength ratio is high and low, respectively. For example, when the stress to strength ratio $\sigma_{max}/\sigma_{cRM}$ is 1.2 and the

tunnel diameter is 6 m, the brittle model will predict depths of failure of 1.5 m and 2.5 m under *ppv* = 0.65 m/s and 1.3 m/s dynamic loading, respectively. On the other hand, the depths of failure would be 1.65 m and > 4.5 m under *ppv* = 0.65 m/s and 1.3 m/s dynamic loading according to Kaiser et al. (1996).

This discrepancy highlights that while the depth of failure under static loading can be reasonably estimated, capturing the depth of failure under dynamic loading is strongly related to the model's post-peak behavior and the strength parameters assigned to the model.

5.5. Summary

A parametric study with two different intensities of input stress wave was carried out, employing both the brittle and the strain-softening models. For each case, the dynamic depth of failure was plotted as a function of the ratio of maximum tangential stress to the rock mass strength as well as the dynamic stress wave intensity expressed by the peak particle velocity. By comparing the numerically simulated depth of failure with that given by the empirical relationships, we note that:

- The simulated depth of failure depends on the material model and the strength parameters used. Both the brittle and the strain-softening models can be used to simulate rock failure under dynamic loading. When both the peak and post-peak strengths are the same in the brittle and strain-softening models, the depth of failure by the brittle model is larger than that of the strain-softening model. However, the depth of failure given by the brittle model with a high peak strength and a low post-peak strength can be smaller than that given by the strain-softening model with a low peak strength and a very high post-peak strength. Therefore,

judging the depth of failure only by the yielded elements in the numerical model can be misleading. One needs to examine the type of strength model used and the strength parameters applied.

- Under static stress loading conditions, the depths of failure given by the current numerical model with the calibrated material parameters are in reasonable agreement with those given by the empirical relations, regardless of the post-peak behavior of the rock.
- Under dynamic stress loading conditions, the simulated depths of failure are higher than those given by the empirical relations when stress to strength ratio is low. However, when the stress to strength ratio is high, the numerically simulated depths of failure are smaller than those given by the empirical relationships regardless of the post-peak material model used.
- Because of the discrepancy identified, we recommend that further research is needed to collect field data with ground motion and failure monitoring to verify the numerical simulation and empirical results.

Chapter 6

Summary and future work

6.1. Summary

A study on stress-induced instability in underground openings is reported in this thesis. First, rock failure under static stress loading is investigated, followed by rock failure analysis under dynamic loading. In particular, the case where mining-induced seismicity further expands the static failure zones around the opening was considered.

At the beginning, previous approaches in modeling brittle rock failure under static loading conditions were examined. Some insights gained from this study are summarized below:

- Using a higher mesh density in the periphery of the opening, especially when conducting a plastic analysis, is important to model the failure zone properly. When the stress near the excavation boundary is underestimated because of using a coarse mesh, the rock strength will also be underestimated.
- In tunneling, different excavation methods will lead to different stress paths. It is important to account for the effect of the excavation method properly to simulate stress-induced rock failure in 2D. It was demonstrated that both the load-split and core-softening techniques can be used to simulate rock failure. The two methods can lead to different results if the failure does not occur in the zone where the minimum principal stress is low. This could happen when the assigned peak strength is low. If the assigned rock strength is high, failure occurs at the low confinement zone and the difference between the two methods is small.
- Another aspect which can affect the simulation result is the outside boundary size. When a small model is used, it underestimates the maximum tangential stress at the tunnel wall, which in turn leads to underestimating the rock strength. The problem can be avoided by

ensuring that the outside boundary is at least 5 times the opening diameter away from the excavation boundary.

- Various failure models, such as the plastic strain-dependent cohesion-weakening frictional-strengthening model and the spalling parameter model, have been used to simulate brittle rock failure in the past. It is demonstrated in this study that a brittle Mohr-Coulomb model can also be used to approximate brittle failure. This method simplifies the modeling effort in two aspects: one is that there are fewer model parameters to be determined and the other is that the modeling can be conducted using the popular numerical tool PHASE^2 in which only brittle material models are available.
- Fractured rocks will lose all their cohesive strength and their remaining post-peak strength is only frictional strength. The frictional strength can be mobilized only if the fractured rocks are confined. It is understood that the true residual strength state can only be reached if the sample is allowed to strain sufficiently beyond peak in a controlled manner. In the absence of such test results and based on the consideration that rocks near a tunnel wall may not be strained extensively, it was assumed that under low confinements a post-peak friction angle higher than the peak friction angle is possible in this study. However, under high confinements, this assumption may not be valid and it could lead to a strain hardening in the numerical model response.
- The strength parameters back analyzed with each method are inter-connected with all the settings within the model. This inter-connectivity of model parameters was investigated and the influence of each individual modeling parameter on the resulting failure zone and stress path was systematically analyzed.

At the second step, some previous studies on modeling brittle rock failure under dynamic loading were reviewed. The results of the current study were used to cross-check with a previously developed empirical chart for estimating the dynamic depth of failure. This led to investigating the development of brittle failure around a circular tunnel under first static loading and furthermore under two different intensities of dynamic loading. In this study it was noted:

- Under dynamic stress loading conditions, when the post-peak strength is low, the simulated depths of failure using a strain-softening model are generally higher than those given by a brittle model. However, when the stress-to-strength ratio is low, the differences between the two depths of failure are minimal. Only when the stress-to-strength ratio is high will the differences become large, which renders the selection of the post-peak behavior an important task.
- The results of this investigation were compared side by side with the empirical charts. The circular shape of the simulated tunnel in this study inherently tends to underestimate the depth of failure. The slopes for the depth of failure contours lines by the current numerical modeling are smaller than those given by Kaiser et al. (1996). This difference is largely due to selecting a frictional post-peak strength envelope in which the friction angle is higher than the peak friction angle. This may have led to a hardening process in the high confinement zone which stops further development of stress-induced failure.
- Field observations are required to provide some evidence for the findings in this study. In general, there is a lack of well documented case studies which detail the dynamic stress loading and the depth of failure.

6.2. Future work

The research presented in this thesis seems to have raised more questions than it has provided answers. There are several areas of future research which could be pursued to further advance our understanding of brittle rock failure:

- One future research is to model brittle rock failure around the boundary of tunnels with different shapes. Circular tunnels are used in TBM tunneling and most of the tunnels in mining are non-circular in shape, which may cause stress concentration at corners that promotes additional failure.
- Another research is to combine a recently proposed mobilized dilation model (Zhao & Cai, 2010) with the brittle Mohr-Coulomb model to simulate rock failure and deformation around tunnels. This may leads to improved representation of rock deformation from numerical modeling.
- Considering the depth of failure only in rock support design many not be sufficient and the extent of the failure zone needs to be considered as well. Future research is needed to include failure zone extent as the second dimension in rock support design decision-making.
- From Chapter 5 it has been realized that more field data need to be collected from carefully documented case studies that experienced dynamic loading. Without this valuable information, it would be difficult to gain confidence on both the empirical and the numerical modeling results.
- The dynamic input wave used in this study was a simplified synthetic wave. In reality, the seismic wave is more complex with different frequency components. Further research is required to model the brittle rock failure using real-world measured wave form input to the

model. The influence of compression and shear stress waves needs to be investigated separately and compared together for identifying a worst case scenario.

Bibliography

Andersson, J.C., 2007. *Rock mass response to coupled mechanical thermal loading. Äspö Pillar stability experiment, Sweden*. Ph.D. thesis. Sweden: SKB KTH, School of Architecture and the Built Environment (ABE), Civil and Architectural Engineering, Soil and Rock Mechanics

Andersson, J.C. & Martin, C.D., 2009. The Äspö pillar stability experiment: Part I—Experiment design. *International Journal of Rock Mechanics and Mining Sciences*, 46(5), pp.865–78.

ASTM., 2010. Standard test for compressive strength and elastic moduli of intact rock core specimens under varying states of stress and temperatures, *American Society for Testing and Materials (ASTM)*, D7012 – 10

Aswegen, G. & Butler, A.G., 1993. Applications of quantitative seismology in South African gold mines. In Young, R.P., ed. *In Proceedings of Rockbursts and Seismicity in Mines, Kingston*. Balkema, Rotterdam, 1993.

Bieniawski, Z.T., 1967. Mechanism of brittle fracture of rock: Part II—Experimental studies. *International Journal of Rock Mechanics and Mining Sciences and Geomechanics*, 4(4), pp.407–08.

Bieniawski, Z.T., 1974. Estimating the strength of rock materials. *Journal of South African Institute of Mining and Metallurgy*, 74(8), pp.312-20.

Brady, B.H.G. & Brown, E.T., 2004. *Rock Mechanics: For Underground Mining*. 3rd ed. Netherland: Springer.

Cai, M., 2008. Influence of stress path on tunnel excavation response – Numerical tool selection and modeling strategy. *Tunnelling and Underground Space Technology*, 23(6), pp.618–28.

Cai, M., Kaiser, P.K. & Duff, D.J., 2012. Rock support design in burst-prone ground utilizing an interactive design tool. Chicago: *ARMA-American Rock Mechanics Association*.

Cai, M., Kaiser, P.K., Suorineni, F. & Su, K., 2007. A study on the dynamic behavior of the Meuse/Haute-Mame Argillite. *Physics and Chamistry of the earth*, 32(8), pp.907-9016.

Cai, M. et al., 2004. Generalized crack initiation and crack damage stress thresholds of brittle rock masses near underground excavations. *International Journal of Rock Mechanics and Mining Sciences*, 41(5), pp.833-47.

Cai, M., Kaiser, P.K., Tasaka, Y. & Minami, M., 2007. Determination of residual strength parameters of jointed rock masses using the GSI system. *International Journal of Rock Mechanics and Mining Sciences*, 44(2), pp.247–65.

Castro, L., 1996. *Analysis of stress-induced damage initiation around deep openings excavated in a moderately jointed brittle rock mass*. PhD thesis. University of Toronto.

Cheon, D.S., Park, C., Jung, Y.B. & Jeon, S., 2006. Modeling brittle failure of rock using damage-controlled test. *Proc. of the 4th Asian Rock Mechanics Symposiumm*, Singapore

Corkum, A.G. & Martin, C.D., 2007. The mechanical behaviour of weak mudstone (Opalinus Clay) at low stresses. *International Journal of Rock Mechanics and Mining Sciences*, 44(2), pp.196-209.

Corthesy, R. & Leite, M., 2008. A strain-softening numerical model of core discing and damage. *International Journal of Rock Mechanics and Mining Sciences*, 45(3), pp.329–50.

Counter, D., 2010. *Geotechnical mine design package and 2009 Annual mine stability review*. Xstrata Copper Kidd Creek Mine.

Diederichs, M.S., 2007. Mechanistic interpretation and practical application of damage and spalling prediction criteria for deep tunnelling. *Canadian Geotechnical Journal*, 44(9), pp.1082-116.

Eberhardt, E., 2001. Numerical modelling of three-dimension stress rotation ahead of an advancing tunnel face. *International Journal of Rock Mechanics and Mining Sciences*, 38(4), pp.499–518.

Edelbro, C., 2010. Different approaches for simulating brittle failure in two hard rock mass cases: A parametric study. *Rock Mechanics and Rock Engineering*, 43(2), pp.151-65.

Everitt, R.A., 2001. *The influence of rock fabric on excavation damage in the Lac du Bonnet granite*. Ph.D. Thesis. Winnipeg, Manitoba, Canada: Univeristy of Manitoba.

Franklin, , 1971. Triaxial strength of rock material. *International Journal of Rock Mechanics and Mining Sciences and Geomechanics Abstracts*, 2(3), pp.86-98.

Golchinfar, N. & Cai, M., 2012. Modeling depth of failure using brittle mohr-coulomb failure model. In *21st Canadian Rock Mechanics Symposium*. Edmonton, Alberta, 2012.

Grabinsky, M.W., Corkum, B.T. & Curran, J.H., 1995. *Numerical Stress Analysis of Proposed Shafts at Placer Dome Inc.'s Campbell Mine*. CRRp report.

Graham, C.B., 1995. *Rockburst Research Handbook*. Sudbury, Ontario: CAMIRO Mining Division.

Hajiabdolmajid, V.R., 2001. *Mobilization of Strength in Brittle Failure of Rock*. Ph.D. thesis. Kingston, Ontario, Canada: Queen's Univeristy.

Hajiabdolmajid, V., Kaiser, P.K. & Martin, C.D., 2002. Modelling brittle failure of rock. *International Journal of Rock Mechanics and Mining Sciences*, 39(6), pp.731-41.

Hakala, M. & Heikkila, E., 1997. *Laboratory testing of Olkiluoto mica gneiss in borehole OL-KR10*. Helsinki, Posiva oy: POSIVA-97-07e.

Hedley, D.G.F., 1992. *Rockburst Handbook for Ontario Hardrock Mines*. CANMET Special Report SP92-1E.

Hoek, E. & Brown, E.T., 1980. *Underground Excavations in Rock*. revised ed. Abingdon: Institution of Mining and Metallurgy.

Hoek, E. & Brown, E.T., 1997. Practical estimates of rock mass strength. *International Journal of Rock Mechanics and Mining Science and Geomechanics Abstracts*, 57(8), pp.1165-86.

Hoek, E., Corkum, B. & Carranza Torres, C., 2002. Hoek-Brown failure criterion. In *Proceeding of the 5th North American Rock Mechanics Symposium*. Toronto, 2002.

Hoek, E., Kaiser, P.K. & Bawden, W.F., 1995. *Support of Underground Excavations in Hard Rock*. 3rd ed. Rotterdam, Balkema: Taylor & Francis.

Hoek, E., Marinos, P. & Benissi, M., 1998. Applicability of the geological strength index (GSI) classification for very weak and sheared rock masses. The case of the Athens Schist formation. *Bulletin of Engineering Geology and the Environment*, 57(2), pp.151-60.

Hsiao, F.Y., Wang, C.L. & Shao, H.J., 2011. Mechanical parameters estimation and tunnel deformation study for brittle rock under high overburden condition. *Rock and Soil Mechanics*, 32(S2), pp.109-14.

Hudson, J.A. & Harrison, J.P., 2007. *Engineering Rock Mechanics*. 1st ed. Amsterdam, Netherlands: Pergamon.

Itasca, 1993, and later. *3DEC User's Manuals*.

Itasca, 2002. *FLAC Manual*. Minneapolis, MN, USA.

Kaiser, P.K. et al., 2000. Underground works in hard rock tunneling and mining. *International Conference on Geotechnical and Geological Engineering*, pp.841-926.

Kaiser, P., Dwayne, D.T. & McCreath, D., 1996. Drift support in burst-prone ground. *CIM bulletin*, 89(998), pp.131-38.

Kaiser, P.K., McCreath, D.R. & Tannant, D.D., 1996. Canadian Rockburst Support Handbook. *Canadian Rockburst Research Program, Vol. II, Book I,* CAMIRO Mining Division.

Kazakidis, V.N., 1995. *A Numerical Modelling Analysis at the G-Zone of the Campbell Mine of Placer Dome Ltd*. MRD Report.

Kovari, K. & Tisa, A., 1975. Multiple failure state and strain controlled triaxial tests. *Rock Mechanics*, 7(1), pp.17-33.

Kristof, B., 1995. Sill pillar mining at the Brunswick mining No. 12 orebody. *Annual General Meeting of CIM*.

Kulhaway, F.H., 1975. Stress deformation properties of rock and rock discontinuities. *Engineering Geology*, 9, pp.327-50.

Lajtai, E.Z., 1971. A theoretical and experimental evaluation of the Griffith theory of brittle fracture. *Tectonophysics*, 11, pp.129–56.

Lanzano, G. et al., 2009. Experimental assessment of performance-based methods for the seismic design of circular tunnels. In *International Conference on Performance-Based Design in Earthquake Geotechnical Engineering*., 2009.

Lockner, D.A., 1995. *Rock Failure in Rock Physics and Phase Relations: A Handbook of Physical Constants*. Washington, DC: American Geophysical Union.

Martin, C.D., 1993. *The Strength of Massive Lac du Bonnet Granite Around Underground Openings*. Ph.D. thesis. University of Manitoba.

Martin, C.D., 1995. Brittle rock strength failure: Laboratory and in situ. *8th ISRM Congress*, 3, pp.1033-40.

Martin, C.D., 1997. Seventeenth canadian geotechnical Colloquium: The effect of cohesion loss and stress path on brittle rock strength. *Canadian Geotechnical Journal*, 34(5), pp.698-725.

Martin, C.D., 2005. *Preliminary assessment of potential underground stability (wedge and spalling) at forsmark, Simpevarp and Laxemar sites*. Quality report. Stockholm, Sweden: Svensk Kärnbränslehantering AB.

Martin, C.D. & Chandler, N.A., 1994. The progressive fracture of Lac du Bonnet granite. *International Journal of Rock Mechanics and Mining Sciences & Geomechanics Abstracts*, 31(6), pp.643–59.

Martin, C.D. & Christiansson, R., 2009. Estimating the potential for spalling around a deep waste repository in crystalline rock. *International Journal of Rock Mechanics and Mining Sciences*, 46(2), pp.219-28.

Martin, C.D., Kaiser, P.K. & McCreath, D.R., 1999. Hoek-Brown parameters for predicting the depth of brittle failure around tunnels. *Canadian Geotechnical Journal*, 36(1), pp.136-51.

Martino, J.B. & Chandler, N.A., 2004. Excavation-induced damage studies at the underground research laboratory. *International Journal of Rock Mechanics and Mining Sciences*, 41(8), pp.1413–26.

Martin, C.D., Read, R.S. & Martino, J.B., 1997. Observations of brittle failure around a circular test tunnel. *International Journal of Rock Mechanics and Mining Science*, 7(34), pp.1065–73.

Maxwell, S.C. & Young, R.P., 1998. Propagation effects of an underground excavation. *Tectonophysics*, 289(1-3), pp.17–30.

Oliveira, D.A.F., 2012. Application of a transversely isotropic brittle rock mass model in roof support design. *Coal Operators' Conference*, pp.15-22.

Olsson, W.A., 1991. The compressive strength of tuff as a function of strain rate from 10e-6 to 10e3 sec. *International journal of rock mechanics and mining sciences*, 28, pp.115-18.

Ortlepp, W.D., 1993. High ground displacement velocities associated with rockburst damage. In Young, P., ed. *3rd International Symposium on Rockbursts and Seismicity in Mines*. Kingston, Ontario, Canada, 1993.

Ortlepp, W.D., 1997. *Rock fracture and rockbursts – An illustrative study*. Johannesburg: The South African Institute of Mining.

Owen, G.N. & Scholl, R.E., 1981. *Earthquake engineering of large underground structures*. Final Report. San Francisco, CA: URS/Blume (John A.) Federal Highway Administration and National Science.

Paterson, S.M. & Wong, T., 2005. *Experimental Rock Deformation- The Brittle Field*. New York: Springer-Verlag.

Pelli, F., Kaiser, P.K. & Morgenstern, N.R., 1991. An interpretation of ground movements recorded during construction of Donkin-Morien tunnel. *Canadian Geotechnical Journal*, 2(28), pp.239-54.

Read, R.S., 1994. *Interpreting Excavated-Induced Displacements Around a Tunnel in Highly Stressed Granite*. Ph.D. thesis. Univeristy of Manitoba.

Read, R.S., 2004. 20 years of excavation response studies at AECL's underground research labratory. *International Journal of Rock Mechanics and Mining Sciences*, 3(41), pp.1251-75.

Read, R.S. & Martin, C.D., 1996. Technical Summary of AECL's Mine-by Experiment, Phase I : Excavation Response. AECL. pp.55-169.

Read, R.S., Martin, C.D. & Dzik, E.J., 1995. Asymmetric borehole breakouts at the URL. In JJK, D. & RA, S., eds. *The 35th U.S. Symposium on Rock Mechanics (USRMS)*. Rotterdam, Balkema, 1995. American Rock Mechanics Association (ARMA).

Rockscience, 2008. *User's manual*. Toronto, Ontario: Rockscience.

Rocscience, I., 2007. *RocLab Version 1.031—Rock mass strength analysis using the Hoek–Brown failure criterion*. [Online].

Sheorey, P.R., Biswas, A.K. & Choubey, V.D., 1989. An empirical failure criterion for rocks and jointed rock masses. *Engineering Geology*, 26(2), pp.141-59.

Stacey, T.R. & Ortlepp, W.D., 1993. Rockburst mechanisms and tunnel support in rockburst conditions. In *Proceedings of International Conference in Geomechanics*. Ostrava, Czech Republic, 1993.

Stavrogin, A.N., Tarasov, B.G., Shirkes, O.A. & Pevzner, E.D., 1982. Strength and deformation of rocks before and after the breakdown point. *Journal of Mining Science*, 17(6), pp.487-93.

Stavropoulou, V., 1982. *Constitutive Laws for Brittle Rocks*. Ph.D. thesis. 334.p: University of Witwatersrand.

Stevenson, T., 1986. *Improving Ground Stability and Mine Rescue*. Provincial Inquiry into Ground Control and Emergency Preparedness in Ontario Mines.

Urbancic, T.I., 1993. *Lockerby Mine - Seismic activity associated with the 34-36 Sill Pillar Internal Reports*. Lockerby Sill Pillar Project.

Valley, B. et al., 2011. Influence of confinement dependent failure processes on rock mass strength at depth. Beijing, China, 2011. Proc. 12th ISRM International Congress on Rock Mechanics.

Vasak, P. & Kaiser, P.K., 1995. *Tunnel stability assessment during rockbursts*. Montreal, Quebec: CAMI 95, 3rd Canadian Conference on Computer Applications in the Mineral Industry.

Vermeer, P. & De Borst, R., 1984. Non-associated plasticity for soils, concrete and rock. *Delft University of Technology*, 3(29), pp.1–64.

Wagner, H., 1987. Design and support of underground excavations in highly stressed rock. *Proceeding of the 6th ISRM Congress on Rock Mechanics*, pp.1443-57.

Wang, J.-N.J., 1993. *Seismic Design of Tunnels- a simple state of-the-art design approach*. 1st ed. New York, New York: Parsons Brinckerhoff Inc.

Wawersik, W.R. & Fairhurst, C., 1970. A study of brittle rock fracture in laboratory compression experiments. *International Journal of Rock Mechanics and Mining Sciences and Geomechanics Abstracts*, pp.561-64.

Wiles, T. & MacDonald, P., 1988. *Correlation of Stress Analysis Results with Visual and Microseismic Monitoring at Creighton Mine*. Computers and Geotechnics.

Young, R.P. & Collins, D.S., 1999. Monitoring an experimental tunnel seal in granite using acoustic emission and ultrasonic velocity. *Rock Mechanics for Industry, Proceedings of the 37th US Symposium on Rock Mechanics*, pp.869-76.

Young, R.P. & Martin, C.D., 1993. Induced seismicity investigations in the site characterization and performance monitoring of nuclear waste repositories. *International Journal of Rock Mechanics and Mining Science*, 30(7), pp.797–803.

Zhao, X.G. & Cai, M., 2010. A mobilized dilation dngle model for rocks. *International Journal of Rock Mechanics and Mining sciences*, 47(3), pp.368-84.

Zhao, X., Cai, M. F. & Cai, M., 2010. Consideration of rock dilation on modeling failure and deformation of hard rocks _ A case study of the mine-by-test tunnel in Canada. *Journal of Rock Mechanics and Geotechnical Engineering*, 2(4), pp.338-49.